CZECH TECHNICAL
UNIVERSITY
IN PRAGUE

FACULTY OF MECHANICAL ENGINEERING
DEPARTMENT OF ENERGY ENGINEERING

2020

MASTER'S THESIS

CFD ANALYSIS OF THE COOLANT FLOW THROUGH THE FUEL ASSEMBLY OF THE REACTOR LVR-15

Bc. MICHAELA ŽABČÍKOVÁ

ZADÁNÍ DIPLOMOVÉ PRÁCE

I. OSOBNÍ A STUDIJNÍ ÚDAJE

Příjmení:	**Žabčíková**	Jméno: **Michaela**	Osobní číslo: **457558**

Fakulta/ústav: **Fakulta strojní**
Zadávající katedra/ústav: **Ústav energetiky**
Studijní program: **Jaderná energetická zařízení**
Studijní obor: **Jaderná energetická zařízení**

II. ÚDAJE K DIPLOMOVÉ PRÁCI

Název diplomové práce:

CFD analýza proudění chladiva palivovým souborem reaktoru LVR-15

Název diplomové práce anglicky:

CFD analysis of the coolant flow through the fuel assembly of the reactor LVR-15

Pokyny pro vypracování:

Osnova:
1. Popis reaktoru LVR-15 se zaměřením na palivový soubor a způsob jeho chlazení.
2. Zapojení reaktoru LVR-15 do projektu FOREvER.
3. CFD model proudění chladiva palivovým souborem reaktoru LVR-15.
4. Analýza proudění chladiva palivovým souborem reaktoru LVR-15.

Seznam doporučené literatury:

Jméno a pracoviště vedoucí(ho) diplomové práce:

Ing. Pavel Zácha, Ph.D., ústav energetiky FS

Jméno a pracoviště druhé(ho) vedoucí(ho) nebo konzultanta(ky) diplomové práce:

Ing. Marek Ruščák, Centrum výzkumu Řež s.r.o.

Datum zadání diplomové práce: **24.04.2020** Termín odevzdání diplomové práce: **26.06.2020**

Platnost zadání diplomové práce: **31.12.2021**

Ing. Pavel Zácha, Ph.D.
podpis vedoucí(ho) práce

podpis vedoucí(ho) ústavu/katedry

prof. Ing. Michael Valášek, DrSc.
podpis děkana(ky)

III. PŘEVZETÍ ZADÁNÍ

Diplomantka bere na vědomí, že je povinna vypracovat diplomovou práci samostatně, bez cizí pomoci, s výjimkou poskytnutých konzultací. Seznam použité literatury, jiných pramenů a jmen konzultantů je třeba uvést v diplomové práci.

.
Datum převzetí zadání

Podpis studentky

© ČVUT v Praze, Design: ČVUT v Praze, VIC

The statement of authorship

I hereby certify that the thesis I am submitting is entirely my own original work except where otherwise indicated. I am aware of the University's regulations concerning plagiarism, including those regulations concerning disciplinary actions that may result from plagiarism. Any use of the works of any other author, in any form, is properly acknowledged at their point of use.

In Prague on ………………………

………………………
Bc. Michaela Žabčíková

Annotation sheet

Author's name: Bc. Michaela Žabčíková

Title of thesis: CFD analysis of the coolant flow through the fuel assembly of the reactor

Czech title: CFD analýza proudění chladiva palivovým souborem reaktoru LVR-15

Academic year: 2019/2020

Specialization: Nuclear Power Engineering Equipment

Department: Department of Energy Engineering

Supervisor: Ing. Pavel Zácha, Ph.D.

Consultant: Ing. Marek Ruščák
Ing. Vincenzo Romanello, Ph.D.
Ing. Antonio Dambrosio

Bibliographic data: Number of pages: 104
Number of figures: 78
Number of tabels: 12
Number of attachements: 1

Abstract: The diploma thesis is focused on the CFD analysis of two fuel assemblies for the research reactor LVR-15. It is performed in the frame of the European project FOReVER. The thesis consists mainly of two parts: the evaluation of the hydraulic characteristics of both fuel assemblies (French and Russian design) and the analysis of the flow through them. For the CFD modelling, the ANSYS software pack was used.

Anotace: Diplomová práce se zabývá CFD analýzou dvou druhů palivových souborů pro výzkumný reaktor LVR-15. Práce je součástí evropského projektu FOReVER. Součástí práce jsou hydraulické charakteristiky obou souborů (francouzského a ruského designu) a rozbor proudění skrz ně. Pro CFD model byl použit softwarový balíček ANSYS.

Keywords: CFD, nuclear fuel assembly, research reactor, safety, pressure drop

Klíčová slova: CFD, jaderný palivový soubor, výzkumný reaktor, bezpečnost, tlaková ztráta

Acknowledgements

I would like to express the deepest appreciation to my supervisor, Ing. Pavel Zácha, Ph.D for the time and the precious advice. I would like to thank my co-workers, Ing. Marek Ruščák, Ing. Vincenzo Romanello, Ph.D. and Ing. Antonio Dambrosio for providing the working background.

I must express my gratitude to my family and friends for supporting me throughout my years of study and the process of writing this thesis.

List of figures

List of tables

List of equations

Contents

List of abbreviations and symbols

ANP	Areva NP (Framatome)
BC	Boundary Conditions
BNCT	Boron Neutron Capture Therapy
BSL	the Mentel Baseline
BWR	Boiling Water Reactor
CANDU	Canada Deuterium Uranium
CEA	French Alternative Energies and Atomic Energy Commission
CFD	Computational fluid dynamics
CVR	Centrum Výzkumu Řez
DES	Detached Eddy Simulation
DNS	Direct Numerical Simulation
EDF	Électricité de France S.A.
EWT	Enhanced Wall Treatment
FA	Fuel Assembly
HTHL2	High-Temperature Helium Loop
IRE	Institut National des Radioéléments
IRSN	Radioprotection and Nuclear Safety Institute
LES	Large Eddy Simulation
LMFR	Liquid Metal-cooled Fast Reactor
LOCA	Loss of Coolant Accident
LTA	Lead Test Assembly
MSR	Molten Salt Reactor
NCBJ	National Centre for Nuclear Research Poland
PWR	Pressurized Water Reactor
RANS	Reynolds-averaged Navier-Stokes
RSM	Reynolds stress model
SCWL2	Supercritical Water Loop
SST	the Shear Stress Transport
SUJB	Státní úřad pro jadernou bezpečnost
TA	TeachnicAtome
VVER	Water-Water Power Reactor
VHTGR	Very High-temperature Gas-cooled Reactor

A	area [m^2]
E	Young's modulus [MPa]
$\vec{f}$	vector field of volume forces [N·kg^{-1}]
h	thermal conductivity [W·m^{-1}·K^{-1}]
k	turbulent kinetic energy [J·kg^{-1}]
$\vec{n}$	unit normal vector of surface [1]
P	general physical property
$\dot{P}^{(g)}$	the amount of quantity generated in a unit of volume per unit of time
p	pressure [Pa; bar]
$\bar{p}$	time-averaged pressure [Pa; bar]
$\dot{Q}^{(g)}$	rate of heat generation per unit volume [W·m^{-3}]
$\vec{q}$	heat flux [W·m^{-2}]

T	thermodynamic temperature [K]
$\vec{u}$	velocity [m·s^{-1}]
$\overline{\vec{u}}$	mean velocity [m·s^{-1}]
$\overrightarrow{u}'$	fluctuation velocity component [m·s^{-1}]
u^+	dimensionless velocity [1]
u_τ	friction velocity [m·s^{-1}]
u_E	specific internal energy [J·kg^{-1}]
$\overline{v^2}$	wall-normal velocity fluctuation [m^2·s^{-2}]
y	absolute distance [m]
y^+	dimensionless wall distance [1]
$\frac{d}{dt}$	time derivative
α	heat transfer coefficient [W·m^{-1}·K^{-2}]
α_V	coefficient of thermal expansion [K^{-1}]
Γ	weighting factor [1]
$\overrightarrow{\overrightarrow{\Delta}}$	strain rate tensor [s^{-1}]
$tr\overrightarrow{\overrightarrow{\Delta}}$	trace strain rate tensor [s^{-1}]
$\overline{\overrightarrow{\overrightarrow{\Delta}}}$	mean strain rate tensor [s^{-1}]
δ	rupture ductility [%]
$\overrightarrow{\overrightarrow{\delta}}$	unit symmetric tensor [1]
ϵ	turbulent dissipation rate [m^2·s^{-3}]
λ	coefficient of frictional resistance [1]
μ	dynamic viscosity [Pa·s]
$\mu^{(t)}$	turbulent dynamic viscosity [Pa·s]

ν	kinematic viscosity [m^2·s^{-1}]
ν_t	kinematic turbulent viscosity [m^2·s^{-1}]
$\tilde{\nu}$	modified turbulent viscosity [m^2·s^{-1}]
Π	flux of a physical quantity
ρ	density [g·cm^{-3}]
ρ_e	specific electrical resistance [Ω·cm^{-1}]
σ	ultimate strength [MPa]
σ_c	ultimate creep strength [MPa]
$\overrightarrow{\overrightarrow{\sigma}}^*$	total pressure [Pa]
$\sigma^{(s)}$	Stefan – Boltzmann constant
$\overrightarrow{\overrightarrow{\tau}}$	shear stress tensor [Pa]
$tr\,\overrightarrow{\overrightarrow{\tau}}$	shear stress tensor trace [Pa]
$\overline{\overrightarrow{\overrightarrow{\tau}}}^{(t)}$	Reynolds stresses tensor [Pa]
τ_w	wall shear stress [Pa]
$\overline{\overrightarrow{\overrightarrow{\Omega}}}$	mean vorticity tensor [s^{-1}]
ω	specific rate of dissipation [s^{-1}]
∇	Nabla operator

Introduction

This diploma thesis is performed in the frame of the European research and innovation project FOREvER. One of the biggest challenges for European research nuclear reactors in these days is their continuity of operation; for this reason, the guaranty of the nuclear fuel supply represents a crucial aspect. In Europe, several high-performance research reactors and medium-power research reactors may have problems with nuclear fuel supply in the future. The European Commission, knowing this problem, included the topic *NFRP 11: Support for the EU security of supply of nuclear fuel for research reactors* into research program H2020 EUROATOM for years 2016-2017. The main reason for this reaction is to ensure the production the medical isotope of Molybdenum-99, and the irradiation capacities for material research and other research applications.

The primary purpose of this diploma thesis is to perform the hydraulic analysis using the CFD approach. In particular, it is the analysis of the pressure drop of the IRT-4M fuel assembly and the new CERCA fuel assembly. Among the outputs, there are the axial profiles of the pressure drop and the average velocities in the CERCA FA. These axial profiles are further used in the project as the input data for the thermohydraulic calculations. In our case, it is the RELAP5 code, which is able to simulate the entire reactor cooling system. Part of the work is also focused on the specification of flow in both fuel assemblies, in other words, the character of the flow in the areas of the fuel elements, which from the safety point of view must be actively cooled. The results from the CFD analysis are validated with the data received from the designer of the new LVR-15 fuel, i.e. TechnicAtome (TA). They will also be compared to the planned experiment to estimate the pressure drop of the CERCA fuel assembly.

In the first chapter of this thesis, there is a description of the reactor LVR-15. The description is focused on a fundamental technical information about the reactor itself and its purpose. The currently used fuel assembly and the whole cooling systems are described in more detail. The second chapter is focused on the detailed description of the FOREvER project, the preliminary design of the CERCA fuel assembly and the goals of the CVR within the project. The other codes used in this project are also described in this chapter. A detailed description of the CFD code is given in the third chapter. It includes a description and the derivation of the Continuity, the Navier-Stokes and the Energy equations. Moreover, there is also a description of the most used turbulent models in CFD and information about the mesh types and its quality assessment. The following chapters are focused on the practical part of the analysis like the creation of the geometry for mesh generation, the results of the mesh sensitivity analysis and the visual form of the final meshes. The solver settings used are shown in the text in tabular form for clarity. Specifically, the chapter 4 includes the CERCA FA analysis with the comparison of the results to the data from the TechnicAtome, the hydraulic characteristic, the axial profiles of hydraulic parameters and the flow analysis itself. Similar information are documented for the IRT-4M in the chapter 5. The chapter also contains a comparison between the hydraulic characteristic of the IRT-4M and the CERCA FA.

Chapter 1: Description of the LVR-15 Nuclear Reactor

Reactor LVR-15 is a research reactor cooled by light water. It is a tank-type thermal reactor (i.e. fission mainly due to thermal neutrons) placed in a non-pressure vessel. Light water works at the same time as a cooling medium and as the moderator of neutrons. Depending on the operating configuration, light water can also be used as a reflector of the neutron flux. The maximum thermal operating power of this reactor is 10 MW and its operational time is subdivided in campaigns. The reactor is the property of company Centrum výzkumu Řež, and its located near to Prague in Czech Republic [1].

The vessel of the reactor is made of 08CH18N10T stainless steel. Most of the internal components, the horizontal channels, the core shell and the grid plate of the active zone are made by aluminum with a purity of 99 %. The vessel is covered by a shielding lid. The outer diameter of the vessel is 2300 mm and the height is 5760 mm. The wall thickness of the vessel is 15 mm and the floor thickness of the vessel is 20 mm. The whole volume of water inside the vessel is 22 m^3 and the weight of the vessel without water is 7900 kg. The other components within the reactor are:

- A facility for used nuclear fuel
- Grips for unused horizontal channels
- Grip plate for unused nuclear fuel
- Emergency shower which is placed over the active zone
- Grip plate for control rods which is also placed over the active zone
- Vertical channels for ionization chamber

Visual description of the reactor LVR-15 is showed in Figure 1.

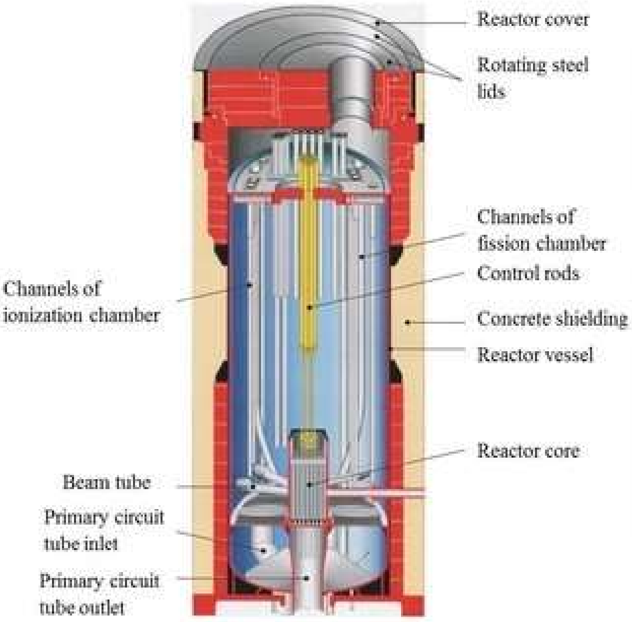

Figure 1 – *The cross section of the LVR-15 reactor [2]*

The active zone of the reactor is composed of fuel assemblies, beryllium blocks, irradiation channels and water displacers. The beryllium blocks are used as radial reflectors and the irradiation channels are used for samples irradiation. The nuclear fuel assemblies, which are used in this reactor are a Russian-type IRT-4M with enrichment of 19.7 % ^{235}U. The number of fuel assemblies can vary between 28 and 32, according to the operating configuration. Few of these fuel assemblies, usually between 12 and 15 are used for the placement of control rods. Control rods are made by boron carbide and 8 of them are used for compensation of reactivity, 3 as emergency ones and 1 of them belongs to the automatic control system. An example of a typical operating configuration of an active zone is documented in Figure 2. Summary of basic information about active zone of the reactor LVR-15 is in table 1 [1].

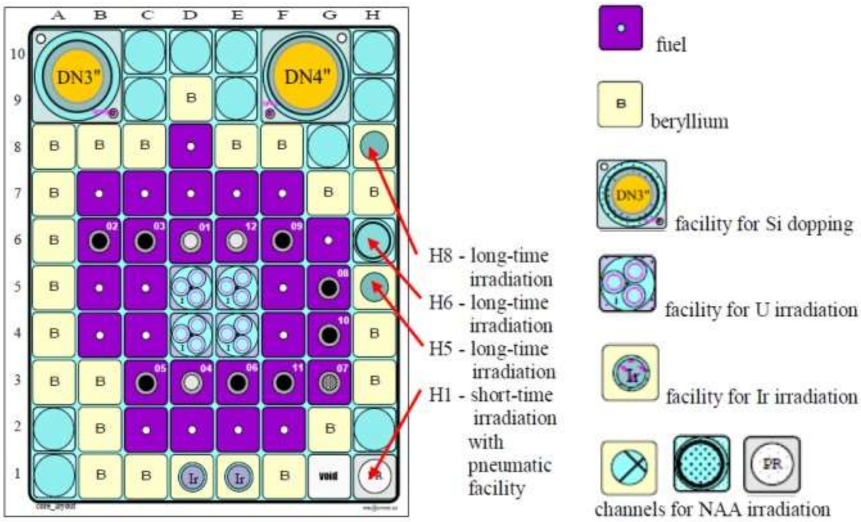

Figure 2 – *Example of an operating configuration of the active zone [3]*

Table 1 – *Summary of basic information about the active zone of the reactor LVR-15*

Type of reactor	Pool-type with forced cooling
Thermal power [MW]	10
Volume flow of cooling medium [$m^3 \cdot h^{-1}$]	2100
Type of fuel	IRT-4M
Type of cooling medium	Water
Type of moderator	Water
Type of reflector	Water or Beryllium
Type of active zone	Square
Grid spacing [mm]	71.5 x 71.5
Number of positions in active zone	8 x 10

1.1 The LVR-15 Reactor Applications

The LVR-15 reactor has many experimental facilities and it is being used for many different types of experiments. Water loops can be found between the most important experimental facilities. They are used for the simulation of the operating condition in primary circuits of PWR (VVER) and BWR reactors. Their construction consists of a piping system with an active channel placed in the active zone of the reactor. Most of the experiments in these water loops are focused on the behavior of the construction materials in the irradiation environment. Other important experimental devices are the irradiation probes. Thanks to them, it is possible to irradiate samples of construction materials that are used for reactors pressure vessels in the Czech Republic and in the whole world as well. For the irradiation of the monocrystals of Si or for a different kind of neutron transmutation doping there is a special type of experimental device called DONA. It is basically a vertical channel made by aluminum and placed in the active zone of the reactor. This equipment has its measuring and controlling apparatus; the entire control of the irradiation process is automatic. The reactor is also used for the production of ^{99}Mo, which decays to ^{99}Tc used in medical treatment. For this process, the irradiation targets IRE are used. Targets are made of high enriched uranium and ^{99}Mo is one of the fission products. They are placed in the center of the active zone in a "neutron trap" surrounded by fuel assemblies. For the medical applications, the reactor was also used for Boron Neutron Capture Therapy (BNCT). In the reactor building there is a "heat chamber" that produces a pack of epithermal neutrons. From

2002 – 2006 this facility was used for the irradiation of 5 patients, but since 2007 it has only been used for research purposes. Experimental facilities contain vertical and horizontal channels. Vertical channels are used for the standard irradiation of samples. They can be surrounded by a beryllium reflector, water reflector, or by fuel assemblies, according to a desired neutron flux. Horizontal channels are used for the outlet of the neutron beam exiting the active zone of the reactor, and its used for different kind of experiments, for example the study of gamma radiation from radiation capture. The device used for short time irradiations is called “pneumatic mail”. In this case the typical irradiation samples are fragments of soil, rock, fly ash, and aerosols. To work with radioactive material, five hot chambers are installed in the reactor hall. The location of some experiment facilities is documented in Figure 3 [1].

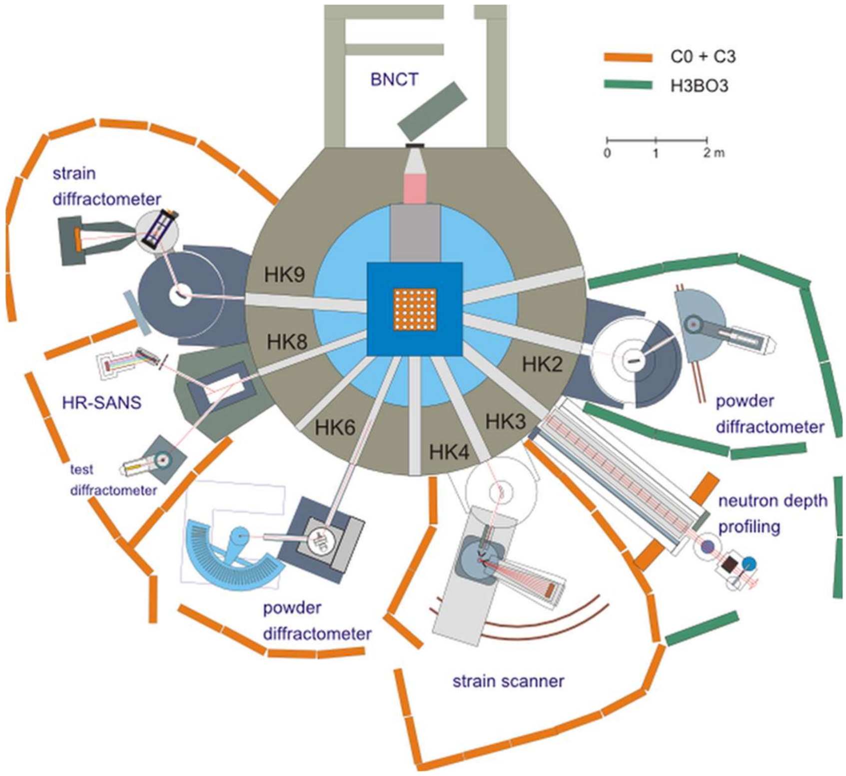

Figure 3 – *Location of horizontal channels and experimental facilities connected to them [4]*

Two new experimental facilities are being built for experiments connected with research in the European fusion program and the Gen IV reactors. The first one is the SCWL2 loop; it should be used for the research in the field of supercritical water, specifically for studies about construction materials and water radiolysis in supercritical conditions. Operating conditions are designated for temperature up to 600 °C and for pressure up to 25 MPa. The second experimental facility under construction is the HTHL2 loop. This loop is called High Temperature Helium Loop and it is built to simulate the Gen IV Very High Temperature Reactors. The loop will use high purity helium, which operating conditions are around 900 °C and 7 MPa. The main purpose of this loop is to test and optimize the helium cleaning system and to test the materials in the operating conditions of the Very High Temperature Reactors. Both SCWL2 loop and HTHL2 loop should be able to operate in active and non-active conditions, i.e. both inside and outside of the active zone [1].

1.2 Description of the IRT-4M Fuel Assembly

The IRT-4M fuel assembly is a plate-type fuel, which is very common for research and testing reactors. In this case, the fuel core is formed by dispersion of UO_2 and aluminum powder. These two components are coupled by a sintering process and the whole fuel meat is enclosed in an aluminum alloy cladding and assembled into fuel elements. Aluminum is used because of its low absorption cross section and for its good thermodynamic properties such as thermal conductivity. Fuel elements have the shape of concentric tubes with square cross section and the fuel assemblies can be made of eight, six or four tubes. The fuel elements are equipped with endings made by the same aluminum alloy as cladding of fuel tubes. Figure 4 shows the six-tube version of the IRT-4M fuel assembly and has captured parts of one fuel element and both assembly endings.

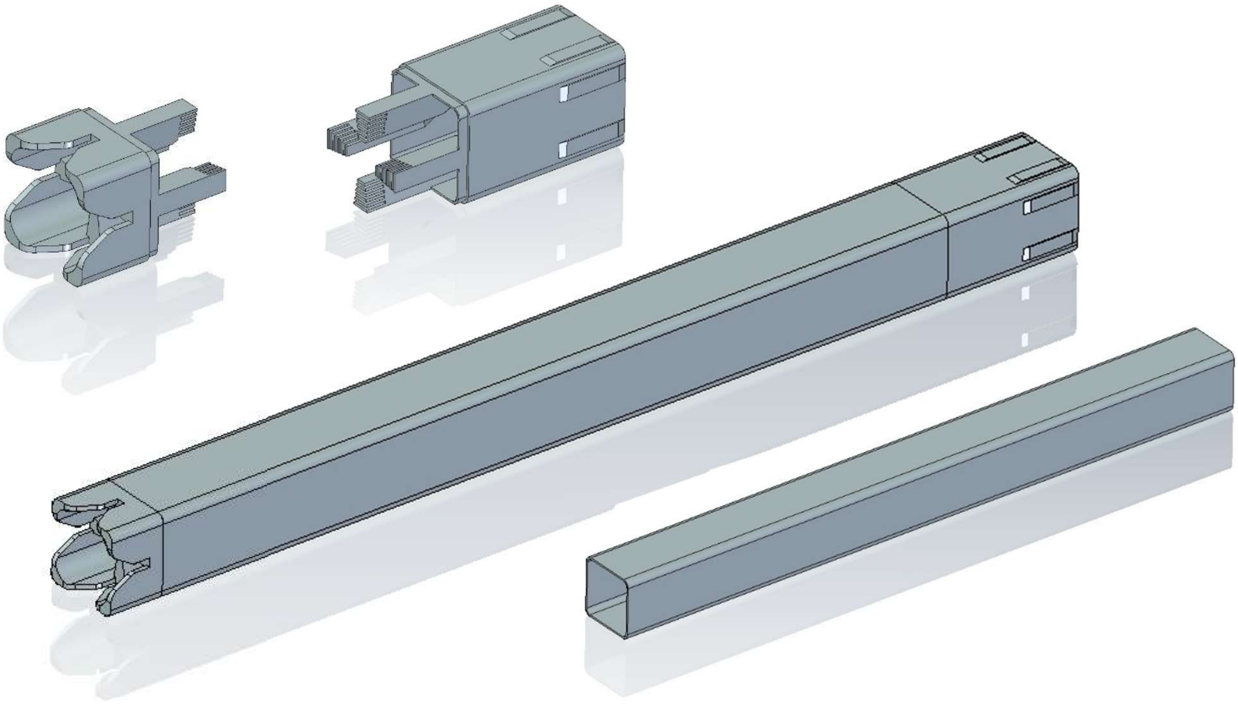

Figure 4 – *Six-tube IRT-4M FA version*

The top part has hole with a diameter of 64 mm, which serves to manipulate the fuel assembly with use of a handling tool. The bottom part has four cutouts with dimensions 8 x 35 mm, which provide accurate settling of fuel assembly in the carrier plate of the active zone. In the case of the eight-tube version, the tube with diameter of 14 mm is inserted in the middle of the fuel assembly. This tube works as a throttle valve and provides greater cooling flow around fuel elements. Specific description of material properties of used aluminum alloy is documented in following table 2 [1].

Table 2 – *Summary of basic information about aluminum alloy used for FA IRT-4M (valid for temperature between 20 – 100°C)*

Density ρ [g·cm^{-3}]	2.68
Thermal conductivity *h* [W·m^{-1}·K^{-1}]	201
Coefficient of thermal expansion α [K^{-1}]	$22.3 \cdot 10^{-6}$
Specific electrical resistance ρ_e [Ω·cm^{-1}]	$2.86 \cdot 10^{-6}$
Ultimate strength σ [MPa]	$(2.06 – 2.26) \cdot 10^{2}$
Ultimate creep strength σ_c [MPa]	$1.08 \cdot 10^{2}$
Young’s modulus *E* [MPa]	$(6.3 – 6.7) \cdot 10^{4}$
Rupture ductility δ [%]	29

In the LVR-15 reactor there are only eight and six tubes version. The six-tube version is used with control rod or as an irradiation channel [1].

1.3 The Cooling System of the Reactor LVR-15

The Cooling system is composed of three operating circuits, together with an emergency system for residual heat removal and the emergency shower system [1].

The primary circuit provides water flow between the reactor vessel and the two heat exchangers branches. The volume flow through the primary circuit can be set up in intervals between 0 – 2100 $m^3 \cdot h^{-1}$. For an operating power below 50 kW, the minimum required volume flow through the reactor is 790 $m^3 \cdot h^{-1}$. During full power operations, the needed volume flow through the reactor is between 1350 and 1500 $m^3 \cdot h^{-1}$ with a maximum inlet temperature of 45°C and an outlet temperature around 55 – 60 °C. From a safety point of view, at least one main circulation pump and one emergency pump are needed during operations with power higher than 50 kW. The total amount of working pumps depends on the operating power and the required volume flow through reactor. In the cases of loss of electric power supply, the main circulation pump is connected to the diesel aggregate and the emergency pump is powered from battery for a sufficient time to start the diesel aggregate. In the primary circuit five main circulation pumps and two emergency pumps are installed. The pipeline system of the primary circuit is made as all-welded. Flange joints are located only at inlets and outlets of pumps, heat exchangers, and pressure vessel of the reactor. The whole pipeline system of the primary circuit is equipped with regulating gate valves, which allow the regulation of volume flow through that circuit. The regulation of the primary circuit is done from control room during normal operations and in cases of shutdown it is possible to regulate it directly from the pumping room [1].

The secondary circuit provides heat transfer from the primary circuit to the tertiary circuit and, at the same time, it forms a barrier against penetration of radioactive water into Vltava river, which is used for cooling the whole system. The secondary circuit is composed of a primary and a secondary heat exchangers, the secondary circuit pumps, and other auxiliary equipment. Overall, there are three pumps in the secondary circulation system which are connected to the electrical supply through frequency converters. Thanks to these frequency converters it is possible to change the water volume flow in wide intervals. When acting as a barrier the secondary circuit pressure is set 0.45 – 1 MPa higher than the pressure in the primary circuit. The volume flow depends on the operating power and on the season; usually it is around 800 $m^3 \cdot h^{-1}$. The inlet temperature of the primary heat exchanger is around 30 °C and the outlet is normally around 38 °C. Filtered water is used as cooling medium [1].

The tertiary circuit transfers heat from the secondary circuit into Vltava river. This circuit contains three horizontal pumps, which provide water flow from Vltava river into the secondary heat exchanger: water is mechanically cleaned before use. From the secondary heat exchanger water is transported back to the Vltava river with maximum allowed temperature of 26 °C: this water cannot be mixed with any chemicals against corrosion or for pH adjustment. The volume flow through the circuit is highly dependent on the seasonal state: during winter it is around 250 $m^3 \cdot h^{-1}$ and in summer it can be around 850 $m^3 \cdot h^{-1}$. The flow is regulated with frequency converters [1].

Among the supporter circuits, there is a primary water cleaning circuit. The suction point of the cleaning circuit is located on the reactor vessel outlet pipeline, before the position of main pumps. The displacer is located on the vessel inlet pipeline, between the volume flow measuring facilities and the regulating gate valve. This cleaning circuit is used only when the water prescribed parameters are exceeded. During reactor operation, it is possible to separate this circuit from the primary one with manual and electric valves. The emergency system for residual heat removal consists of the selected pumps of the primary circuit, which have back up power supply: specifically, it is main pump number 1 together with one of the emergency pumps number 6 and 7. The emergency shower system is made up of four interconnected tanks with demineralized water. In cases of water leak from the primary circuit, these tanks can provide water supply into reactor vessel with volume flow between $2 - 4\ dm^3 \cdot s^{-1}$. The volume of each tank is $10.6\ m^3$ and the system is able to handle water leak with a maximum water flow of $4.4\ dm^3 \cdot s^{-1}$, lasting 1.25 hour, when operated alone, and a maximum water flow of $8\ dm^3 \cdot s^{-1}$, if operated together with hydrants. The system is controlled automatically according to the operating water level in the reactor vessel [1].

Chapter 2: The European Project FOREvER

The full name of this project is Fuel fOr REsearch Reactors. The overall objective of this project is to secure the nuclear fuel for European nuclear research reactors. The project has two main goals; the first is the conversion from high to low enriched uranium fuel through the use of Mo fuels technology (the test name will be HiPROSIT). The second goal is to provide an action against the ROSATOM monopoly for European medium-power research reactors, with a test named 4EVERTEST. The reactor LVR-15 was selected as a case study for designing a new core that could work with the original IRT-4M fuel assemblies and the European fuel assemblies based on U_3Si_2 flat fuel plates. The participants on this project are [5]:

- COMMISSARIAT A L ENERGIE ATOMIQUE ET AUX ENERGIES ALTERNATIVES (France)
- TechnicAtome (France)
- Société Technique pour l'Energie Atomique (France)
- INSTITUT MAX VON LAUE – PAUL LANGEVIN (France)
- LGI CONSULTING SARL (France)
- TECHNISCHE UNIVERSITAET MUENCHEN (Germany)
- NARODOWE CENTRUM BADAN JADROWYCH (Poland)
- Studiecentrum voor Kernenenergie/Centre d'Etude de l'Energie Nucléaire (Belgium)
- CENTRUM VÝZKUMU REZ S.R.O. (Czech Republic)

2.1 More about 4EVERTEST

Medium-power research reactors are considered nuclear research reactors with operating thermal power under 20 MW. These types of research reactors with original Soviet design have only one fuel provider in Europe, the ROSATOM-owned company TVEL. Two examples of these reactors are the LVR-15 in the Czech Republic and the BRR in Hungary [5].

Modifying the geometry of the fuel assembly is required to use European-manufactured nuclear fuel based on dispersion of U_3Si_2 in Russian designed research reactors. It is important because Europe uses different manufacturing technologies for nuclear fuel. A plate type fuel with a similar geometry is already used in different nuclear research reactors and is needed to perform Lead Test Assembly (LTA) irradiations in a prototype reactor. For this project it will be inserted in the reactor LVR-15. Specific goals in this part of project are to design a prototypic fuel assembly and perform the neutronic and thermohydraulic safety calculations, then to produce the physical prototype of the fuel and perform the irradiation test. The preliminary design of the CERCA fuel assembly with captured parts as one fuel element and both assembly endings is documented in Figure 5 [5].

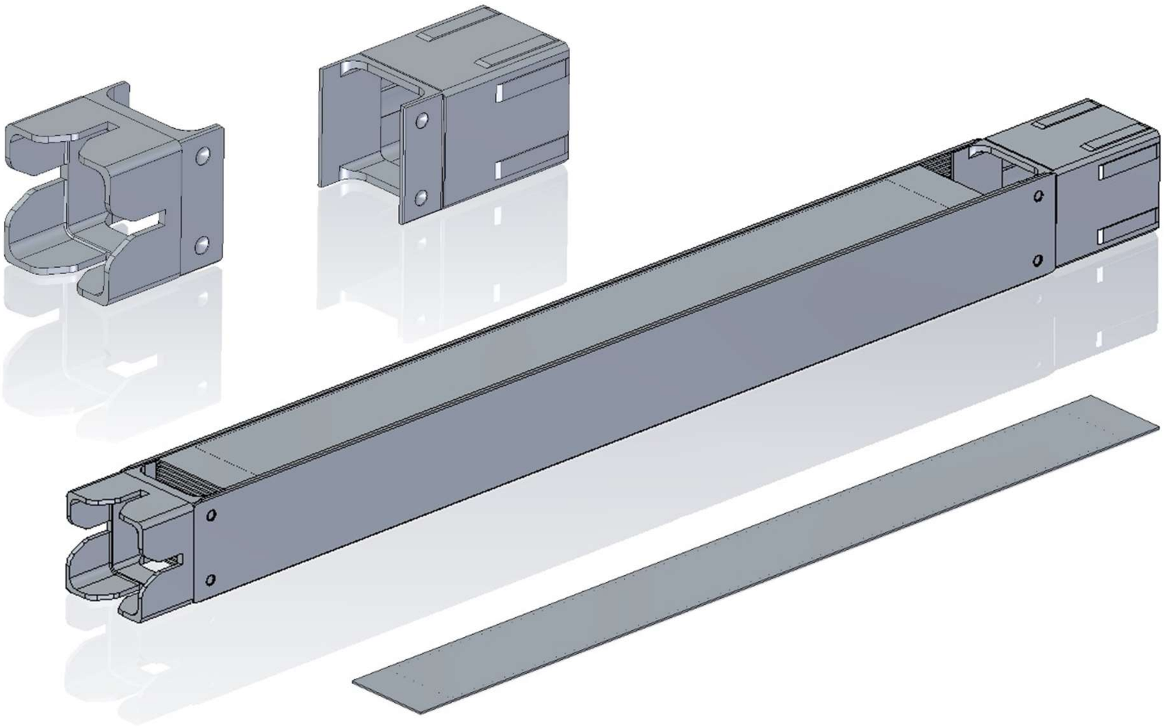

Figure 5 – *Preliminary design of the CERCA FA*

2.2 The Part of the CVR in 4EVERTEST

The CVR has several tasks in the project. The first task is reactor data gathering and the transfer of relevant information to the designer (TA) and preliminary analysis associated with the fuel used so far. Specifically, it is data about fuel element characteristic, fuel assembly characteristic, core requirements and reactivity control, instrumentation and control data, operational limits and conditions, and fuel core interfaces. On this section the CVR is cooperating with the NCBJ with their research reactor MARIA. The second task is to produce reliable and robust European fuel assembly for medium-power research reactors. In this part the CVR cooperates with the ANP under the direction of the TA. The third task is preliminary design of Controlled and Standard Fuel assemblies supported by neutronic and thermohydraulic calculations on the whole core of the LVR-15 made by the new fuel assemblies. The next step is the data collecting regarding general safety and licensing requirements: a significant task for the CVR is performing of neutronic and thermal-hydraulic calculations with the LVR-15 mixed core. The CVR must also perform an hydraulic test to estimate the pressure drop of the standard prototype fuel assembly. Outputs will be submitted to the Czech regulatory authority (SÚJB) in order to get the new operational licensing with the prototype fuel. After the licensing, the fuel assembly will be irradiated in the reactor LVR-15. This test will be crucial for the demonstration of the feasibility of replacing the original IRT-M4 fuel with the new fuel [5].

2.3 Other Codes Used in the Project FOREvER

Several computational codes are used in this project. Some of them are focused on neutron physics, others on thermohydraulics, and others on nuclear safety and emergency conditions. A few of them are listed in the following section with a short description.

2.3.1 APOLLO2

APOLLO2 is a deterministic neutron code developed by the French CEA with support from former AREVA and Electricité de France. This code is based on the Boltzmann equation, the gamma transport equation and the multi-group method. In comparison to the codes which use the Monte Carlo method, APOLLO2 uses specific mathematical methods to solve the Boltzmann equation and with sufficient computing power [6]. Among the most frequently used numerical methods there are the Method of Characteristic, which is a technique for solving partial differential equation, the SN discrete ordinates method, and the Method of collision-probability. The software is designed primarily for PWR and BWR industry. However, several studies have been done to demonstrate the possibility of using this code also for VVER technology [7].

2.3.2 TRIPOLI-4

TRIdimensionnel POLYcinétique (TRIPOLI-4) is another code developed by the French CEA, which is able to solve a linear Boltzmann equation for neutrons and photons using the Monte Carlo method [8]. It is used as a reference code in nuclear fission and fusion industry. Development of this code began in the 1990s using programming language C++. The code is currently capable of calculating in three-dimensional space with continuous-energy of particles. Key features include the possibility of simulating four kinds of particles using coupling. Between these particles there are neutrons with energy from 20 MeV down to 10^{-5} eV, photons with energy from 50 MeV down to 1 keV, electrons and positrons, both with energy from 100 MeV down to 1 keV [9].

2.3.3 RELAP5

RELAP5 is the advanced version of the RELAP, which is the thermohydraulic code developed at the Idaho national laboratory. The full name of this program is Reactor Excursion and Leak Analysis Program. It is useful not only for reactor safety analyses, but also for the reactor design or as a simulator for the operator training. The code is capable of simulating a wide range of different accidents. Thanks to the extensive fluid library, it is also possible to simulate reactor systems such as CANDU, VHTGR, MSR or LMFR. As in the case of other thermohydraulic codes, the calculations are based on two-phase model with balancing equations for the mass, the momentum, and the energy [10].

2.3.4 TRACE

The original code is named TRAC, fully The Transient Reactor Analysis Code, which was developed by Los Alamos National Laboratory. In the past, there were four codes with very similar computational capabilities. These codes were TRAC-P, TRAC-B, RELAP5, and RAMORA. All were neutronic-thermohydraulic codes, some of them focused on small break LOCA and some of them on large break LOCA. Over the years these codes have been merged into one single modernized code: the TRAC/RELAP Advanced Computational Engine [11]. TRACE is primarily qualified to analyze the ESBWR design as well as BWR and PWR large and small break LOCAs accidents. Nevertheless, it is not the officially appropriate code for stability analysis, control rod ejections, or other operational transients [12].

2.3.5 CATHARE

CATHARE is a thermohydraulic code developed by CEA in cooperation with EDF, the former AREVA and the IRSN. Its full name is *Code for Analysis of THermalhydraulics during an Accident of Reactor and safety Evaluation*. The computational method is based on a two-phase fluid model with six equations, which are conservation equations of mass, energy and movement [13]. The code is capable of simulating the system behavior during a loss of coolant accident, steam generator rupture, feed water line break, residual heat removal failure or steam line break. Calculations can be performed on all types of reactors and few types of system loop and experimental facilities [10].

2.3.6 ATHLET

ATHLET, fully *Analysis of THermal-hydraulics of LEaks and Transient*, is the thermal-hydraulic code, developed by Gesellschaft für Anglen- und Reaktorsicherheit. Like other thermalhydraulic codes, ATHLET allows analysis of operational conditions, abnormal transients and all kinds of accidents in nuclear power plants [14]. The important feature of this software is the possibility to be coupled with other codes. Among these codes belong several reactor physics codes, for example SCALE, but also CFD codes, which can be further coupled with structural mechanics codes. Officially supported CFD codes include the ANSYS CFX, which can be coupled with the ANSYS Mech. However, it is possible to find studies where the coupling was achieved also with the ANSYS Fluent [15].

2.3.7 COCONEUT

COCONEUT is a new neutron scheme developed by TechnicAtome and it is based on existing neutronic codes APOLLO2, CRONOS2 and TRIPOLI4. The full name of this code is COre COnception NEUtronic Tool. The software is developed to design and optimize medium-power research reactors. The main objective of developing of this code is the connection between different neutronic codes, both in the results and in the calculations themselves [16].

2.3.8 SERPENT-2

SERPENT-2 is a multi-purpose three-dimensional particle transport code based on Monte Carlo method, developed at the VTT Technical Research Center of Finland. The development of this code began in 2004 and the first version of SERPENT was focused on simple reactor physics. The new version SERPENT-2 brought a several improvements. Thanks to this, SERPENT is able to solve traditional reactor physics, neutron and photon transport simulations, but also multi-physics simulations by using internal and external coupling [17]. In recent years, the development has focused on multi-physics simulations, including the coupling with the OpenFOAM CFD code. That kind of simulation starts by running a SERPENT-2 with uniform material-wise temperature and density distribution. Results from this calculation are passed to OpenFOAM that calculates new temperature and density distributions based on the fission heat source. The results from OpenFOAM are then sent back to SERPENT-2 that determines new fission heat distribution. The use of this iterative method brings more accurate results in reactor physics and new possibilities for the use of CFD codes in nuclear industry [18].

2.3.9 SCALE

SCALE is a package of neutronic codes that can be used for several types of analyses. Among these analyses there are: critical safety, reactor physics, radiation shielding, activation, depletion and decay, sensitive and uncertainty analysis. The development of this package started in 1969, when Oak Ridge National Laboratory started supporting US Atomic Energy Commission by using the new code KENO, which is a neutronic code based on Monte Carlo method and used for critical safety [19]. Nowadays SCALE contains a variety of computational modules with the possibility of using Monte Carlo or Deterministic transport solvers. For example, in the case of criticality analysis, among others, a hybrid 3D deterministic/Monte Carlo module named Sourcerer is used. SCALE also contains its own nuclear data library [16].

Chapter 3: The Computational Fluid Dynamics

The computation fluid dynamics (shortly CFD) is the mathematical modeling of fluids behavior using computer technology. This computation method is used in a wide range of research and in engineering applications. Because of this, there are several commercial software programs, the most famous are the ANSYS Fluent and the STAR-CCM+ codes. Depending on the application, there can be several open source software. In the case of nuclear engineering and research, the most used are OpenFOAM and Code_Saturne. Compared to the commercial software, these software programs have a less user-friendly environment and smaller applications capability.

3.1 Basic Equations Used in CFD

This following subchapter is based on information from the references [20] [21] [22] [23] [24]. In the CFD, we can find three basic equations. These equations are derived from the transport theory phenomena, where the balancing of quantities in the control volume is defined as Eq. (1). From the mathematical point of view, it is necessary to reflect different type of possible mechanisms that are expressed in implicit form on the right side of Eq. (1). One of the most important mechanisms is the convective transfer one. This mechanism may occur in cases when the required physical quantity is transferred by the fluid flow. Another important mechanism is based on the existence of a temperature, velocity, or concentration gradient.

$$\begin{Bmatrix} Accumulation \\ rate \end{Bmatrix} = \begin{Bmatrix} Input \\ rate \end{Bmatrix} - \begin{Bmatrix} Output \\ rate \end{Bmatrix} + \begin{Bmatrix} Production \\ rate \end{Bmatrix} \tag{1}$$

If we assume the variable P as a required balanced quantity in the general meaning, the balance equation can be written as Eq. (2). The following Figure 6 represents an idea of the control volume for the Eq. (2).

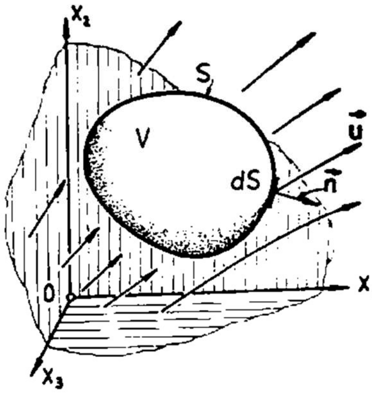

Figure 6 – *The stationary control volume in velocity field for Eq (2) [20]*

$$\frac{d}{dt}\int_V PdV = -\int_S \vec{n}\cdot\vec{u}\,PdS - \int_S \vec{n}\cdot\Pi dS + \int_V \dot{P}^{(g)}dV \qquad (2)$$

In Eq. (2) the left side member represents the accumulation rate; in other words, it is a change of the required balanced time dependent quantity. The first right side member shows the convective transfer through the boundary surface. The second right side member includes other types of transfers than the convective one and the last member is an example of the production rate. The new variable Π represents the flow of physical quantities through the unit of surface per unit of time by different mechanism than the convective one. After several mathematical modifications, the Eq. (2) can be written as partial differential Eq. (3).

$$\frac{\partial P}{\partial t} + \nabla\cdot(\vec{u}P) + \nabla\cdot\Pi - \dot{P}^{(g)} = 0 \qquad (3)$$

This equation is formed for the stationary control volume. The essential feature of this kind of control volume is the fact, that its shape and size are constant, but the amount of mass included inside of it can be changeable. This situation occurs in the case of compressible fluids, where their density is time dependent. This kind of control volume corresponds to the situation, where we measure the temperature of a liquid with a probe placed in a fixed position. In other words, we are receiving information about the temperature of different particles, which are going through this area within every time step. However, another way to define control volume exists, and it is referred as the movable control volume. This kind of the control volume moves in the fluid with its own velocity, independent from the fluid velocity. In some special cases, when the velocity of the movable control volume is the same as the velocity of the fluid, it is called the material control volume. Since this control volume has the same velocity as the fluid, we are basically always focused on the same particles of the fluid. It means, that the included mass in the control volume is constant, but the shape and the size of it can vary. By expressing Eq. (3) for this control volume we obtain Eq. (4):

$$\frac{DP}{Dt} + (\nabla\cdot\vec{u})P + \nabla\cdot\Pi - \dot{P}^{(g)} = 0 \qquad (4)$$

The first left side member is called the Lagrangian form of a material derivative and it describes the time rate of change of some physical quantities depending from position. Its equation is showed as Eq. (5):

$$\frac{DP}{Dt} = \frac{\partial P}{\partial t} + (\vec{u} \cdot \nabla)P \tag{5}$$

This kind of control volume can be observed if we use the same temperature measuring instrument like in the case of the stationary control volume, which corresponds to the first right side member Eq. (5). In the same moment, we will also use some other type of temperature measuring instrument, whose probe will be moving in the measured fluid with the same velocity as the fluid. This measured information would correspond with the second member of Eq (5).

Now, when we have general differential equations for both types of control volume, we can say that for the case of mass conservation equation, in other words continuity equation, the balanced physical quantity is the mass. Since the equation refers to a certain control volume, it refers also to a unit of volume, that means, the physical quantity is density. In the case of homogenous fluid, the mechanism of mass diffusion cannot exist, and the mass cannot appear or disappear: meaning, that the third and fourth member in the left side of the equations (3)(4) will be equal to zero. The continuity equation of a homogenous fluid is in general form documented as Eq. (6) for the stationary control volume and as Eq. (7) for the material control volume.

$$\frac{\partial \rho}{\partial t} + \nabla \cdot (\rho \vec{u}) = 0 \tag{6}$$

$$\frac{D\rho}{Dt} + \rho \nabla \cdot \vec{u} = 0 \tag{7}$$

The first left side member in the Eq. (6) shows the change in density in dependence on time; this situation occurs in the case of compressible fluids. For incompressible fluids, this member is equal to zero. The second member expresses the amount of the mass that enters and exits the control volume.

With the momentum equation, which is the second most important equation for CFD, the situation is similar. The balanced physical quantity is the momentum, which is defined as a multiple of the mass and the velocity of the fluid. As with the continuity equation, the physical quantity refers also to a unit of volume. After substituting the physical quantity into the Eq. (4), the equation for the momentum balance is showed as Eq. (8)

$$\frac{D(\rho\vec{u})}{Dt} + (\nabla \cdot \vec{u})\rho\vec{u} + \nabla \cdot \vec{\vec{\sigma}}^{*} - \rho\vec{f} = 0 \tag{8}$$

Unlike the continuity equation, the momentum can appear and disappear under the condition of the external forces. This fact is reflected by the fourth left side member Eq. (8). The momentum can be also transmitted between adjacent layers of the fluid. Since friction occurs, this phenomenon is represented as an internal tension in the control volume and in Eq. (8) is characterized by the third left side member. This equation after few mathematical modifications and after editing the internal tension member becomes Eq. (9):

$$\rho\frac{D\vec{u}}{Dt} = -\nabla p + \nabla \cdot \vec{\vec{\tau}} + \rho\vec{f} \tag{9}$$

In this equation, the left side member represents inertial forces. The first right side member describes the pressure forces and the second one stands for the forces of viscous friction. Unlike in the case of solids, where the internal tension is dependent on the strain, this situation is more complicated in the fluid dynamics. One of the basic functional dependencies for the viscous friction is called the Newton's viscosity law and it is showed as the Eq. (10).

$$\vec{\vec{\tau}} = \lambda\,\vec{\vec{\delta}}\; tr\,\vec{\vec{\Delta}} + 2\,\mu\,\vec{\vec{\Delta}} \tag{10}$$

This equation puts the shear stress and the strain rate into the linear dependence and all the fluids whose behavior corresponds to that are called the Newtonian fluids. The constant μ is called dynamic viscosity and its value depends on the type of fluid and the temperature. For the incompressible fluids the mathematical modeling is easier. Thanks to the fact that for incompressible fluids the trace of the strain rate is equal to zero, the Eq. (10) can be modified into a simple Eq. (11). For incompressible fluids, the shear stress tensor trace $tr\,\vec{\vec{\tau}}$ is also equal to zero.

$$\vec{\vec{\tau}} = 2\,\mu\,\vec{\vec{\Delta}} \tag{11}$$

However, for the compressible fluids it is necessary to know the value of the member λ in the Eq. (10). Since it is difficult to determine this value by experimental methods and considering the fact that the shear stress tensor trace could also be zero for the compressible fluids, the value of λ is determined as:

$$\lambda = -\frac{2}{3}\mu \qquad (12)$$

Due to this assumption, the Newton's law for the compressible fluids can be expressed as the Eq. (13).

$$\overset{\rightrightarrows}{\tau} = -\frac{2}{3}\mu\,\overset{\rightrightarrows}{\delta}\;tr\,\overset{\rightrightarrows}{\Delta} + 2\,\mu\,\overset{\rightrightarrows}{\Delta} \qquad (13)$$

The substitution of this law into the Eq. (9) results in the Navier-Stokes equation, which can be formulated as the Eq. (14).

$$\rho\frac{D\vec{u}}{Dt} = -\nabla p + \mu\,\nabla^2\vec{u} + \rho\overrightarrow{f} \qquad (14)$$

The Navier-Stokes equation is a non-linear partial differential equation. Together with the continuity equation, they form the system of equations to determine the velocity and the pressure fields of fluids. The non-linearity of the Navier-Stokes equation causes considerable problems in its solution. Since there are only few cases, where this equation can be solved exactly, in all the other cases it is necessary to use numerical methods. Both equations, which are mentioned in this chapter are derived for the laminar flow; in the case of turbulent flow, the whole situation is more complicated. This issue is further discussed in the next chapter.

The last important equation for this chapter is the energy equation. As well as two previous equations, also this one is based on the balance Eq. (4). The balanced physical quantity is the internal energy, which refers to the unit of volume. The changes in internal energy occur for several reasons; the heat transfer is one of them, and in the following energy equation it is represented by the heat flux. The heat transfer can occur by three different mechanisms, but the existence of a thermal gradient is essential for all of them. The first heat transfer mechanism mentioned in this paper is the heat conduction, which is based on the following Fourier's law:

$$\overrightarrow{q} = -h\nabla T \qquad (15)$$

The coefficient h in the Eq. (15) is the material thermal conductivity. The thermal conductivity for many types of materials is also highly dependent on the temperature. Another mechanism of the heat transfer is the thermal radiation. The following Stefan – Boltzmann law applies to this heat transfer mechanism, where $\sigma^{(s)}$ is Stefan – Boltzmann constant.

$$\vec{q} \cdot \vec{n} = \sigma^{(s)} T^4 \tag{16}$$

The equation (16) is valid for the so-called black body, which is a special theoretical case. For real bodies, the emissivity (ε_{irr}) parameter must be taken into account as well. An important note to this mechanism is the fact that heat transfer occurs between two surfaces at different temperatures independently on the environment between them. The last mechanism is the convection heat transfer. This kind of mechanism can occur only when the fluid is flowing. Based on the source of the fluid movement, we recognize two kinds of convection, the natural and the forced one. The law that describes this mechanism is the Newton's law of cooling and it is showed on the Eq. (17).

$$\vec{q} \cdot \vec{n} = \alpha(T_f - T_s) \tag{17}$$

The parameter α is called heat transfer coefficient, and it is a parameter highly dependent on many factors. The internal energy can also be generated by the mechanical friction or by the conversion from other types of energy, for example from the chemical reactions. After considering of all the previous mechanisms, substituting them into the Eq. (4), and after few mathematical modifications, the energy Eq. (18) is formed in the differential form.

$$\rho \frac{Du_E}{Dt} = -\nabla \cdot \vec{q} - p\nabla \cdot \vec{u} + \overset{\rightrightarrows}{\tau} : \overset{\rightrightarrows}{\Delta} + \dot{Q}^{(g)} \tag{18}$$

3.2 Turbulent Models

As mentioned in the previous subchapter, in the case of turbulent flow, the expression of the Navier-Stokes equation is slightly different. This is due to the existence of the fluctuating component of the velocity that results from turbulent eddies. The fluctuation velocity component can be thought of as the velocity component that oscillates around the instantaneous velocity mean value. The following Figure 7 and the Eq. (19) may help to illustrate the situation.

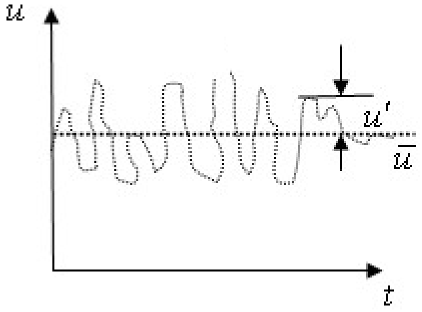

Figure 7 – *The record of the velocity during a turbulent flow [25]*

$$\overrightarrow{u} = \overline{\overrightarrow{u}} + \overrightarrow{u}' \tag{19}$$

In this Figure, u represents the value of the instantaneous velocity. This instantaneous velocity is composed by the value of the instantaneous mean velocity $\bar{u}$ and the fluctuation velocity component u'. Although the example is presented on velocity, this kind of phenomena may also occur with the other scalar quantities, like for example with the pressure [20] [24] [26].

The substitution of the previous Eq. (19) into the already derived Navier-Stokes equation for the laminar flow (14) produces the following Raynolds-averaged Navier-Stokes (shortly RANS) Eq. (20).

$$\rho \frac{D\overline{\overrightarrow{u}}}{Dt} = -\nabla\bar{p} + \mu\,\nabla^2\overline{\overrightarrow{u}} - \nabla\cdot(\rho\overline{\overrightarrow{u}'\overrightarrow{u}'}) + \rho\overrightarrow{f} \tag{20}$$

The new term in the Eq. (20) is called the tensor of turbulent stresses or also the Reynolds stresses tensor. This tensor can be expressed by the Eq. (21).

$$\overset{\rightrightarrows}{\tau}^{(t)} = -\rho\overline{\vec{u}'\vec{u}'} \tag{21}$$

With this tensor, a problem arises, because the modern theory of turbulence does not generally allow the formulation of dependency between the tensor and the time-averaged velocity gradients. This tensor must be modeled by using empirical and semi-empirical relationships, the so-called turbulent models [24] [26].

There are several types of approaches in the turbulent model theory. The most used ones are turbulent models based on the RANS equation. These models are further subdivided into models based on the linear eddy-viscosity, on the non-linear eddy-viscosity, and on the Reynolds stress transport. Other approaches are the Large eddy simulations (shortly LES), the Detached eddy simulations (shortly DES) and the Direct numerical simulations (shortly DNS) [24] [26].

3.2.1 The Reynolds-averaged Navier-Stokes models (RANS)

The advantage of the RANS models is their possible applicability for industrial simulations. The linear eddy-viscosity models are based on the Boussinesq hypothesis. This hypothesis says, that the turbulent stress tensor can be modeled by using the newly introduced turbulent viscosity $\mu^{(t)}$. This corresponds to the Eq. (22), which is based on the previous Eq. (21):

$$\overset{\rightrightarrows}{\tau}^{(t)} = 2\mu^{(t)}\overset{\rightrightarrows}{\Delta} - \frac{2}{3}\rho k\overset{\rightrightarrows}{\delta} \tag{22}$$

where $\overset{\rightrightarrows}{\Delta}$ is the mean strain rate tensor, which is defined as the Eq (23) for the compressible fluids and as the Eq. (24) for the incompressible fluids. The parameter k is called the mean turbulent kinetic energy and its mathematical expression is showed in Eq. (25) [24] [26].

$$\overset{\rightrightarrows}{\Delta} = \frac{1}{2}\left(\frac{\partial \bar{u}_i}{\partial x_j} + \frac{\partial \bar{u}_j}{\partial x_i}\right) - \frac{1}{3}\frac{\partial u_k}{\partial x_k}\overset{\rightrightarrows}{\delta} \tag{23}$$

$$\overset{\rightrightarrows}{\Delta} = \frac{1}{2}\left(\frac{\partial \bar{u}_i}{\partial x_j} + \frac{\partial \bar{u}_j}{\partial x_i}\right) \tag{24}$$

$$k = \frac{\overline{u'_i u'_i}}{2} \tag{25}$$

The simplest linear eddy-viscosity model are the algebraic turbulent models. Sometimes they are called zero-equations models, because they do not need any additional equations. They are based on functions that give the value of the turbulent viscosity directly from the flow variables. The most known algebraic models are *Cebeci-Smith model*, *Baldwin-Lomax model*, *Johnson-King model* and *A roughness-dependent model* [26].

The more advanced models are the one equation turbulent models, which are based on the solution of one turbulent transport equation. These models include the *Prandtl's model* and the *Spalar – Allmaras model*. While the Prandtl's model balances the turbulent kinetic energy k in its transport equation and applies it back for calculation of the turbulent kinematic viscosity and the turbulent dynamic viscosity, the Spalar-Allmaras model balances the modified turbulent viscosity $\tilde{\nu}$ and applies it back on calculation of the turbulent dynamic viscosity. Both transport equations are based on the Eq. (4) and their expressions are showed as the Eqs. (26) and (27) [26].

$$\frac{\partial}{\partial t}(\rho k) + \frac{\partial}{\partial x_j}(\rho k u_j) = \tau_{ij}\frac{\partial u_i}{\partial x_j} - C_D\frac{k^{\frac{3}{2}}}{l} + \frac{\partial}{\partial x_j}\left[\left(\nu + \frac{\nu_t}{\sigma_k}\right)\frac{\partial k}{\partial x_j}\right] \tag{26}$$

$$\begin{aligned}\frac{\partial}{\partial t}(\rho\tilde{\nu}) + \frac{\partial}{\partial x_i}(\rho\tilde{\nu}u_i) = \\ = G_v + \frac{1}{\sigma_{\tilde{\nu}}}\left[\frac{\partial}{\partial x_j}\left\{(\mu + \rho\tilde{\nu})\frac{\partial\tilde{\nu}}{\partial x_j}\right\} + C_{b2}\rho\left(\frac{\partial\tilde{\nu}}{\partial x_j}\right)^2\right] - Y_v + S_{\tilde{\nu}}\end{aligned} \tag{27}$$

As it can be seen from the equations, the turbulent models are highly dependent on many constants whose values are very often based on the experiments. Although these models are now quite less popular, the Spallar-Allmaras model is still widely used mainly in the aerospace industry [24].

The most used turbulent models nowadays are the two equations turbulent models like the k-omega and the k-epsilon ones in their all different modifications. As in the two previous cases, also these models are based on the Boussinesq hypothesis. In addition to one turbulent transport equation for the balance of the turbulent kinetic energy k, they have an added turbulent transport equation for the balance of another turbulent variable. In the case of the k-omega turbulent model, it is the so-called Specific turbulent dissipation rate ω and for the k-epsilon turbulent model, it is the Turbulent dissipation ε. The biggest weakness of these models is the Boussinesq hypothesis, which is not valid for strong curved, or strongly accelerated complex flows.

Both turbulent transport equations for the standard k-epsilon model are showed as the Eqs (28) and (29). K-epsilon model is less suitable for calculations involving large pressure gradients. Its original formulation has been improved over the years; in fact, in the modern CFD software, we can find its various modification: such as the Realisable k-epsilon or the RNG k-epsilon. These modifications bring improvements in the area of calculations focused on rapidly strained flows, swirling flows and separated flows. Over the years, this model has proven to be the most suitable for free-shear layers flows calculations [24] [26].

$$\frac{\partial}{\partial t}(\rho k) + \frac{\partial}{\partial x_i}(\rho k u_i) = \frac{\partial}{\partial x_j}\left[\left(\mu + \frac{\mu_t}{\sigma_k}\right)\frac{\partial k}{\partial x_j}\right] + P_k + P_b - \rho\epsilon - Y_M + S_k \tag{28}$$

$$\frac{\partial}{\partial t}(\rho \epsilon) + \frac{\partial}{\partial x_i}(\rho \epsilon u_i) = \frac{\partial}{\partial x_j}\left[\left(\mu + \frac{\mu_t}{\sigma_\epsilon}\right)\frac{\partial \epsilon}{\partial x_j}\right] + C_{1\epsilon}\frac{\epsilon}{k}(P_k + C_{3\epsilon}P_b) - C_{2\epsilon}\rho\frac{\epsilon^2}{k} + S_\epsilon \tag{29}$$

The k-omega model presented in this paper by the Eqs. (30) and (31) is more accurate for simulations in the near wall boundary regions. As well as k-epsilon model, also this model has been improved over the years and in additional to its standard version, we can find modified versions called the BSL k-omega model and the k-omega SST now. In comparison to the standard k-omega model, the BSL k-omega model brings improvements by implementation of the k-epsilon model and by using the blending function, which activate relevant model when is needed. The k-omega SST adds a hybrid approach for near-wall calculations [24] [26].

$$\frac{\partial}{\partial t}(\rho k) + \frac{\partial}{\partial x_i}(\rho k u_i) = \frac{\partial}{\partial x_j}\left[\left(\mu + \frac{\mu_t}{\sigma_k}\right)\frac{\partial k}{\partial x_j}\right] + G_k - Y_k + S_k \tag{30}$$

$$\frac{\partial}{\partial t}(\rho \omega) + \frac{\partial}{\partial x_i}(\rho \omega u_i) = \frac{\partial}{\partial x_j}\left[\left(\mu + \frac{\mu_t}{\sigma_\omega}\right)\frac{\partial \omega}{\partial x_j}\right] + G_\omega - Y_\omega + S_\omega \tag{31}$$

Another type of RANS-based turbulent models are the non-linear eddy-viscosity models. The Reynolds turbulent stress tensor is for these models generally defined as the Eq. (32).

$$\overset{\Rrightarrow}{\tau}^{(t)}{}_n = 2\mu^{(t)} f\left(\overset{\Rrightarrow}{\Delta}, \overset{\Rrightarrow}{\Omega}\right) \tag{32}$$

where the parameter $\overset{\Rrightarrow}{\Omega}$ is the mean vorticity tensor and it is defined as [20]:

$$\overset{\Rrightarrow}{\Omega} = \frac{1}{2}\left(\frac{\partial \bar{u}_i}{\partial x_j} - \frac{\partial \bar{u}_j}{\partial x_i}\right) \tag{33}$$

The shape of the resulting function of variables $\overset{\rightrightarrows}{\Delta}$ and $\overset{\rightrightarrows}{\Omega}$ depends on the specific model, which can be a quadratic or a cubic polynomial. In the case of the quadratic models, better results in the simulations of reproduced driven secondary flows are achieved compared to linear eddy viscosity models. The cubic models are more appropriate for simulations of strongly curved and swirling flows. Probably the best-known non-linear eddy-viscosity model is the *v2-f*. This model is similar to the well-known standard k-epsilon model. Besides the turbulent kinetic energy and turbulent dissipation, this model balances also the so-called wall-normal velocity fluctuation $\overline{v^2}$ and to model a behavior near the walls is use the elliptic relaxation function f. It is basically a four equations turbulent model. The two new equations corresponding to this model are presented for illustration in the Eqs. (34) and (35) [27] [28].

$$\frac{\partial}{\partial t}\left(\rho\overline{v^2}\right)+\frac{\partial}{\partial x_i}\left(\rho\overline{v^2}u_i\right)=kf-\frac{\overline{v^2}}{k}\epsilon+\frac{\partial}{\partial x_j}\left[\left(\nu+\frac{\nu_t}{\sigma_{\overline{v^2}}}\right)\frac{\partial\overline{v^2}}{\partial x_j}\right] \tag{34}$$

$$L^2\nabla^2 f-f=\frac{C_1-1}{T}\left(\frac{\overline{v^2}}{k}-\frac{2}{3}\right)-C_2\frac{P_k}{\epsilon} \tag{35}$$

The last type of the turbulent models based on the RANS equation is the Reynolds stress model, shortly RSM. This model solves directly the Reynolds stress numbers and the turbulent energy dissipation. In the case of 3D simulation, this turbulent model contains 7 equations, which make the most complex type of the RANS turbulent model. In comparison with the well-known turbulent models k-omega and k-epsilon, the RSM model has higher computational requirements and large convergence problems. Due to the fact that it is not based on the Boussinesq hypothesis, the RSM model is suitable for simulating phenomena such as flows with significant streamline curvature, flow separation, and swirling flows. For the illustration, the exact transport equation for this model is showed in the Eq. (36) [24] [26].

$$\begin{aligned}\frac{\partial}{\partial t}\left(\rho\overline{u_i'u_j'}\right)&+\frac{\partial}{\partial x_k}\left(\rho u_k\overline{u_i'u_j'}\right)\\&=-\frac{\partial}{\partial x_k}\left[\rho\overline{u_i'u_j'u_k'}+\overline{p'\left(\delta_{kj}u_i'+\delta_{ik}u_j'\right)}\right]+\frac{\partial}{\partial x_k}\left[\mu\frac{\partial}{\partial x_k}\left(\overline{u_i'u_j'}\right)\right]\\&\quad-\rho\left(\overline{u_i'u_k'}\frac{\partial u_j}{\partial x_k}+\overline{u_j'u_k'}\frac{\partial u_i}{\partial x_k}\right)+\overline{p'\left(\frac{\partial u_i'}{\partial x_j}+\frac{\partial u_j'}{\partial x_i}\right)}-2\mu\overline{\frac{\partial u_i'}{\partial x_k}\frac{\partial u_j'}{\partial x_k}}\\&\quad-2\rho\Omega_k\left(\overline{u_j'u_m'}\epsilon_{ikm}-\overline{u_i'u_m'}\epsilon_{jkm}\right)\end{aligned} \tag{36}$$

3.2.2 The Large eddy simulation models (LES)

The so-called Large eddy simulation (shortly LES) models bring a completely different method for calculations of turbulent flows. These models are based on the Filtered Navier-Stokes equation. It means, that a filter is applied to the Navier-Stokes equation, which removes small eddies and considers only the large ones, which affect the momentum, the mass, and the energy of the flow. The small eddies, that are neglected in the Filtered Navier-Stokes equation, are further modeled by the subgrid-scale models. These subgrid-scale models are usually based on the Boussinesq hypothesis. In comparison with the RANS models, the LES models need a much finer mesh, which significantly increases computational requirements. However, due to the considerable development of the computer technology, this method is applied more frequently than before. An example of the Filtered Navier-Stokes equation is documented in the Eq. (37) [24] [26].

$$\frac{\partial}{\partial t}(\rho\overline{u_i}) + \frac{\partial}{\partial x_i}\left(\rho\overline{u_i}\,\overline{u_j}\right) = -\frac{\partial\bar{p}}{\partial x_i} + 2\frac{\partial}{\partial x_j}\left(\mu\overline{\overrightarrow{\overrightarrow{\Delta}}}\right) + \frac{\partial\tau_{ij}}{\partial x_j} \qquad (37)$$

3.2.3 The Detached eddy simulation models (DES)

A combination of the RANS and the LES approach creates the Detached eddy simulations, shortly DES. These methods are combined in the way that the RANS approach is applied to the boundary layer, while the LES is applied to the eddy regions. The DES was originally designed to work with the RANS Spalart-Allmaras model. Nowadays, such models as the Realizable k-epsilon, the BSL and SST k-omega, and the Transition SST model are available. Although the hybrid approach of this model reduces mesh requirements compared to the LES approach, the DES models are still highly computationally demanding. The application of this model has proved to be particularly suitable for aerodynamic simulations, where the high-Reynolds numbers occur [24] [26].

The most accurate method for dealing with turbulent flow is the Direct numerical simulation, shortly DNS. The method is based on the direct numerical solution of the Navier-Stokes equation. No turbulent models are used and the whole range of eddies is directly solved, which means that the mesh requirements are enormous. The three-dimensional DNS requires for the number of mesh points are defined by the Eq. (38).

$$N^3 \geq Re^{9/4} \qquad (38)$$

This means, that for the simulation of flow with the Reynolds number around 4000 the required size of meshes is over $64 \cdot 10^9$ elements. This model is a subject for the academic research rather than for the industrial applications [26].

3.3 Types of mesh elements and forms

Many CFD software use the finite volume method. The basic idea of this method is to divide a given domain into a finite number of volumes using a computer mesh. The differential equations that were mentioned in the previous subchapter are replaced by a system of algebraic equations for each volume using the discretization methods. In the case of 2D problems, there are triangular and quadrilateral elements. For 3D problems, tetrahedral, hexahedral, polyhedral, pyramid, or wedge are used. The modern software also allows the combination of different kinds of elements in the so-called hybrid mesh.

Each type of elements has different properties. Tetrahedral elements are suitable for complicated geometries, and they are supported by most of the mesh software. Their disadvantage is the final number of elements that are required to create the mesh for a given geometry compared to other types of elements; the final number of elements is directly related to the amount of RAM memory that must be allocated for the calculation, which may affect the necessary computational time. When using automatically generated tetrahedral meshes, a poorer quality is achieved, which further affects the convergence properties of the calculation and its accuracy. Hexahedral elements are a compromise between tetrahedral and polyhedral elements. They provide more accurate results at lower density of meshes for some cases of geometries. The polyhedral elements can fill the computational domain more effectively compared to the above-mentioned elements. Furthermore, it is possible to achieve the best convergence and calculation requiring a lower number of elements compared to hexahedral and tetrahedral elements [29]. The shape of individual elements is documented in the following Figure 8.

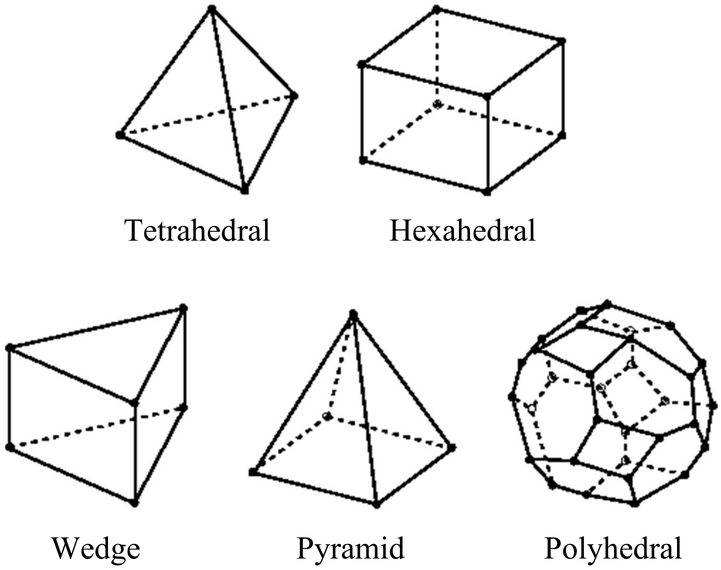

Figure 8 – *The element types [30]*

These elements can be formed either in structured or unstructured meshes. Historically, due to the computer background at that time, structured meshes were mainly used. Elements that can be formed into a structured mesh include quadrilateral and triangular elements for 2D. In the case of 3D, there are mainly hexahedral elements, and in some specific cases, it is possible to use pyramid or wedge elements. The following description of the structured mesh is given on 2D for simplicity. Each node of the mesh is defined by the integers i and j that represent the location of the node in the coordinate system of the computing domain. If it is a structured mesh, it is possible to create a relation between i and j values of neighbouring elements and thus reduce the overall memory requirements. Another advantage of structurally formed meshes is the high degree of mesh control. However, such meshes can be created only in the case of very simple geometries which are not attractive from the point of view of modern industry. The multi-block meshes are the answer for certain types of geometry; they allow the creation of a structured mesh for an individual block of a given geometry. Here, the element-to-element relationships are created for each block separately; this is less efficient than a one-block arrangement. On the other hand, the unstructured mesh form is capable of capturing even the most complicated geometry. It is generated automatically based on prescribed algorithms, that reduce the necessary knowledge for mesh creation and the time needed for its creation is noticeably shorter. The visual difference between a structured and unstructured mesh is shown in the following Figure 9 [31] [32].

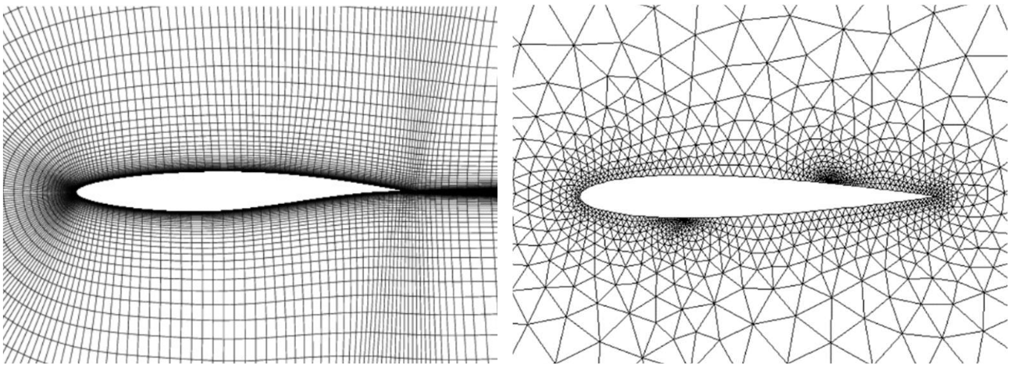

Structured mesh Unstructured mesh

Figure 9 – *The structured and unstructured 2D mesh of the aircraft wing profile [33] [34]*

In the case of meshes made up of several blocks, it is possible to define two types of mesh connection at the interface of these blocks, independently of whether the individual blocks are structured or unstructured. The first one is the conformal interface, which requires the same number and position of nodes on both blocks at their contact surface. No additional interpolation of the values is required with such a type of interface; this positively affects the speed and accuracy of the calculation. This type of interface corresponds to the structured mesh that is shown in Figure 9, which is composed of several blocks. The second type of the interface is non-conformal interface, which does not qualify for a conformal interface. The advantage of this interface is the possibility of changing only a specific block without the need to generate the mesh of the whole geometry; this feature is beneficial, for example, in the case of dynamic meshes. It is also possible to connect meshes with different elements using both interfaces; such meshes are called hybrid ones, and they are suitable for larger models where we try to use the advantage of individual types [35].

3.4 The mesh quality

The mesh quality has a significant influence on the calculation process, the speed of convergence and the accuracy of the subsequent results. The mesh elements are designed to be as efficient as possible for their ideal shapes; for the 2D, it is equilateral triangles or squares, for 3D regular or isosceles tetrahedron and cube are the ideal shapes. The criteria for assessing the mesh quality are based on differences between real mesh elements and the ideal ones. There are several quality assessment criteria; in the software package ANSYS we can find, for example, the skewness, which compares the actual volume of the element with the ideal one or the jacobian ratio, which indicates the deviation of the actual shape from the ideal one. A more detailed description of the criteria is given only for the aspect ratio and the orthogonal quality due to their later application.

The orthogonal quality of the mesh elements is determined using normal wall vectors, vectors coming from the centre of gravity of the element into the centre of gravity of the surrounding elements and vectors coming from the centre of gravity of the element to the element surfaces. For clarity, Figure 10 below shows the position of described vectors. The green ones represent the normal vector of the wall; the blue ones are connecting the centres of gravity and the red ones the centre of gravity to the surface.

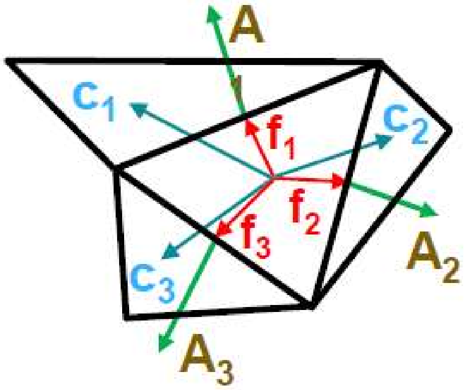

Figure 10 – *The vectors in the element for the definition of the orthogonal quality [36]*

The resulting orthogonal quality is determined in the interval from 0 to 1 using the formula (39). The spectrum representing the acceptability of the achieved quality for the CFD solver ANSYS Fluent is documented on the following Figure 11 *[36]*.

$$\min\left(\frac{A_i \cdot f_i}{|\vec{A_i}||\vec{f_i}|}, \frac{A_i \cdot c_i}{|\vec{A_i}||\vec{c_i}|}\right) \tag{39}$$

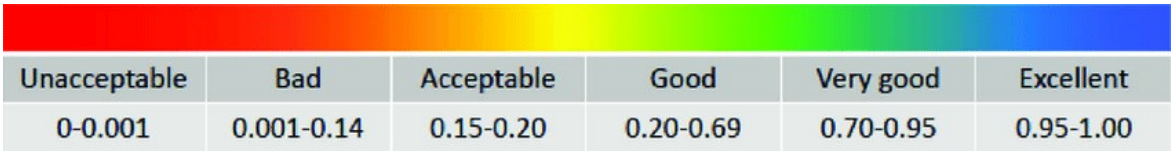

Unacceptable	Bad	Acceptable	Good	Very good	Excellent
0-0.001	0.001-0.14	0.15-0.20	0.20-0.69	0.70-0.95	0.95-1.00

Figure 11 – *The spectrum of the ANSYS Fluent orthogonal quality [37]*

The aspect ratio criterion characterizes the stretching of an element. It is determined as the ratio of the following distances; the normal distance between the centroid of the element and the centroid of the element wall, and the distance between the centroid of the element and the node of the element. For clarity, the following Figure 12 shows the described distances in the element [38].

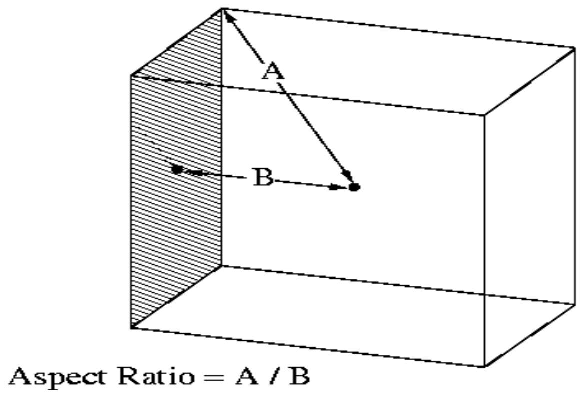

Figure 12 – *Definiton of the aspect ratio [38]*

According to the ANSYS documentation, the maximum recommended value of the aspect ratio is around 10, depending on the type of element. However, there are some cases where a mesh with the aspect ratio values of up to 10 000 can be used. It is acceptable in the cases when the flow is aligned along with stretched elements and if there is no substantial flow variation [24].

3.5 The near wall modeling, wall function

The near-wall flow modelling is highly problematic from the physical and numeric point of views. In addition to the no-slip condition, in other words, the zero velocity near the wall, which is associated with the occurrence of large velocity gradients, the turbulence itself in this area is very complicated to describe by mathematical models. However, the flow in this area has a significant impact on the remaining free flow; walls are the primary source of vorticity and turbulence. From the analytical point of view, the flow region near the wall is divided into three layers [24].

The closest one to the wall is the viscous sublayer; there are mostly viscous effects, and in this sublayer the turbulent kinetic energy is getting dissipated rather than produced. The outer sublayer of the near-wall area is the so-called log-law region or sometimes also the fully turbulent region. As it is evident from the name, in this area turbulences are dominant in the transmission phenomena, and the logarithmic law determines the resulting flow character. Between these two layers, there is a transition sublayer called the buffer layer. A graphical representation of the subdivision of the Near-wall region into sublayers is shown in Figure 13.

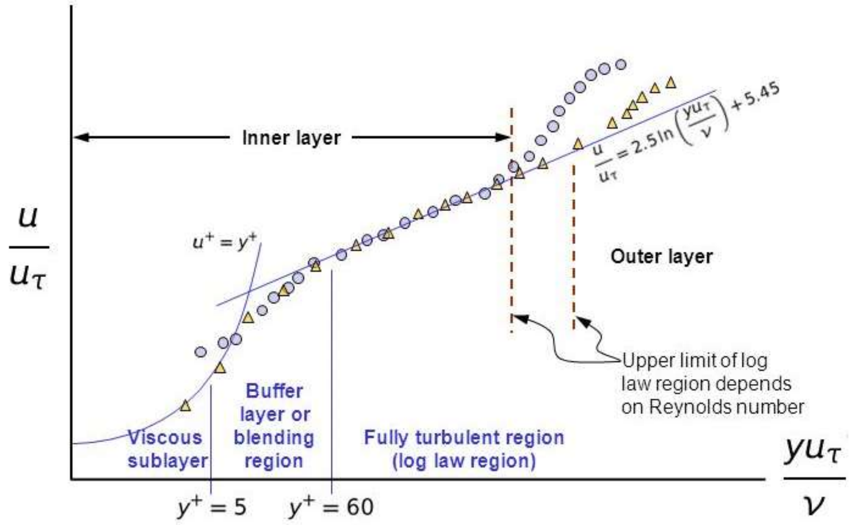

Figure 13 – *Subdivision of the Near-wall region [39]*

As can be seen from the previous description, there are three different types of fluid behaviour in the area near the wall. It means that we need to have three different treatments for each layer. It is necessary to know in what area we are to apply the right treatment. Two dimensionless units have been introduced for this purpose; the first one is the dimensionless wall unit y^+ and is described by the following equation (40) [24].

$$y^+ = \frac{u_\tau y}{\nu} \tag{40}$$

Where y is the distance to the nearest wall, u_τ is the friction velocity, and v is the kinematic viscosity of the fluid. The second dimensionless unit is the dimensionless fluid speed; the unit is represented by the letter u^+, and its mathematical expression is given as the following equation (41) [24].

$$u^+ = \frac{u}{u_\tau} \tag{41}$$

The friction velocity u_τ is defined as the following equation (42) for both of these dimensionless units [24].

$$u_\tau = \sqrt{\frac{\tau_w}{\rho}} \tag{42}$$

Unfortunately, only two of the three layers are described mathematically. Specifically, it is the viscous sublayer and the area of log law. The buffer layer is complicated to describe because of the complex balance between the driving forces in viscous sublayer and the area of log law.

There are two different types of flow modelling approach near the wall. The first approach focuses directly on modelling near the wall, and it is generally called the near-wall model approach. The mesh density is sufficient to cover all areas near the wall, especially the viscous sublayer. This approach requires that the first cell from the wall must reach the y^+ value equal to 1 or even less. The second one is the wall function approach. The wall functions are based on semi-empirical relationships that cover the effect of the entire inner layer near the wall. This approach rapidly reduces the mesh density. The main requirement is that the first layer of cells from the wall covers the entire inner layer. Depending on the applied wall function, the y^+ value of the first wall cell is required to be at least equal to 30. The mesh requirements depending on the used approach, are illustrated in the following Figure 14 [40].

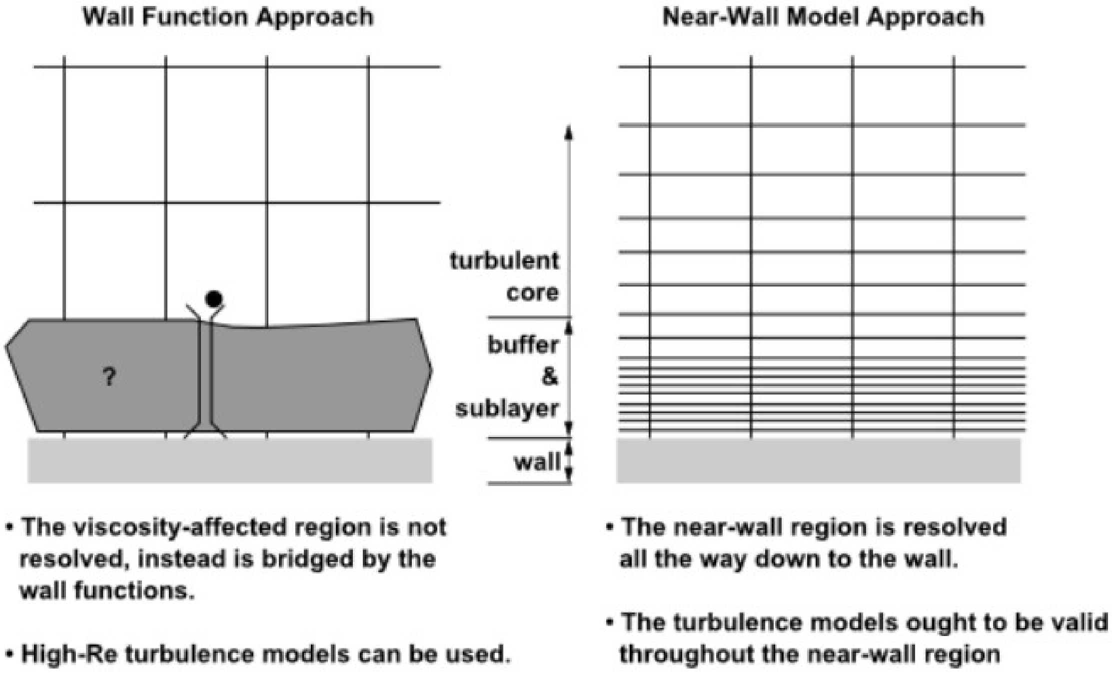

Figure 14 – *The near-wall approach [41]*

For these two historical approaches, the interval y^+ values between 5 and 15 is particularly problematic. Because of this, advanced approaches to modelling near-wall phenomena have been developed within ANSYS Fluent software. For the two-equation model k-e, they are the Menter-Lechner and Enhanced Wall Treatment, which allow to run this model independently from the y^+ value [24].

The Enhanced Wall Treatment combines two-layer model with the enhanced wall functions. This means that if the mesh density near the wall is sufficient, i.e. the y^+ value is equal to 1, the near model approach is applied. The wall functions are applied in the areas where the mesh is coarse. For the buffer zone, the blending function is applicated. This function allows a smooth transition between low Reynolds number model and wall functions. The blending function is based on granting a weighting factor depending on the value of y^+; for example, if y^+ equals to 1, the weighting factor is zero, and the low Reynolds number model is used for calculations. This can be mathematically expressed by the following equation (43) [24]

$$u^+ = e^{\Gamma} u^+_{lam} + e^{1/\Gamma} u^+_{turb} \tag{43}$$

where the Γ represents a weighting factor which can be determined by the following equation (44) [41].

$$\Gamma = -\frac{0{,}01(y^+)^4}{1+5y^+} \tag{44}$$

Chapter 4: The Thermohydraulic Analysis of the New European Fuel Assembly

The chapter is focused on the thermohydraulic analysis made by the CFD code named ANSYS Fluent. This chapter includes a description of the simplification of the geometry, a description of the required mesh and a discussion about results. The calculations were performed for three different levels of accuracy. The first one is focused only on the channels between fuel plates, and it is considered the simplest one. The second one includes the geometry of the top and bottom nozzle parts. Finally, the third one takes into account also the geometry of the fuel channel in the reactor LVR-15. The results of this analysis are also compared to the report made by TechnicAtome using the CATHARE code. All the computing work was done on the DELL Precision Tower 3620 workstation, featuring a 4-core Intel Core i7-7700 processor with a base frequency of 3.6 GHz and 64 GB of RAM.

4.1 The simplification of the geometry

The TechnicAtome provided the 3D model in STEP format. The model is composed of the 22 fuel plates, which will be made by aluminum alloy with uranium meat in the center of each plate. The other parts provide the mechanical stability and proper water flow; between these parts, there are the side plates, the top and bottom nozzle parts. In this model, several modifications were made for simplified geometry for the purpose of simpler mesh. These modifications were primarily focused on small blended and chamfered edges, which may uselessly increase the needed mesh density in these areas. The several examples of modifications are documented in the following Figures 15 and 16.

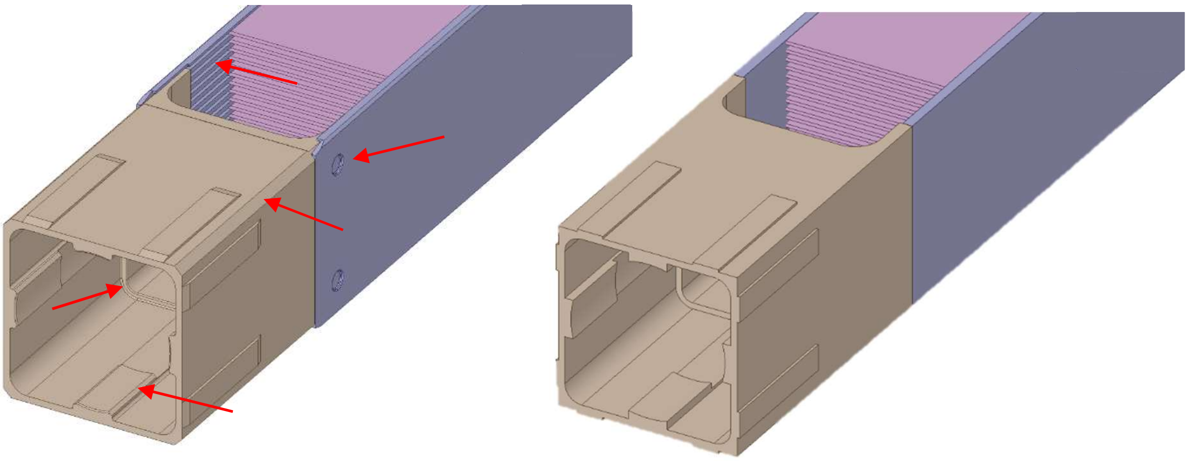

Figure 15 – *The modifications in the top nozzle area*

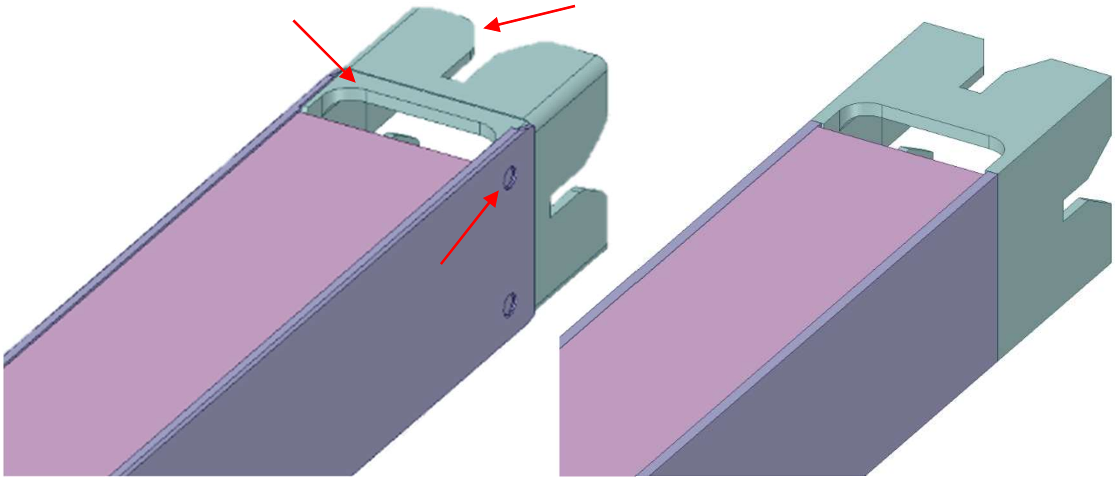

Figure 16 – *The modifications in the bottom nozzle area*

Because of the symmetric character of this fuel assembly, only one quarter was simulated. As a next step for the geometry, the inverse volume was created using another software from the ANSYS pack called the DesignModerel. This inverse volume represents the water mass, and it is necessary for creating a computational mesh. For structural mesh, the volume of each channel between the fuel plates is divided into 6 subvolumes. The inverse volume of top and bottom nozzle part is needed to connect two different types of mesh elements also is divided into several subvolumes.

4.2 The CERCA mesh parameters

The flow domains were divided into several subvolumes, as mentioned in the previous subchapter. Two types of mesh elements were applied to these subvolumes of the flow domains. The first ones are hexahedral elements in a structured configuration, the second ones are polyhedral elements. In the area of the top and bottom nozzle parts, the prismatic elements are applied close to the walls. The transition between the hexahedral and the polyhedral region is formed through transition elements. The description and properties of these types of elements are given in the previous chapter *The Computational Fluid Dynamics*. For the creation of the mesh, the so-called program ANSYS Meshing from the ANSYS software package was used. Since the ANSYS Meshing allows generating only tetrahedral, hexahedral, and prismatic elements, it was necessary to use another software to convert tetrahedral elements to polyhedral ones. For this purpose, it was possible to use the ANSYS Fluent, which has a function called *Converting the Domain to a Polyhedra*. This function allows the conversion of tetrahedral and prismatic elements to polyhedral ones, while keeping hexahedral elements in the case of a multi-element mesh. [42]

The introduction to this chapter states that several levels of accuracy have been used, and several types of meshes are corresponding to this. A sensitivity analysis was performed on the first level of the accuracy model. The mesh of this model consists entirely of hexahedral elements in a structural order. The mesh analysis was performed on one half of the channel using the symmetry boundary condition; the simulated geometry is documented in Figure 17. The physical parameters were corresponding to a pressure of 1.32 bar and a temperature of 40 °C. These values were chosen for two reasons. The first of them is for the purpose of validation with the thermohydraulic model made by the TechnicAtome, where the same values were used. The second one is the indication of the pressure value of 1.32 bar stated in the original report on the IRT-4M FA [43]. The turbulent model was the k-epsilon model with EWT. The input velocity into the channel was chosen as 2.5 $m \cdot s^{-1}$, which corresponds to the mean value from the interval of the following hydraulic characteristics. The analysis of the mesh was mainly focused on its sensitivity in dependence on the number of elements in the longitudinal direction of the channels. By analyzing in this direction, it was possible to reduce the total required number of elements, mainly thanks to the flow character in this area that is not changing its current in the channels. Another analyzed mesh parameters were the required number of elements per channel width and thickness. In the case of the analysis of the number of elements per channel thickness, the dependence between the number of elements and the achieved value of the parameter y^+ was examined. The results of the analyzes are represented in the following Figures 18, 19 and 20. To better understand the analyzed directions, Figure 17 is attached. Of the represented values, 13 elements were selected in the y-direction, 69 elements in the x-direction and 270 elements in the z-direction. The final mesh is documented together with a detailed recording of the beginning of the channels in the following Figure 21.

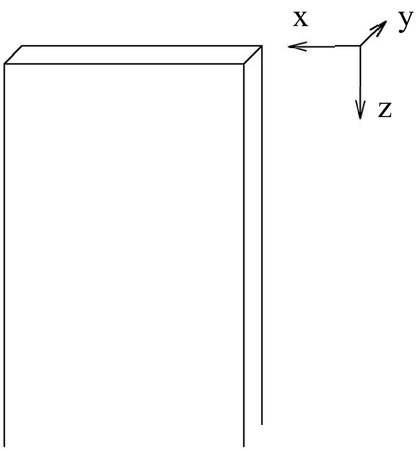

Figure 17 – *The simulated geometry for the CERCA FA model sensitivity analysis*

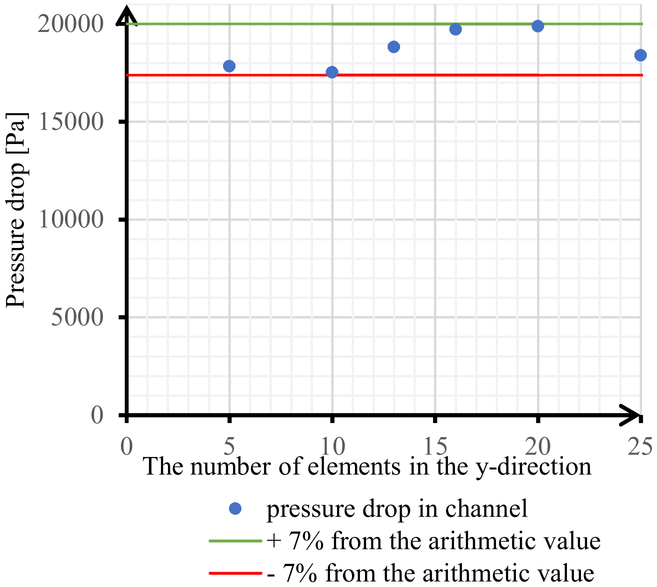

Figure 18 – *The mesh sensitivity analysis in the y-direction for the CERCA FA*

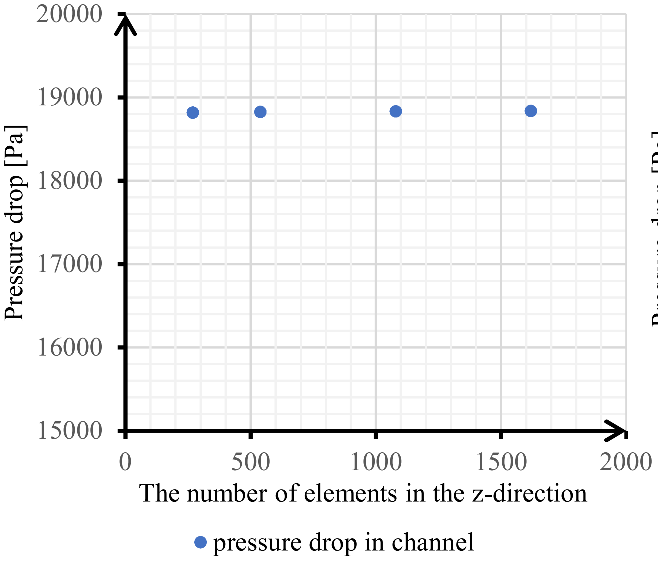

Figure 19 – *The mesh sensitivity analysis in the z-direction for the CERCA FA*

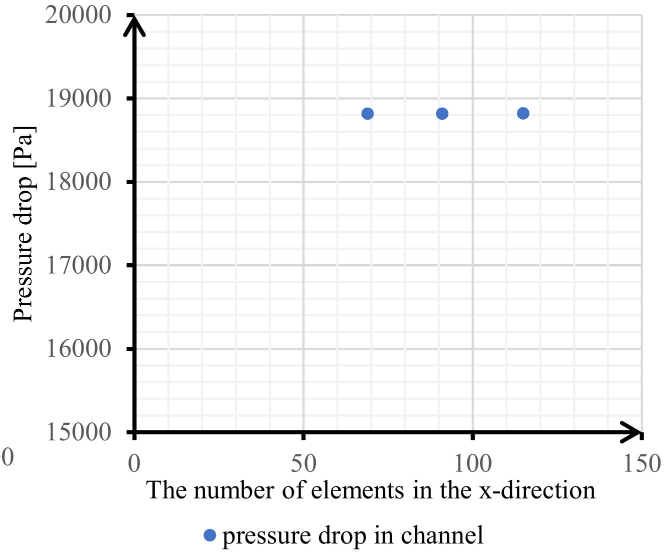

Figure 20 – *The mesh sensitivity analysis in the x-direction for the CERCA FA*

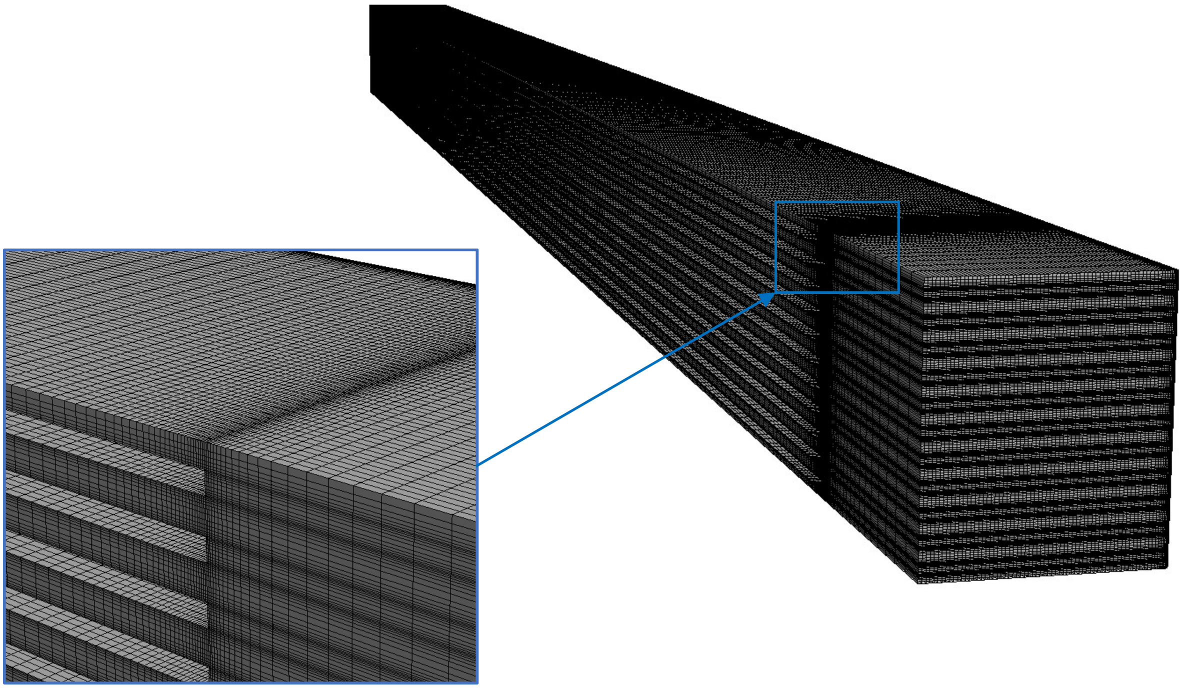

Figure 21 – *The 3D structured mesh of the first level of accuracy, the model of the CERCA FA active part channels mesh*

The quality of the mesh was assessed according to the achieved orthogonal quality and aspect ratio values. Since these are structured hexahedral meshes made by rectangular hexahedron elements, the value of the orthogonal quality is equal to one for all elements in this model. The achieved aspect ratio values are shown in the following Figure 22. The mesh contains a total of 3 973 231 hexahedral elements.

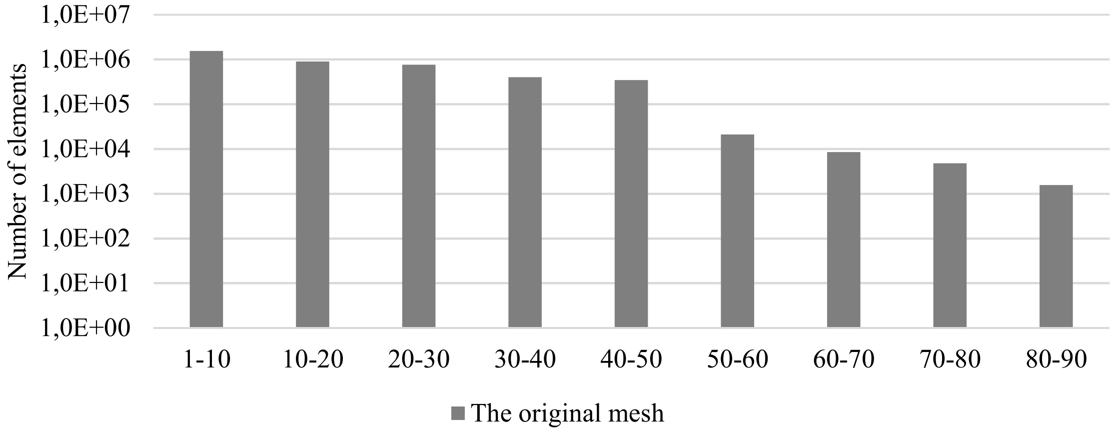

Figure 22 – *The achieved aspect ratio values of the CERCA FA active part channels mesh*

The other mesh documented below corresponds to the entire internal geometry of the fuel assembly. Due to the complicated geometry of the top and bottom nozzle parts, it was necessary to apply a non-structural tetrahedral mesh in these areas. These regions of the tetrahedral elements were later converted to the polyhedral elements using ANSYS Fluent. The channel part of the model is composed of the structured mesh of the hexahedral elements with the same parameter as in the previous case. Due to the element's conversion, the non-conformal interface was created between the active part of the FA and the top and bottom nozzle parts. The effect of this type of interface on the results is evaluated below. A preview of this mesh is documented in the following Figure 23.

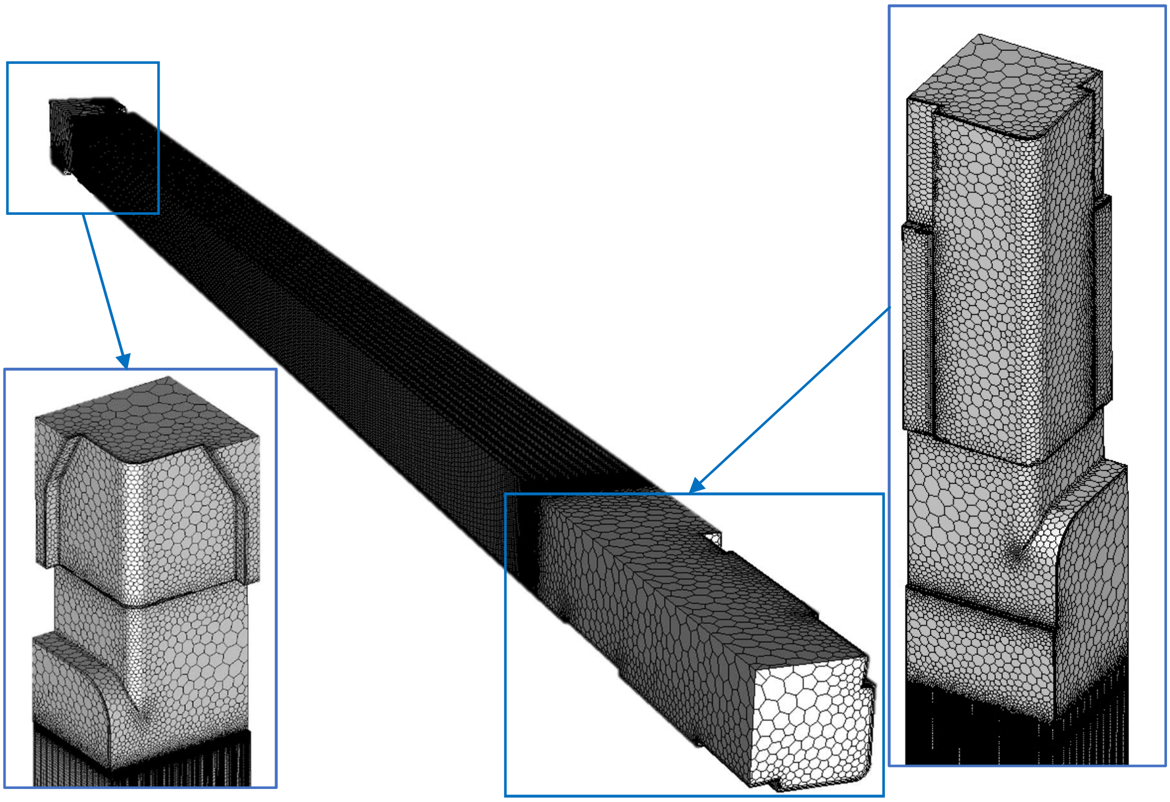

Figure 23 – *The 3D mesh of the second level of accuracy,the CERCA FA inside volume mesh*

This mesh contains a total of 3 950 748 elements. As in the previous model, the mesh quality was assessed using orthogonal quality and aspect ratio. In this case the tetrahedral elements were transformed to polyhedral ones, the following Figures 24 and 25 of the orthogonal quality and the aspect ratio show the difference; the original mesh, the crosshatched line, reached a total of 4 676 236 elements.

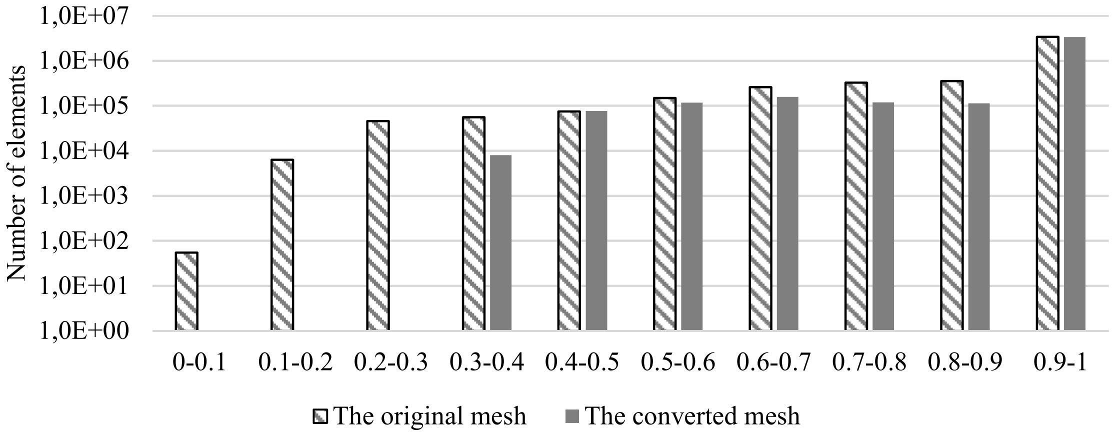

Figure 24 – *The achieved orthogonal quality of the the CERCA FA inside volume mesh*

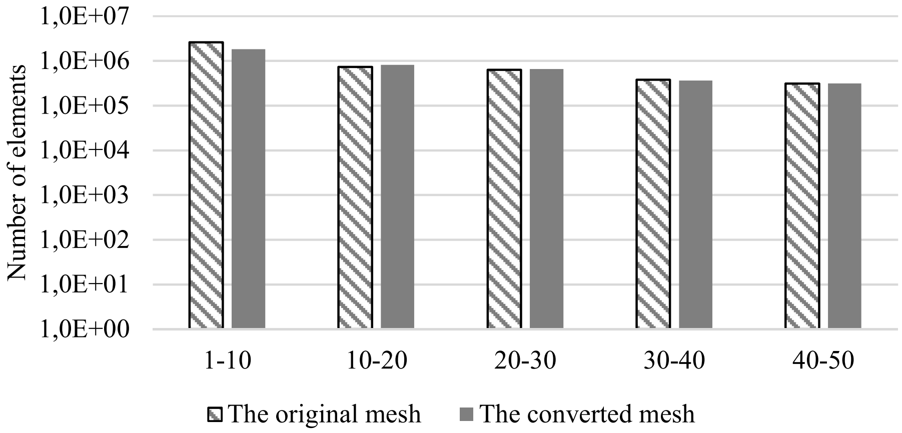

Figure 25 – *The achieved aspect ratio values of the CERCA FA inside volume mesh*

As showed in the Figures, the transformation of tetrahedral elements into polyhedral elements resulted in a decrease in the total number of elements and in an overall improvement in mesh quality.

The following mesh represents the fuel assembly at a specific core position of the reactor LVR-15; more specifically, it also includes the flow of water around the fuel assembly. The mesh was created similarly as in the previous case, i.e. using the structured hexahedral mesh of the active part of the fuel assembly and the tetrahedral elements, which were further transformed into polyhedral elements. The original mesh of tetrahedral elements and the mesh of polyhedral elements are shown in the Figures below.

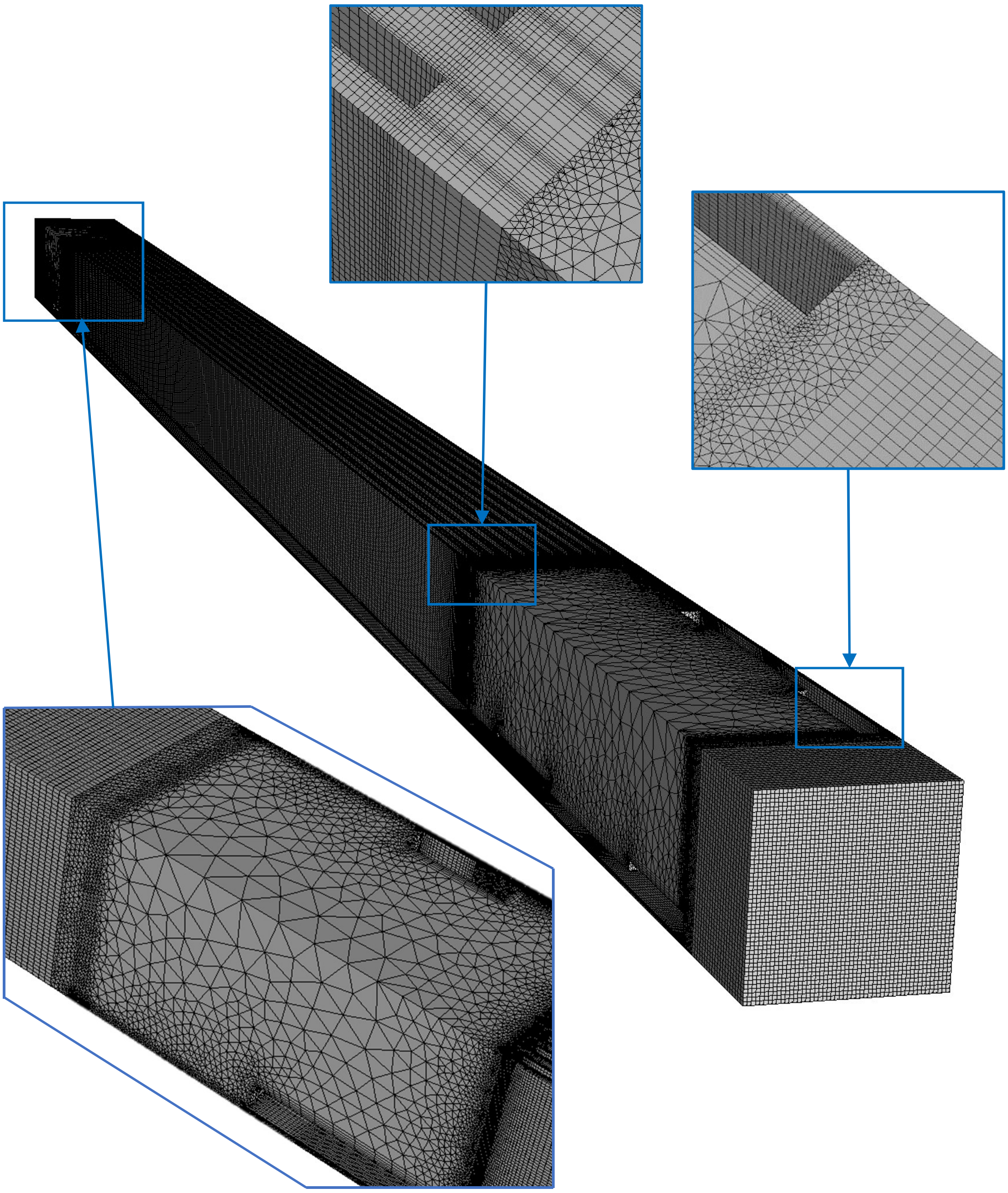

Figure 26 – *The 3D mesh of the third level of accuracy, the CERCA FA model including the outer flow, tetrahedral elements*

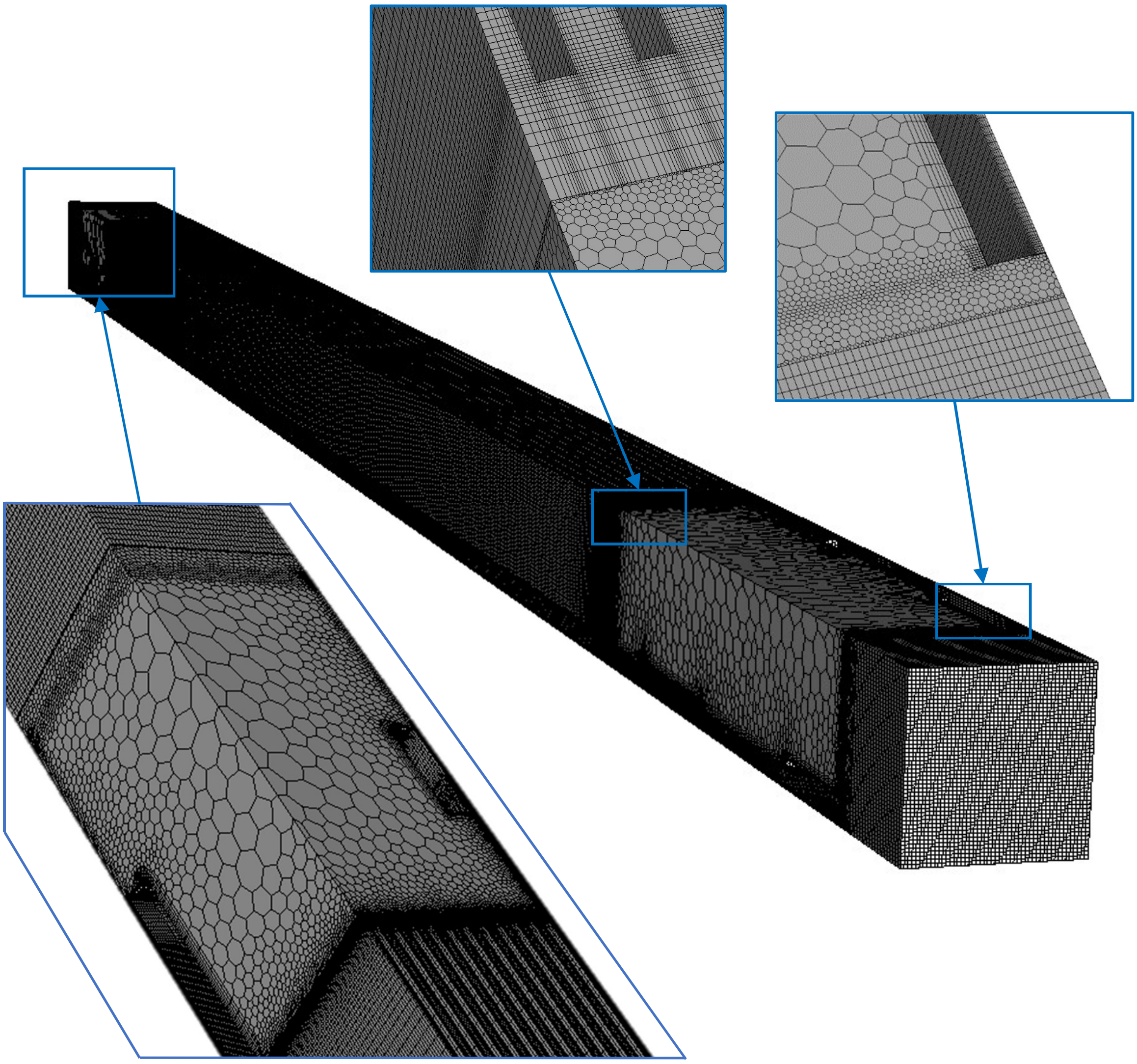

Figure 27 – *The 3D mesh of the third level of accuracy, the CERCA FA model including the outer flow*

This mesh contains 5 380 470 elements in the case of using polyhedral ones in specific areas and 6 674 584 in the case of using tetrahedral ones instead of them. The following Figures 28 and 29 are showing the achieved mesh quality.

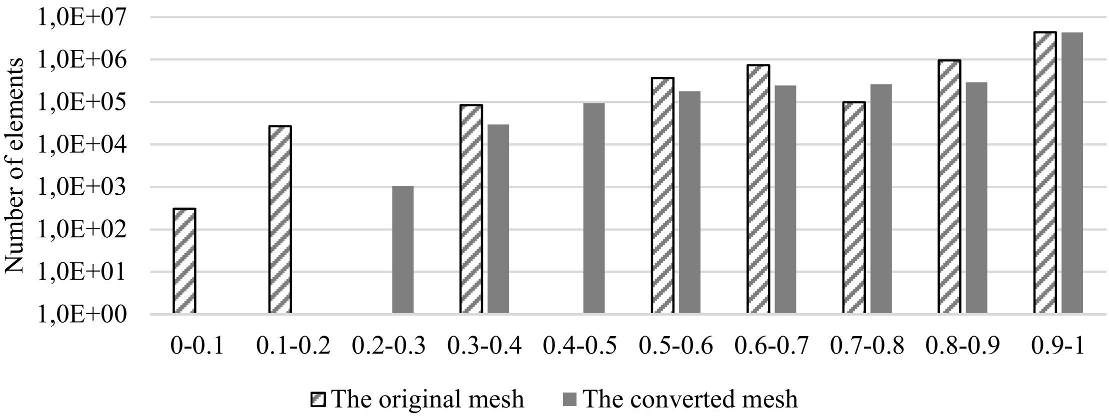

Figure 28 – *The achieved orthogonal quality of the CERCA FA mesh including the outer flow*

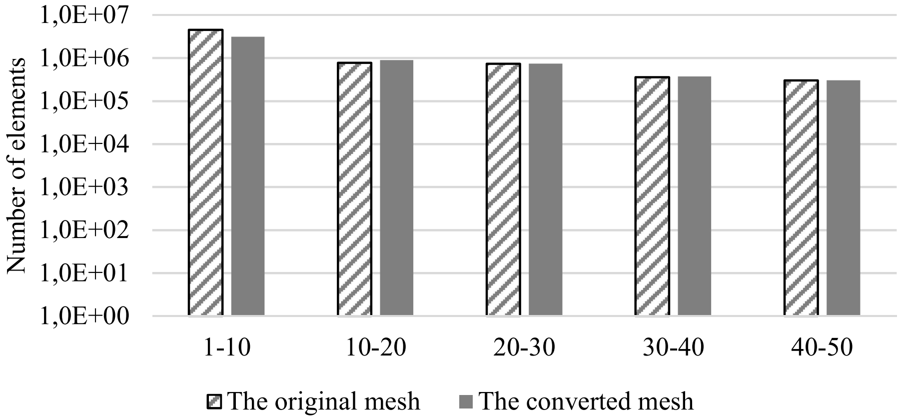

Figure 29 – *The achieved aspect ratio values of the CERCA FA mesh including the outer flow*

In addition to the decrease in the number elements, the quality of the mesh improved as well. Several calculations were performed on the tetrahedral mesh and subsequently on the polyhedral mesh resulting from the transformation, to compare the effect of the results due to the transformation of the elements. The results showed that the transformation of the tetrahedral elements to polyhedral ones and the non-conformal interface had no negative impact on simulation results.

4.3 The CERCA solver setting

The same solver setting was used on all three models. The ANSYS Fluent CFD solver in double precision mode was used for calculations. Pressure based solver, which is historically used for low velocities and incompressible flows, has been chosen as a numerical method. As with the density-based solver, the velocity field is obtained from the momentum equation. The pressure field is obtained from the pressure correction equation, which is given by continuity and momentum equations. RANS Realizable k-e model is used as turbulent model; its description is available in the previous subchapter *3.2 Turbulent models*. This turbulent model was chosen because of the possible application of the Enhanced wall treatment approach; the main advantage of this approach is also described in the previous subchapter. The simulated fluid is water, whose physical parameters were obtained from the online table of water thermodynamic properties [44]. The boundary condition at the model entry was chosen as *velocity inlet* with the mean velocity perpendicular to this area. At the output of the model, the *pressure outlet* was selected as the boundary condition. The turbulent parameters in these areas are not known; for this reason, they were kept by default as a turbulent intensity equal to 5 % and a turbulent viscosity ratio equal to 10. The coupled algorithm was chosen as an algorithm for solving velocity and pressure fields. The warped-face gradient correction was chosen for calculation stability. This correction is recommended for calculations on polyhedral elements, hexahedral elements and on hybrid meshes with high aspect ratios. Only the velocity and pressure fields are solved; the energy equation is not applied. The first-order upwind interpolation scheme was applied for the momentum equation, the turbulent kinetic energy equation and the turbulent dissipation rate equation simulate the first 100 iterations. After the start-up, these schemes were switched to the generally recommended second-order upwind interpolation scheme. The default interpolation scheme of the second-order was chosen for pressure and the least squares cell-based for gradient. The relaxation factors were kept as default because the simulation progress was stable. The hybrid initialization was chosen as the initialization method because it is more suitable for single-phase and steady-state simulations. For an overview, the solver settings are summarized in the following table 3; the chosen specific thermodynamic parameters of water are given in table 4.

Table 3 – *Summary of the ANSYS Fluent solver settings*

ANSYS Fluent		
General	Pressure based solver Steady Gravity in z axis	
Models	Viscous model	k-ε Realizable (Enhanced Wall Treatment)
	Energy	off
Material	Fluid – water	
Boundary conditions	Velocity inlet	Velocity magnitude (different values)
	Symmetry	¼ of the FA
	Wall	Default setting
	Pressure outlet	Gauge pressure (0 Pa)
	Turbulence	Intensity and Viscosity Ratio with default values
Solution methods	Scheme	Coupled
	Gradient	Least Squares Cell Based
	Pressure	Second Order
	Momentum	Second Order Upwind
	Turbulent Kinetic Energy	Second Order Upwind
	Turbulent Dissipation Rate	Second Order Upwind
	Warped-Face Gradient Correction	on
Solution Controls	Under-Relaxation Factors	Default values
Initialization	Hybrid Initialization	

Table 4 – *The thermodynamic parameters of water at given pressure of 1.32 bar*

Temperature [°C]	**Density [$\mathrm{kg \cdot m^{-3}}$]**	**Dynamic viscosity [Pa·s]**
20	998.22	0.0010015921
40	992.24	0.0006529814
50	988.06	0.0005468580

A total of 5000 iterations were performed. The convergence of the calculation was monitored from the trend of the residues and the trend of the inlet pressure. The residue target was to achieve all residues below 10^{-3}. The inlet pressure was monitored by the Mass-weighted average, and the target was to keep it constant, especially at the end of the calculations.

4.4 The CERCA analysis results

The following subchapters focus on the data obtained using CFD simulation. These are mainly the hydraulic characteristic of the fuel assembly at different operating temperatures and also the axial profile of the pressure drops and average velocities. The velocity values were subtracted using reports function called surface integrals, the specific type of report is the area-weighted averaged. For the pressure, the specific type of report is the mass-weighted average, for the mass flow, it is the fluxes function one.

4.4.1 The validation of calculations

To verify the accuracy of CFD simulation, the results shown in this subchapter are compared with the data received from the TA [45]. The comparison of the results is presented in the following Figure 30.

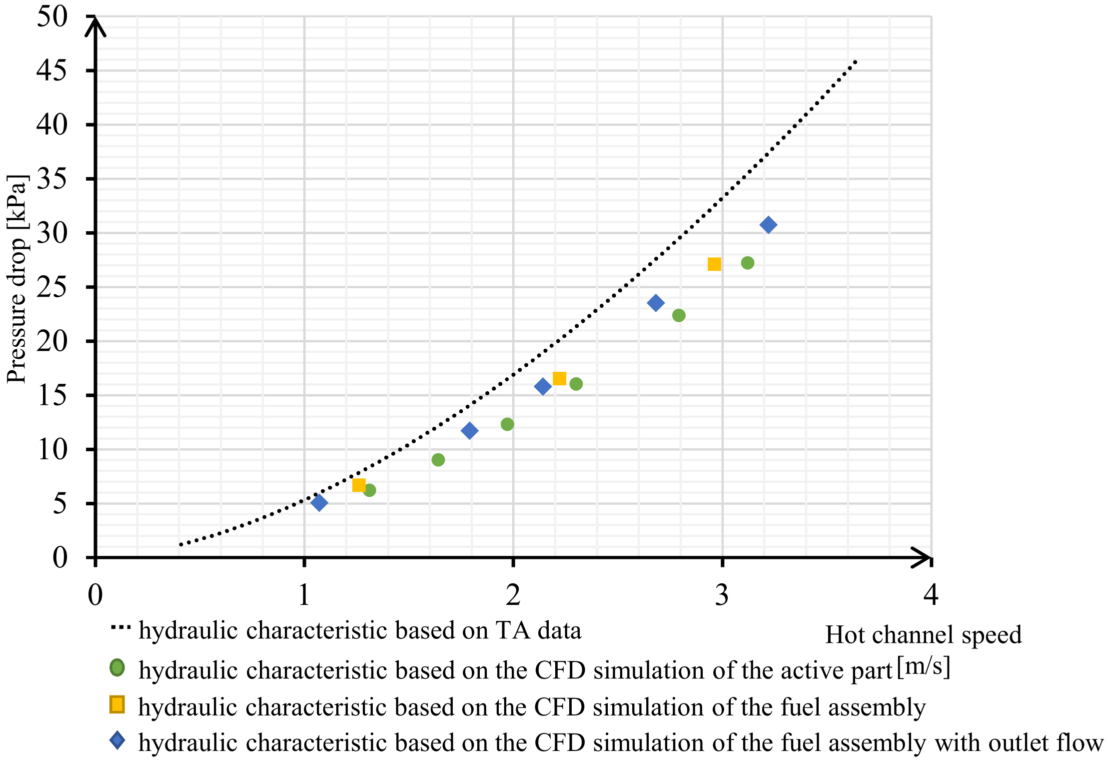

Figure 30 – *The speed dependence in hot channel on pressure drop of the CERCA FA*

Figure 30 shows the relationship between the velocity in the hot channel and the pressure drops through the fuel assembly. It is the hydraulic characteristic of the fuel assembly with water at given parameters of pressure of 1.32 bar and temperature of 40 °C. It includes a curve representing the results of the isothermal benchmark produced by the French TA. Besides, selected operating states, which were simulated using CFD on the models mentioned above, are presented in Figure 30.

As it can be seen in Figure 30, for the models containing the top and bottom nozzle parts, the obtained hydraulic characteristics of the relationship between the velocity in the hot channel and the pressure drop on the fuel assembly are not significantly different from the hydraulic characteristic of the active part. These results correspond to the expected pressure drop ratio between the active part and the top and bottom nozzle parts from the geometry point of view. The difference between the hydraulic characteristic from the received data and the hydraulic characteristic made by CFD simulation is up to 20%. Such a difference can be assumed due to the fact that the TA used the thermohydraulic system code instead of the CFD code. The data represented in Figure 30 are also shown in the following table 5 for the active part, table 6 for the whole fuel assembly and table 7 for the fuel assembly including outer flow. The data are ordered according to the velocity value at the input boundary condition of the simulated model.

Table 5 – *The hydraulic characteristic of the CERCA FA active part*

BC: Inlet velocity [$m \cdot s^{-1}$]	Pressure drop on the model [kPa]	Velocity in the hot channel [$m \cdot s^{-1}$]
1.9	27.23	3.12
1.7	22.40	2.79
1.4	16.05	2.30
1.2	12.33	1.97
1.0	9.05	1.64
0.8	6.23	1.31

Table 6 – *The hydraulic characteristic of the CERCA FA*

BC: Inlet velocity [$m \cdot s^{-1}$]	Pressure drop on the model [kPa]	Velocity in the hot channel [$m \cdot s^{-1}$]
2.0	27.11	2.96
1.5	16.57	2.22
0.85	6.71	1.26

Table 7 – *The hydraulic characteristic of the CERCA FA with the outer flow*

BC: Inlet velocity [m·s^{-1}]	Pressure drop on the model [kPa]	Velocity in the hot channel [m·s^{-1}]
1.8	30.75	3.22
1.5	23.55	2.68
1.2	15.81	2.14
1.0	11.73	1.79
0.6	5.07	1.07

4.4.2 The hydraulic characteristics

In addition to the calculations of the hydraulic characteristic at water temperature of 40 °C and operating pressure of 1.32 bar, other series of calculations on the fuel assembly model with the outer flow were performed to determine the characteristics at water temperature of 20 °C and 50 °C with the same operating pressure. The temperature value of 50 °C was chosen because of the possible occurrence in the active zone of the reactor LVR-15 during the summer months. The temperature value of 20 °C represents the hypothetical situation of the operating conditions and the possible experimental conditions. The results of these calculations are represented in the following Figure 31 and in Table 8.

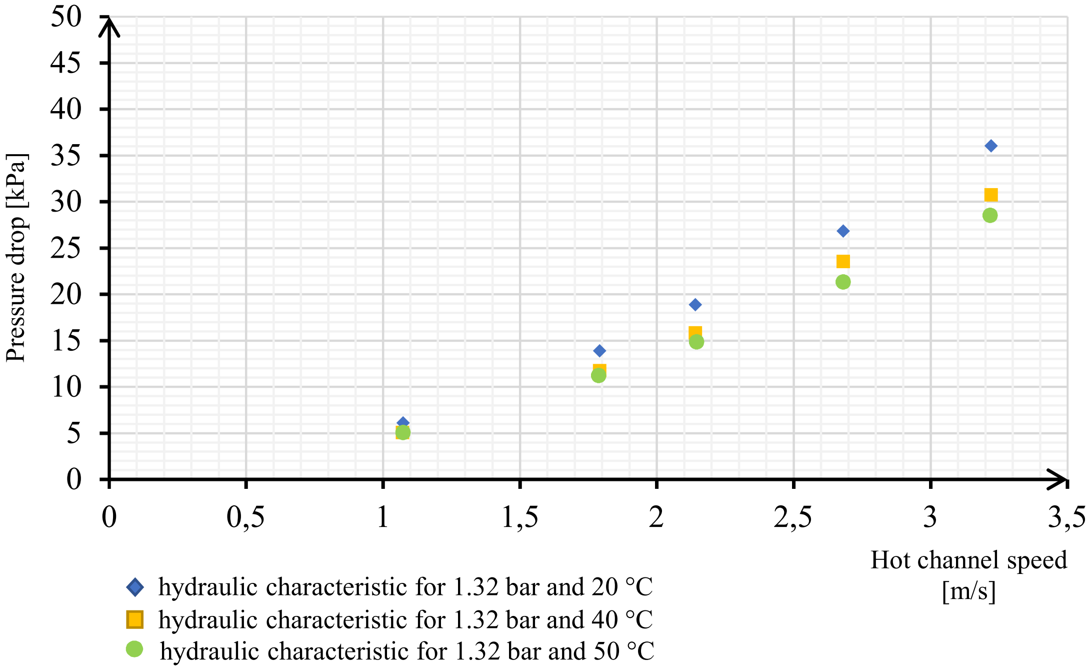

Figure 31 – *The speed dependence in hot channel on pressure drop of the CERCA FA at different temperatures and the operating pressure of 1.32 bar*

Table 8 – *The hydraulic characteristic of the CERCA FA with the outer flow at different temperatures and the operating pressure of 1.32 bar*

BC: Inlet velocity [m·s^{-1}]	**Water at 20 °C**		**Water at 40 °C**		**Water at 50 °C**	
	Pressure drop [kPa]	Velocity in channel [m·s^{-1}]	Pressure drop [kPa]	Velocity in channel [m·s^{-1}]	Pressure drop [kPa]	Velocity in channel [m·s^{-1}]
1.8	36.02	3.22	30.75	3.22	28.51	3.22
1.5	26.82	2.68	23.55	2.68	21.33	2.68
1.2	18.88	2.14	15.81	2.14	14.85	2.14
1.0	13.88	1.79	11.73	1.79	11.22	1.79
0.6	6.08	1.07	5.07	1.07	5.05	1.07

From the presented results, it is evident that, increasing the temperature, the hydraulic resistance decreases and so does the necessary pumping work to ensure the required flow. The trend of decreasing the hydraulic resistance of the fuel assembly due to the increasing temperature is mainly due to the decreasing trend of the dynamic viscosity as a function of the water temperature at given operating pressure.

4.4.3 The hydraulic axial profiles of the fuel assembly

One of the major results of this thesis is the evaluation of the axial profile of the pressure drops and of the average velocity in the fuel assembly. These values are further applied in the RELAP system code for the thermohydraulic analysis. An example of these profiles is presented in the following Figures 32 and 33. The results are reported numerically in Table 9.

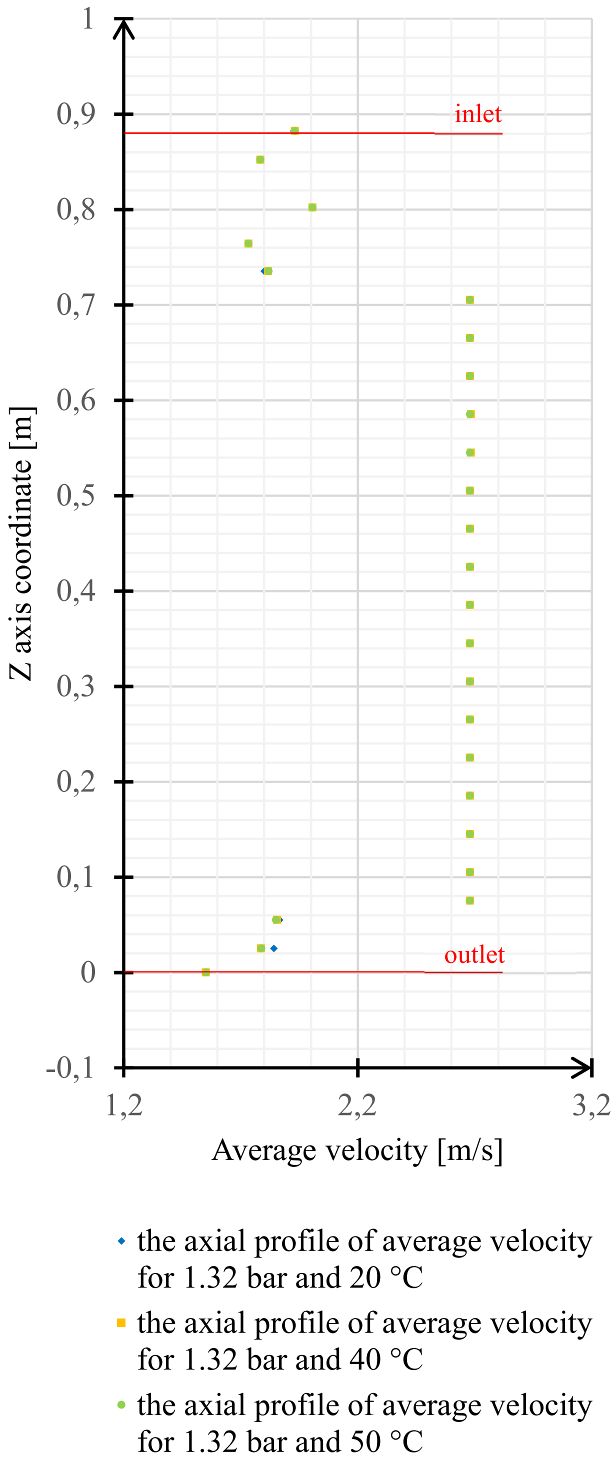

Figure 32 – *The average velocity axial profile of the CERCA FA*

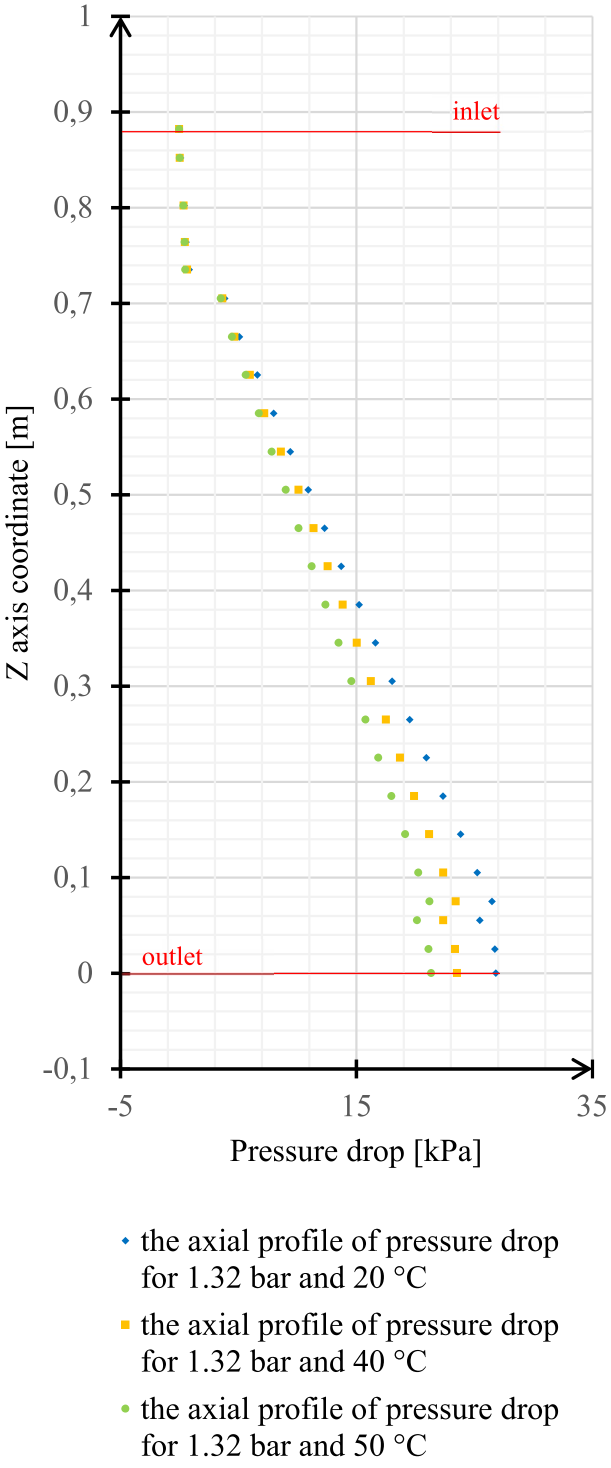

Figure 33 – *The pressure drop axial profile of the CERCA FA*

Table 9 – *The axial profile of the pressure drop and average velocity of the CERCA FA with the outer flow at different temperatures, operating pressure of 1.32 bar and the inlet velocity 1.5 $m.s^{-1}$ at the boundary condition*

z-axis coordinate [m]	**Water at 20 °C**		**Water at 40 °C**		**Water at 50 °C**	
	Pressure drop [kPa]	Average velocity [$m \cdot s^{-1}$]	Pressure drop [kPa]	Average velocity [$m \cdot s^{-1}$]	Pressure drop [kPa]	Average velocity [$m \cdot s^{-1}$]
0.882	0.00	1.92	0.00	1.93	0.00	1.93
0.852	0.10	1.78	0.05	1.78	0.03	1.78
0.802	0.42	2.01	0.38	2.01	0.35	2.01
0.764	0.55	1.73	0.48	1.73	0.45	1.73
0.735	0.83	1.80	0.66	1.82	0.51	1.82
0.705	3.83	2.68	3.66	2.68	3.51	2.68
0.665	5.09	2.68	4.69	2.68	4.46	2.68
0.625	6.59	2.68	5.98	2.68	5.64	2.68
0.585	8.00	2.68	7.21	2.68	6.74	2.68
0.545	9.40	2.68	8.60	2.68	7.84	2.68
0.505	10.91	2.68	10.11	2.68	9.02	2.68
0.465	12.32	2.68	11.39	2.68	10.12	2.68
0.425	13.72	2.68	12.58	2.68	11.22	2.68
0.385	15.23	2.68	13.86	2.68	12.39	2.68
0.345	16.63	2.68	15.05	2.68	13.49	2.68
0.305	18.03	2.68	16.24	2.68	14.59	2.68
0.265	19.53	2.68	17.52	2.68	15.77	2.68
0.225	20.93	2.68	18.71	2.68	16.87	2.68
0.185	22.33	2.68	19.9	2.68	17.96	2.68
0.145	23.84	2.68	21.18	2.68	19.14	2.68
0.105	25.24	2.68	22.37	2.68	20.24	2.68
0.075	26.48	2.68	23.43	2.68	21.21	2.68
0.055	25.46	1.87	22.37	1.86	20.14	1.85
0.025	26.74	1.84	23.37	1.79	21.14	1.79
0	26.82	1.55	23.55	1.55	21.33	1.55

These are corresponding to the mass flow through the fuel assembly of approximately 7.7 kg·s^{-1}; specifically, they are axial profiles from the CFD model of the fuel assembly with the outer flow. The results are represented for water parameters at pressure of 1.32 bar and for three different temperature values. The linear region in both Figures corresponds to the active part of the fuel assembly. The input area of the fuel assembly is located at the z coordinate 0.88 m; the output area is situated at the z coordinate 0 m. The greatest effect in the values of the pressure drop is on the different temperatures visible in the active part of the fuel assembly. This phenomenon can be attributed to the hydraulic diameter of the active part area that is smaller than the one of the top and bottom nozzles; due to the higher occurrence of walls per unit flow volume, the frictional resistance and different dynamic viscosity of water are more pronounced here. It can be assumed that for other mass flows, the shape may be very similar for both profiles. The only expected difference is the shift of the given profile to higher or lower values, both in pressures and velocities.

4.4.4 The analysis of the flow inside the CERCA FA

The following subchapter is focused on the character of the flow inside the CERCA FA. For this purpose, the velocity contours and the particle tracking were used. The analysis is performed on the CERCA FA model that included the top and bottom nozzle parts and the outer flow. For the sake of comparison with the IRT-4M, the data with the inlet velocity 1.2 m·s^{-1} were used.

Figure 34 includes the geometry of the CERCA FA, the velocity contours on the symmetry surfaces of the ¼ FA and the velocity contours of the horizontal cross-sections. The velocity contours are mainly focused on the area of the top and bottom nozzle parts. The coordinate system fixes the correct position of the ¼ FA. The blue rectangles show the areas where the flow character is documented using the particle tracking. For more information, the selected cross-sections are further documented in Figures 35 – 42 with graphs of the velocity magnitude and the static pressure along the specific lines. The cross-sections are focused on the area of top nozzle at z-coordinate 0.81 m, the active part area at z-coordinate 0.48 m and the bottom nozzle area at z-coordinate 0.05 m.

The results of the particle tracking are represented in the following Figures 43, 44, 45, 46, and 47. Some of these particles are so-called delayed, meaning that these specific particles were filtered in the limited time frame. The color legend for the velocity is included. The detailed description is provided under pictures of the relevant section.

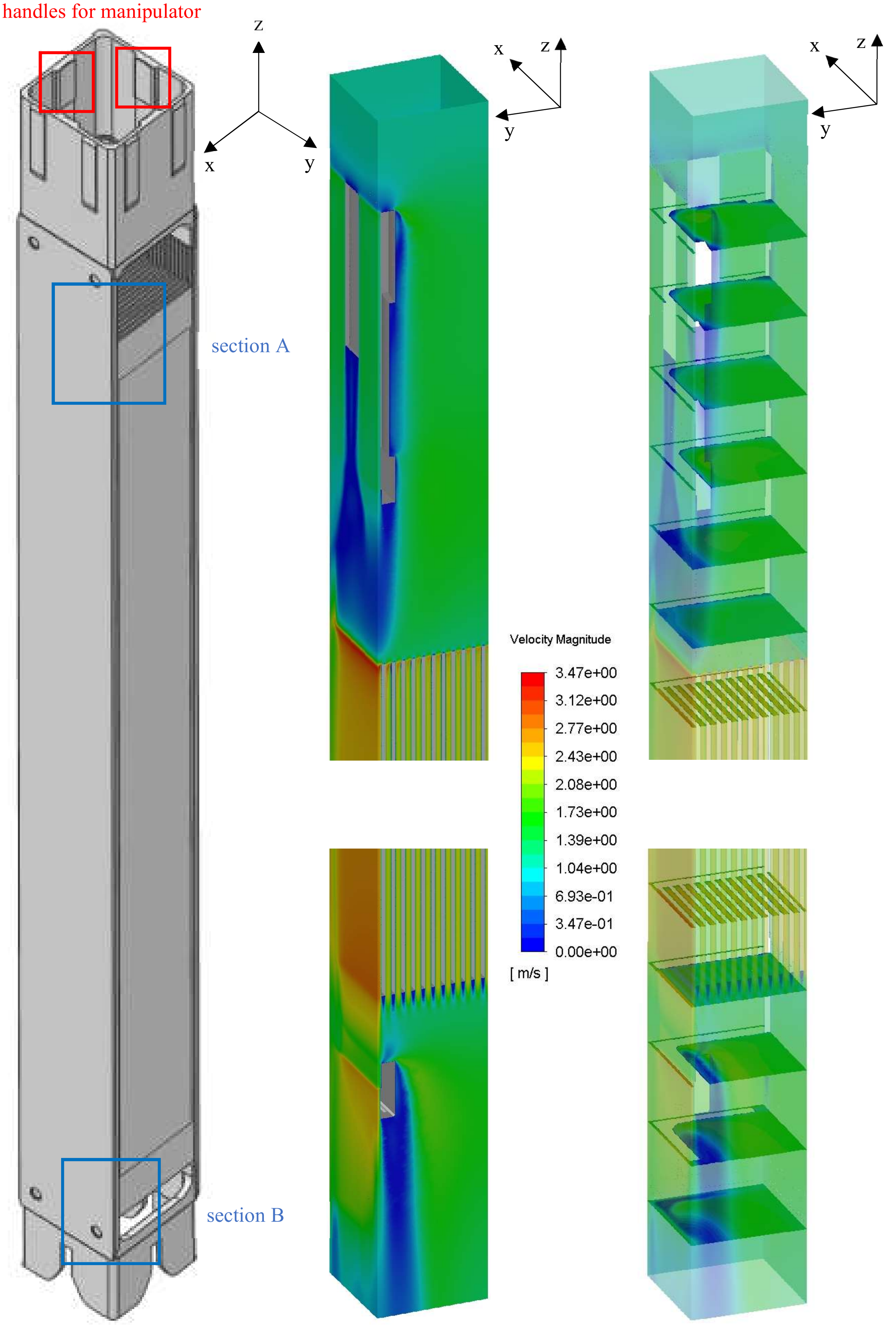

Figure 34 – *The velocity contours of the ¼ CERCA FA*

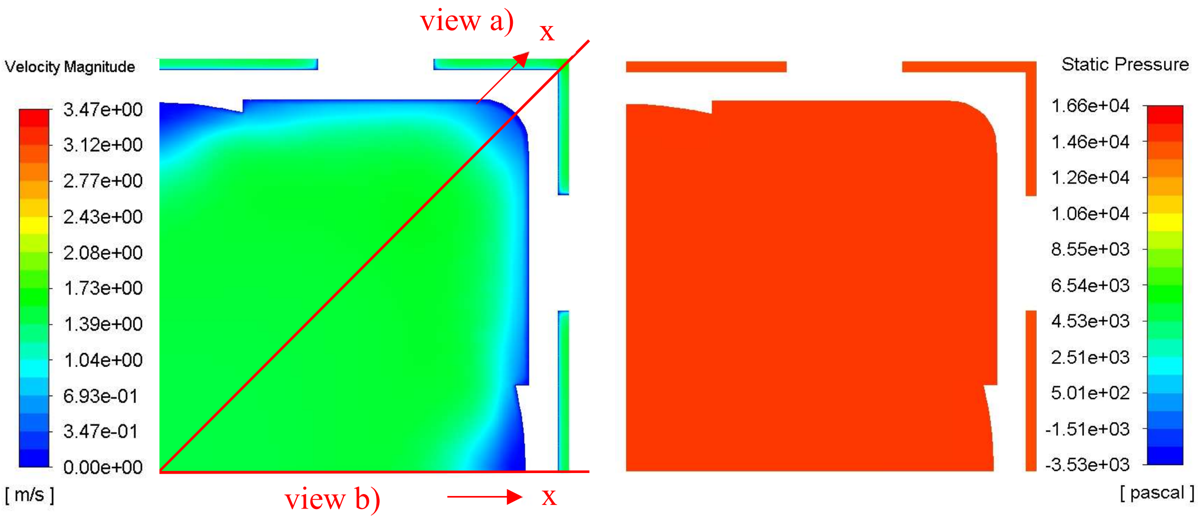

Figure 35 – *The detailed cross-section at z = 0.81 m of the ¼ CERCA FA, top nozzle*

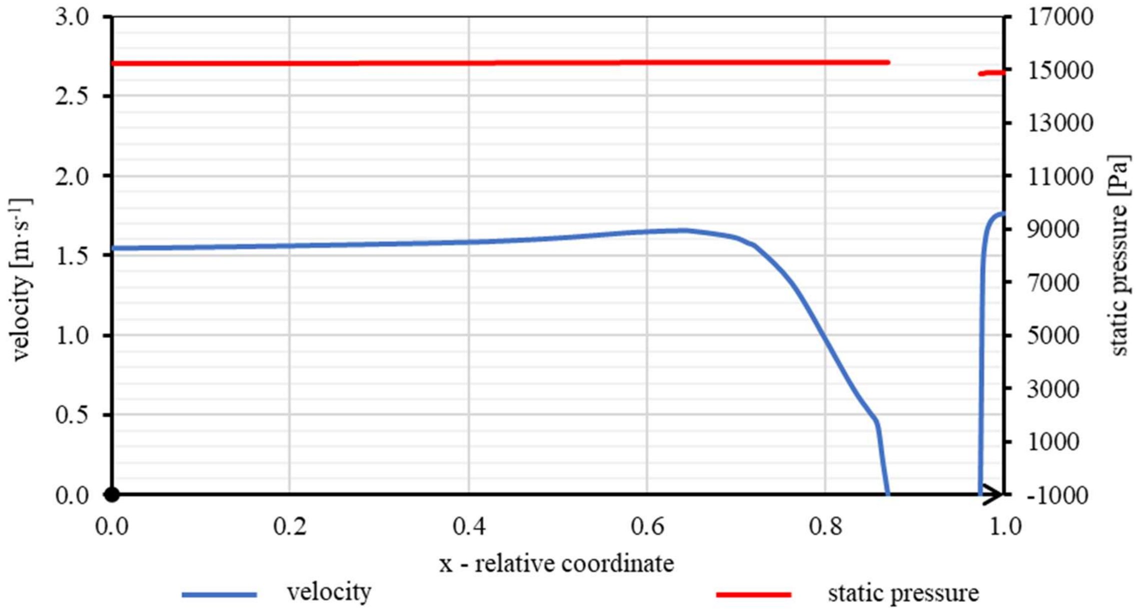

Figure 36 – *The velocity magnitude and the static pressure at z = 0.81 m, view a)*

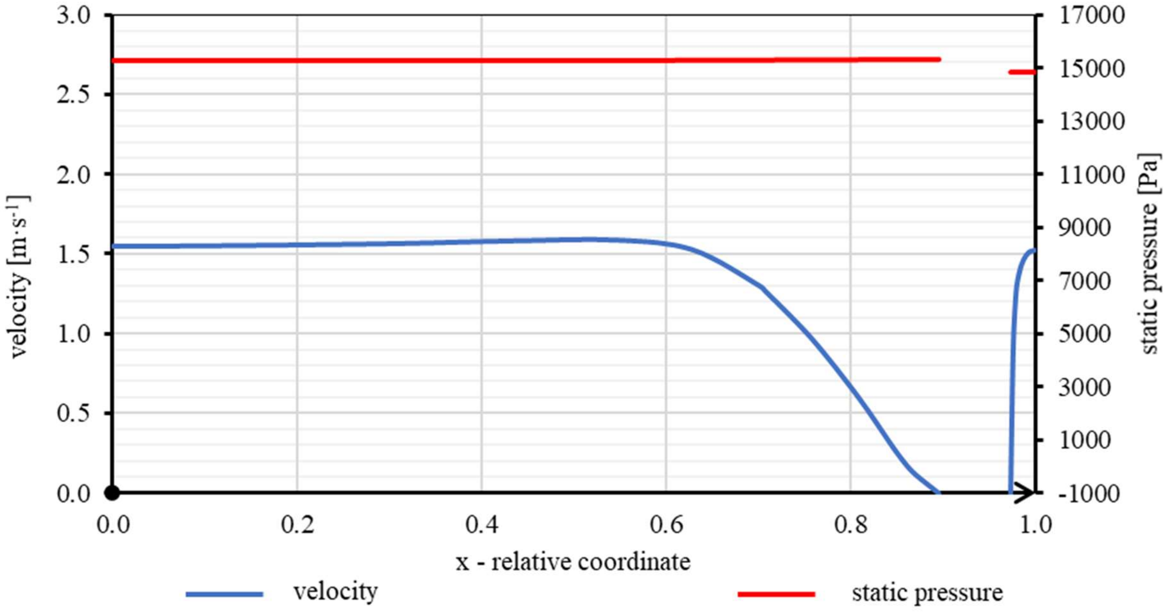

Figure 37 – *The velocity magnitude and the static pressure at z = 0.81 m, view b)*

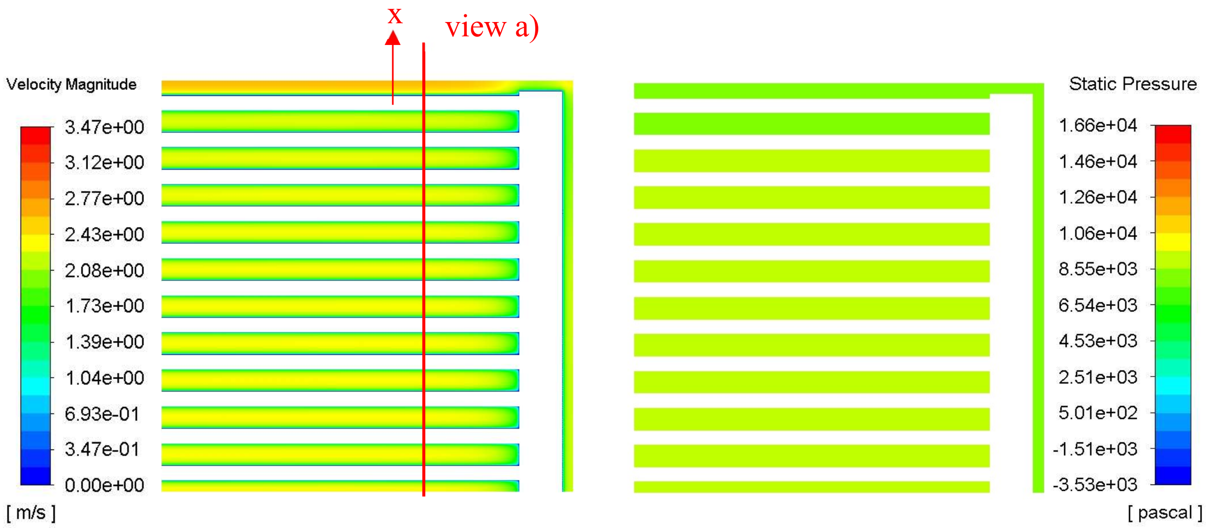

Figure 38 – *The detailed cross-section at z = 0.48 m of the ¼ CERCA FA, active part*

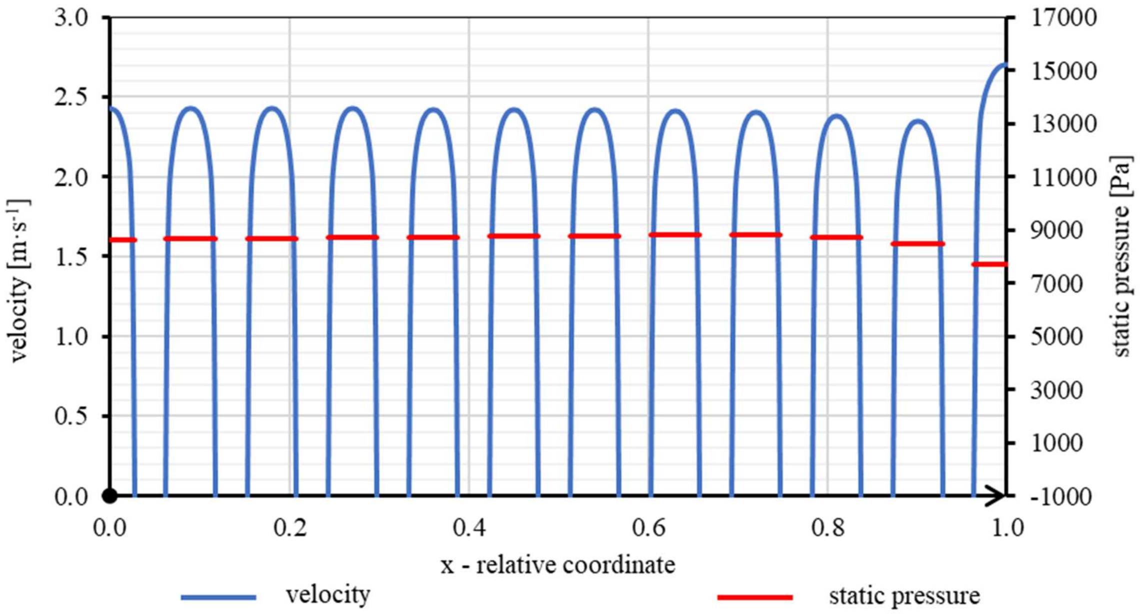

Figure 39 – *The velocity magnitude and the static pressure at z = 0.48 m, view a)*

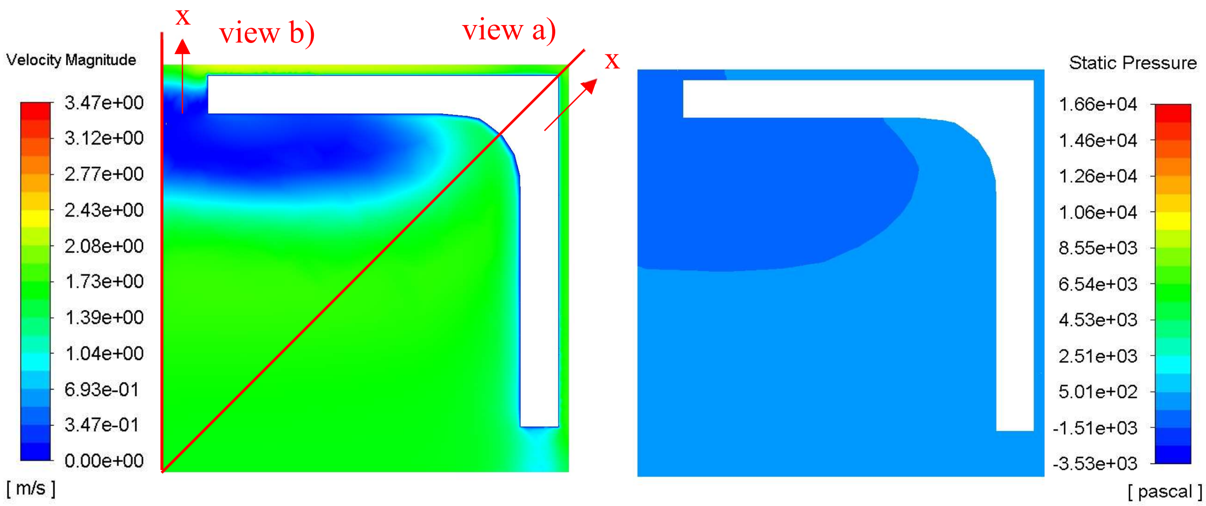

Figure 40 – *The detailed cross-section at z = 0.05 m of the ¼ CERCA FA, bottom nozzle*

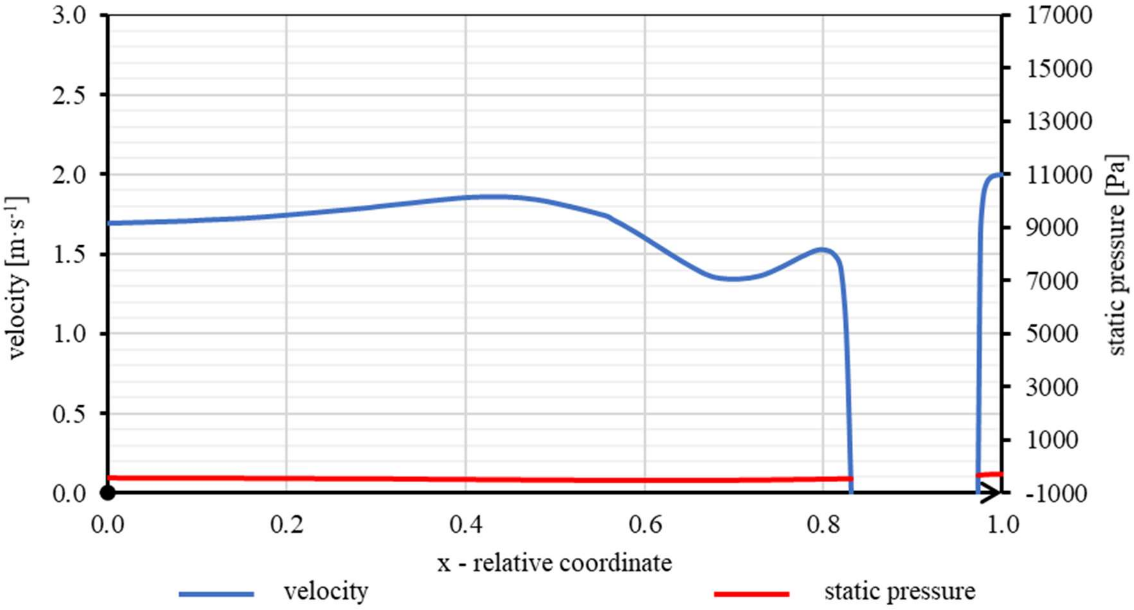

Figure 41 – *The velocity magnitude and the static pressure at z = 0.05 m, view a)*

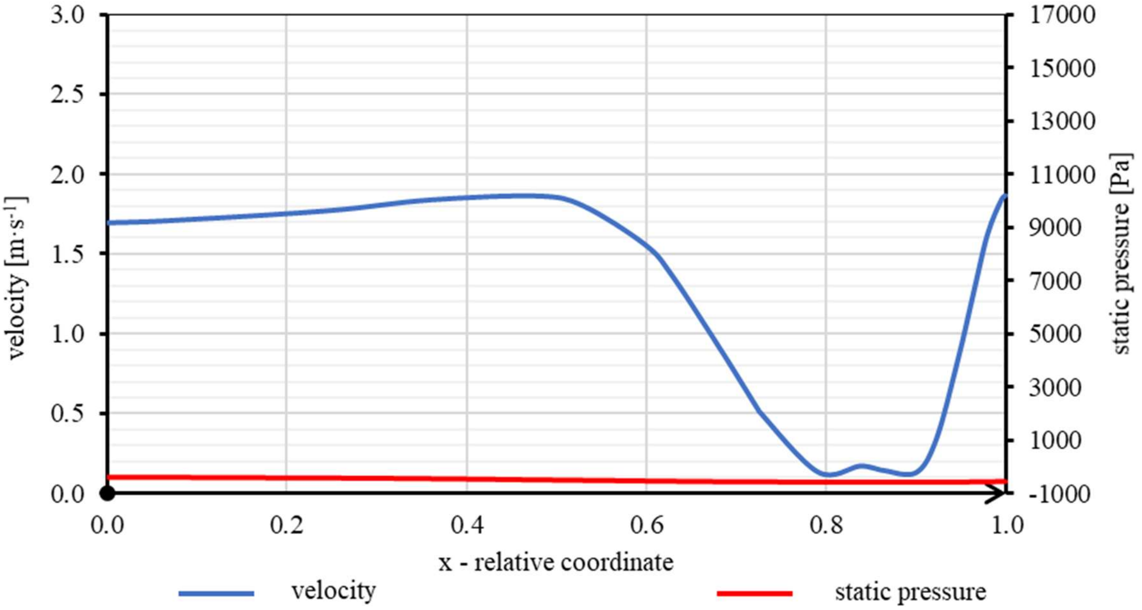

Figure 42 – *The velocity magnitude and the static pressure at z = 0.05 m, view b)*

The velocity contours capture significantly low velocity magnitude in and under the windows areas of the top and bottom nozzle parts. Since the velocity magnitude is defined as a sum of velocities in all three directions; this phenomenon may be caused by turbulence behavior of the flowing water. On the inlet and outlet of the active zone channels, there are turbulent flows due to the geometry. The velocity in the outer channel is higher compared to the rest of the channels.

Figures 36, 37 and 41, 42 show more in details the spatial velocity distribution in the nozzle areas. For the top nozzle area, the flow is affected by the handles for the manipulator. The position of these attachments is marked in Figure 34. In the area of the bottom nozzle, the low-velocity magnitude occurs due to the turbulences. These high turbulences are further documented in Figures 46 and 47. The cross-section of the active part, which is documented in Figures 38 and 39, captures the flow distribution trend between the singles active zone channels. Especially from Figure 39, it is possible to see that the outer channel reaches around 0.25 $m \cdot s^{-1}$ higher velocity compared to the other channels.

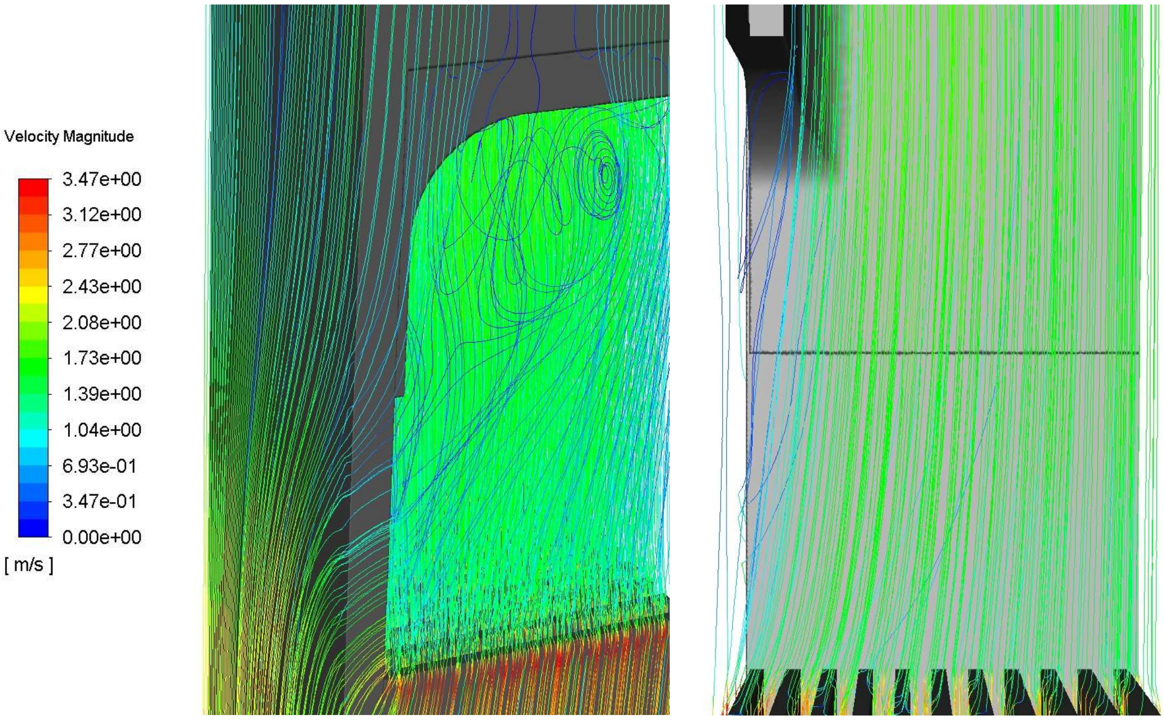

Figure 43 – *The particle tracking in the area of section A – CERCA FA*

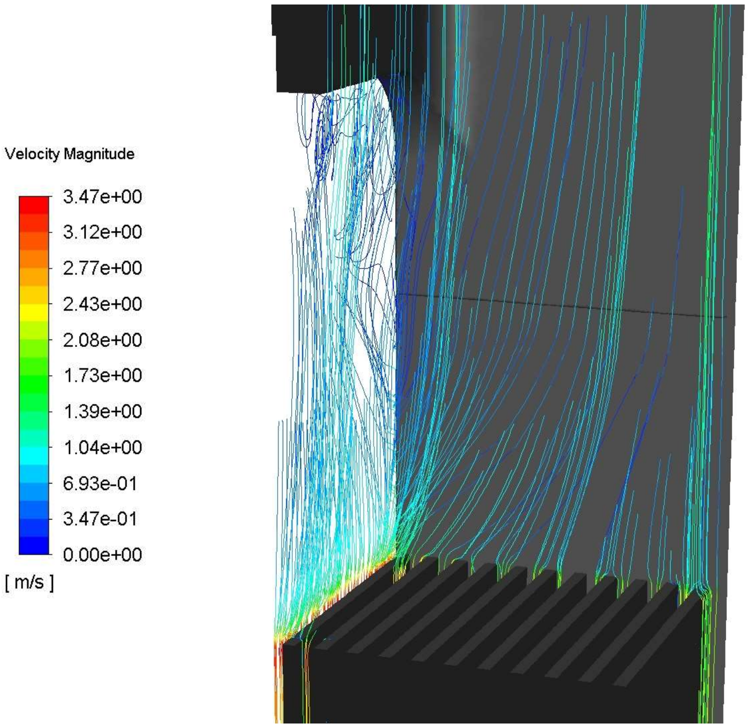

Figure 44 – *The particle tracking in the area of section A – delayed particles – CERCA FA*

As mentioned in the introduction to the subchapter, Figures 43 and 44 represent the particle tracking in the area of section A, in other words, the window area in the top nozzle part. Figures show the transition of a part of the flow from the inner area of the fuel assembly to the outer one. Specifically, Figure 44 shows the delayed particles: a certain part of these delayed particles is due to the wall friction. The rest of them are located in the window area and they are caused by high turbulences.

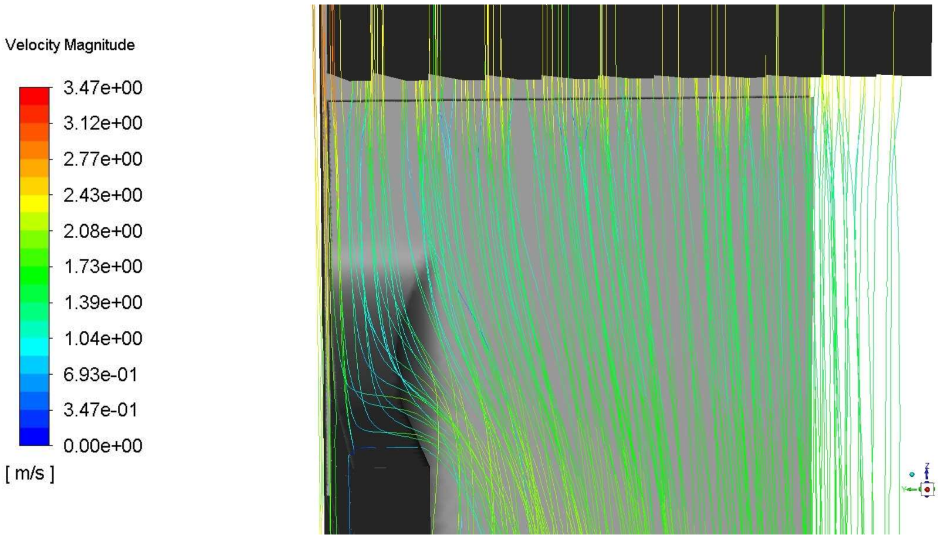

Figure 45 – *The particle tracking in the area of section B – the window area – CERCA FA*

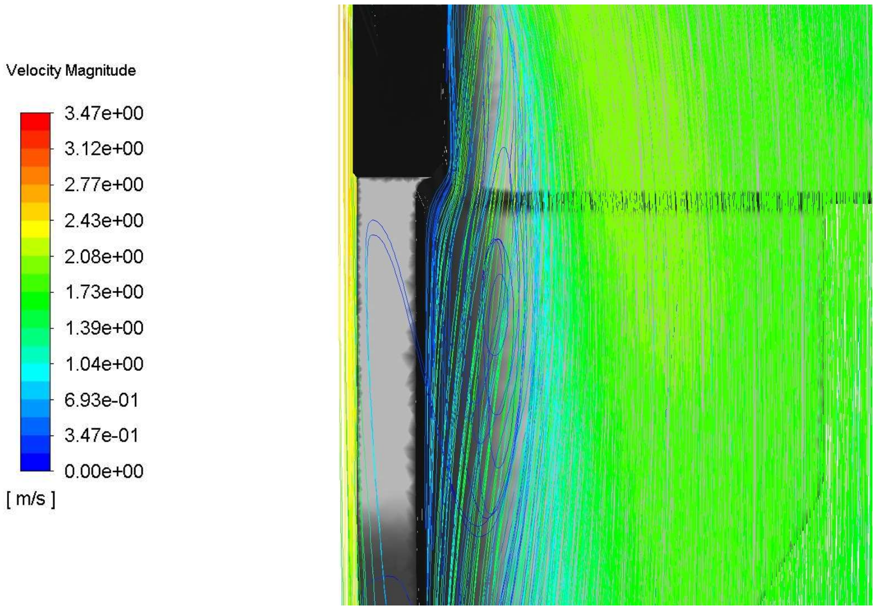

Figure 46 – *The particle tracking in the area of section B – under the window – CERCA FA*

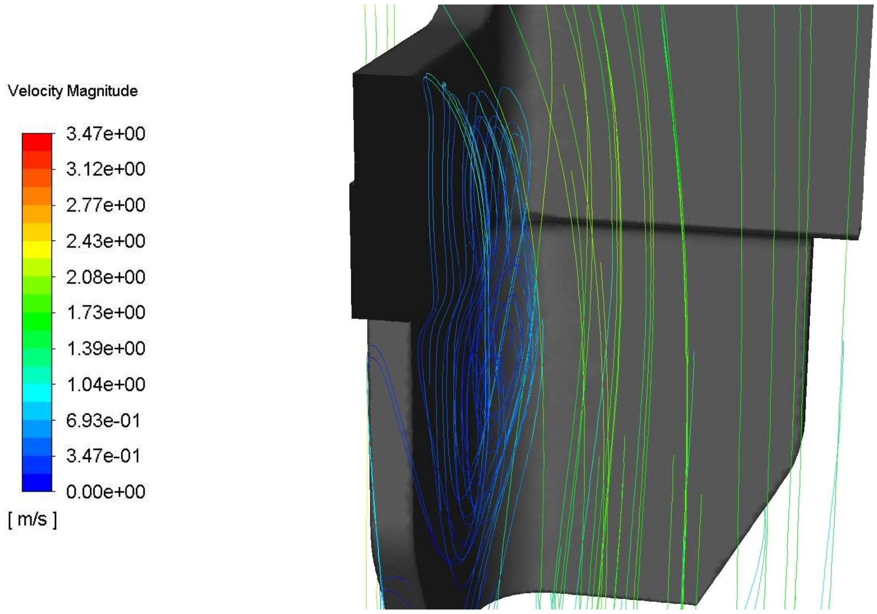

Figure 47 – *The particle tracking in the area of section B – delayed particles – CERCA FA*

Figures of the section B capture the turbulent flow occurring in the bottom nozzle part. In Figure 45, the partial passage of the flow from the outer bypass to the inner volume of the fuel assembly through the window in the bottom nozzle part is visible. Figures 46 and 47 document the situation under this window, where the high turbulent flow occurs. The delayed particles again represent a certain number of particles hold due to the turbulence.

Chapter 5: The Thermohydraulic Analysis of the IRT-4M Fuel Assembly

The chapter is focused on the thermohydraulic analysis of the Russian design IRT-4M fuel assembly using the CFD code ANSYS Fluent. As in the previous chapter, the creation and simplification of geometry, the creation of the mesh and the obtained results are described first. Then the calculations were divided into two model examples, the first one representing only the geometry of the active part of the fuel assembly and the second one representing the entire IRT-4M fuel assembly with the top and bottom nozzle parts and the external flow around the assembly. The results of the analyzes are further compared with the results of the analysis carried out on the New European fuel assembly presented in the previous chapter. All the computing work was done on the DELL Precision Tower 3620 workstation, featuring a single 4-core Intel Core i7-7700 processor with a base frequency of 3.6 GHz and 64 GB of RAM.

5.1 The creation of geometry

Since it was not possible to use a 3D model of the IRT-4M supplied directly by the producer in this diploma thesis, it was necessary to model the geometry using publicly available fuel assembly drawings, the dimensions of the physical model of the fuel assembly, which is owned by the CVR, and the 3D model of the 6-tube version of the IRT-4M fuel assembly created in the Department of Design in the CVR. The resulting model consists of 7 fuel tubes of square cross-section with rounded edges, one fuel tube of circular cross-section and one non-fuel tube of circular cross-section which serves as a central throttle element. The model also includes top and bottom nozzle parts which hold the tubes in their proper positions. All these components are made of aluminum alloy; the fuel is stored in the tubes in the form of a uranium oxide dispersion in an aluminum matrix (the so-called meat). The software used for this purpose is called SpaceClaim, and it is included in ANSYS software pack. The resulting geometry is represented in the following Figure 48.

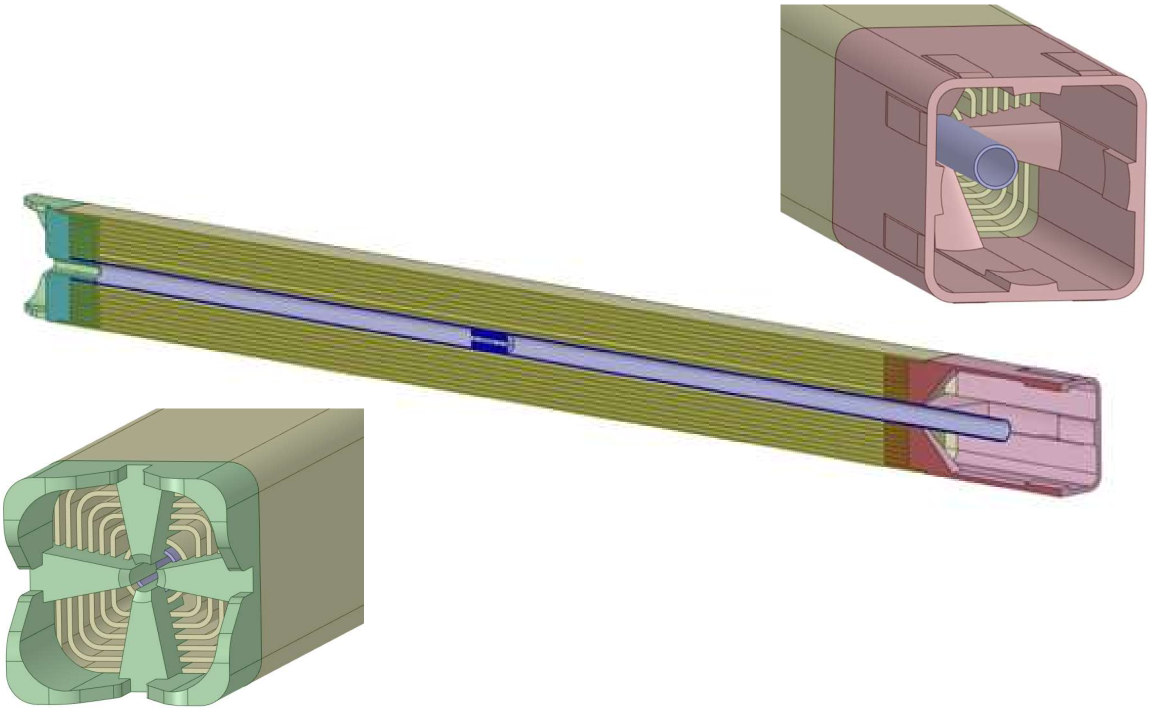

Figure 48 – *The created geometry of the IRT-4M 8-tube version*

Like the New European fuel assembly, also the IRT-4M has a symmetrical character; for this reason, only one quarter of the fuel assembly is simulated using the symmetric boundary condition. The next procedure was similar to the previous chapter: using the model an inverse volume representing the mass of the water was created; this volume was further divided into several sub-volumes so that a structured mesh of the required parameters could create the active part of the fuel assembly.

5.2 The IRT-4M mesh parameters

In this model, two types of mesh elements are used as well as in the CERCA fuel assembly. Specifically, they are the hexahedral and polyhedral elements, and the regions of these elements are connected by a non-conformal interface by transition elements. The mesh sensitivity analysis was performed on the one-quarter of the specific channel of the fuel assembly using the symmetry boundary condition; the geometry of this channel is represented in the following Figure 49. The physical parameters, the turbulent model and the input velocity were corresponding to the analysis made on the CERCA New European fuel assembly. The analysis was again focused primarily on the reduction of elements in the longitudinal direction of the channels. Unlike the previous fuel assembly, there was a problematic area of the throttling element occurrence in the center of the active part of the fuel assembly where it was necessary to provide a sufficiently fine mesh. This area is documented in the following Figure 53. The results of the analyzes are represented in the following Figures 50, 51 and 52. For the clarity of the analyzed directions, Figure 49 is attached. Of the represented values, 5 elements were selected in the y-direction, 68 elements in the x-direction and 510 elements in the z-direction.

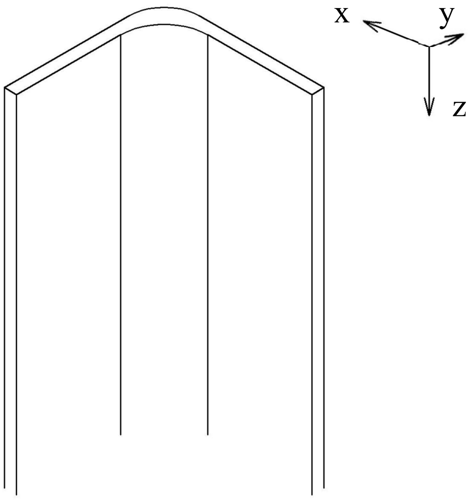

Figure 49 – *The simulated geometry for the IRT-4M model sensitivity analysis*

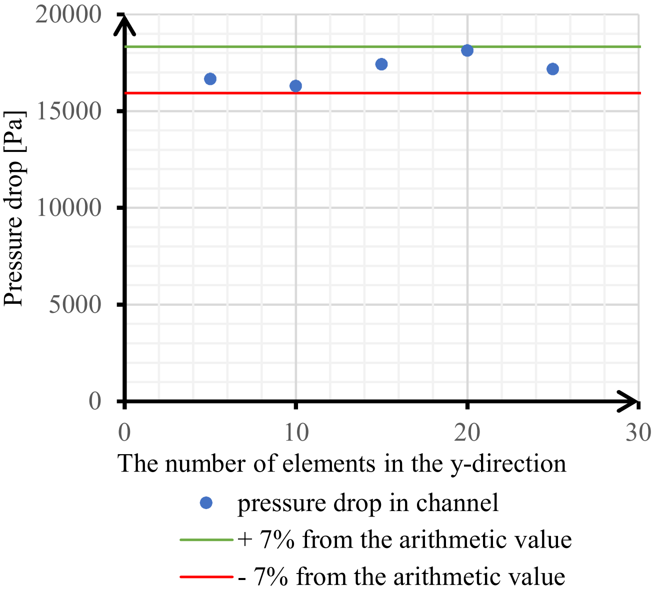

Figure 50 – *The mesh sensitivity analysis in the y-direction for the IRT-4M FA*

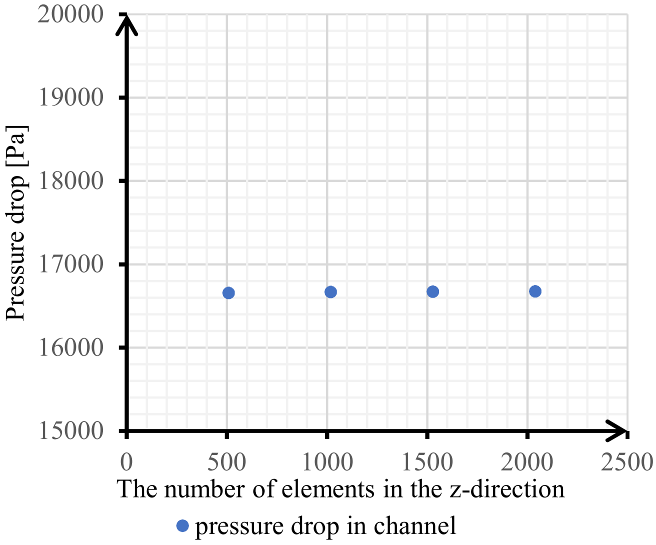

Figure 51 – *The mesh sensitivity analysis in the z-direction for the IRT-4M FA*

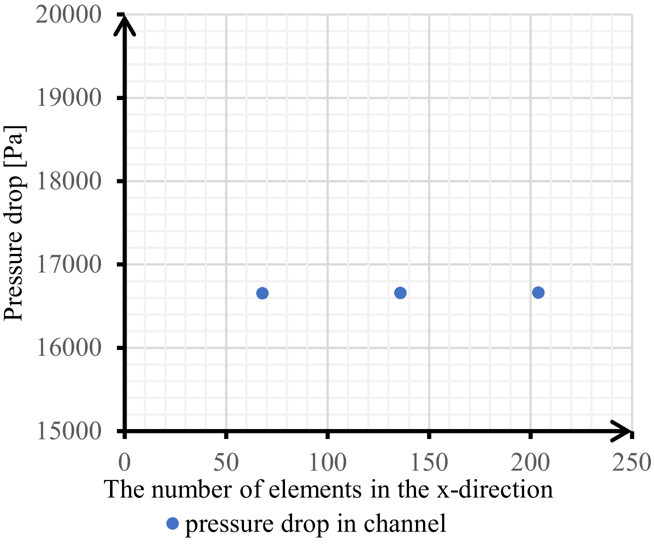

Figure 52 – *The mesh sensitivity analysis in the x-direction for the IRT-4M FA*

The computational mesh, which was created for the simulations of the active part of the fuel assembly IRT-4M, is presented in the following Figure 53. It is a purely hexahedral structured mesh that captures only one-quarter of given geometry with the subsequent use of symmetry boundary condition.

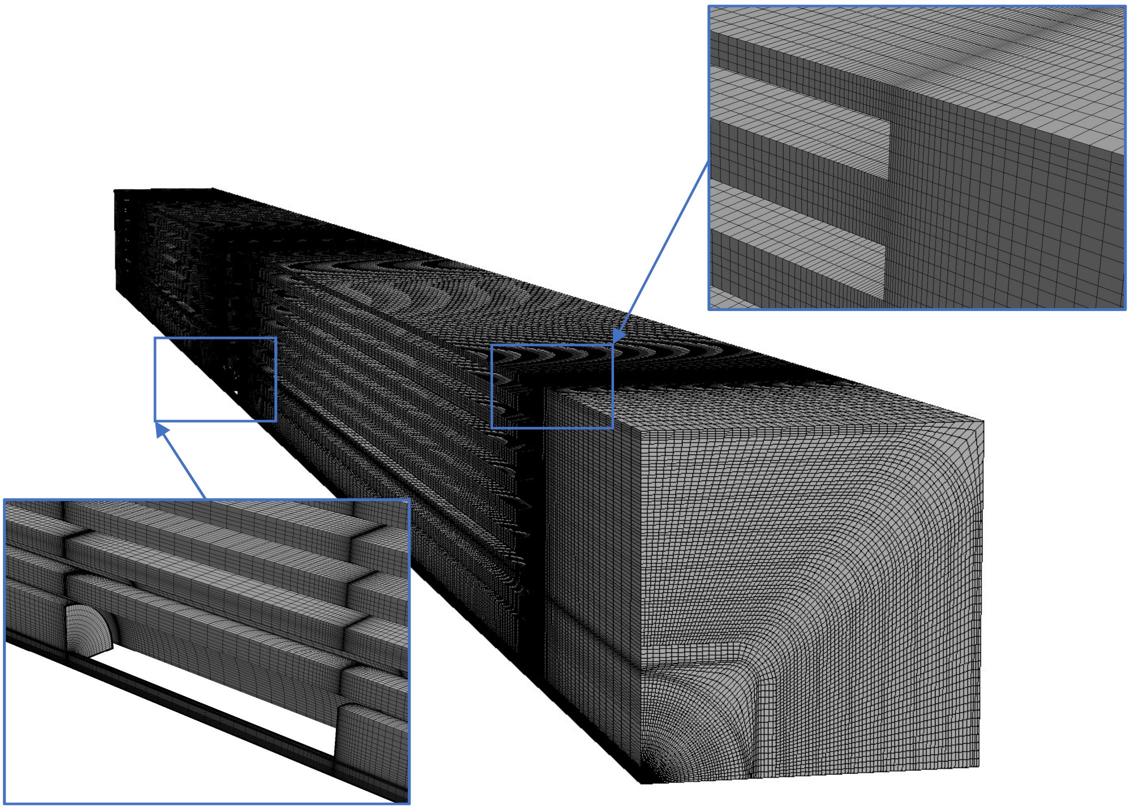

Figure 53 – *The 3D structured mesh of the first level of accuracy, the model of the active part of the IRT-4M FA*

As in the previous chapter, the quality of this mesh is assessed according to the orthogonal quality and the aspect ratio. The achieved orthogonal quality and aspect ratio values are shown in the following Figures 54 and 55. The mesh contains a total of 3 364 800 hexahedral elements.

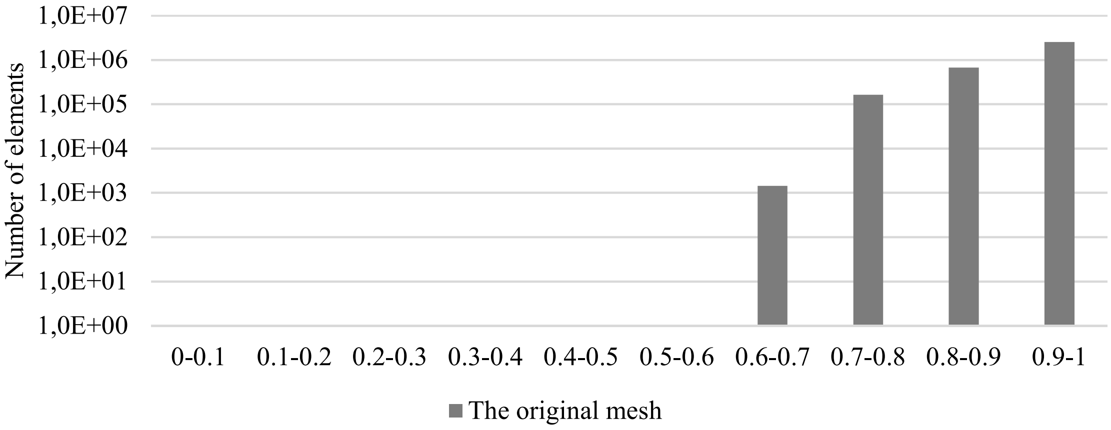

Figure 54 – *The achieved orthogonal quality of the mesh of the channels of the active part of the IRT-M4 fuel assembly*

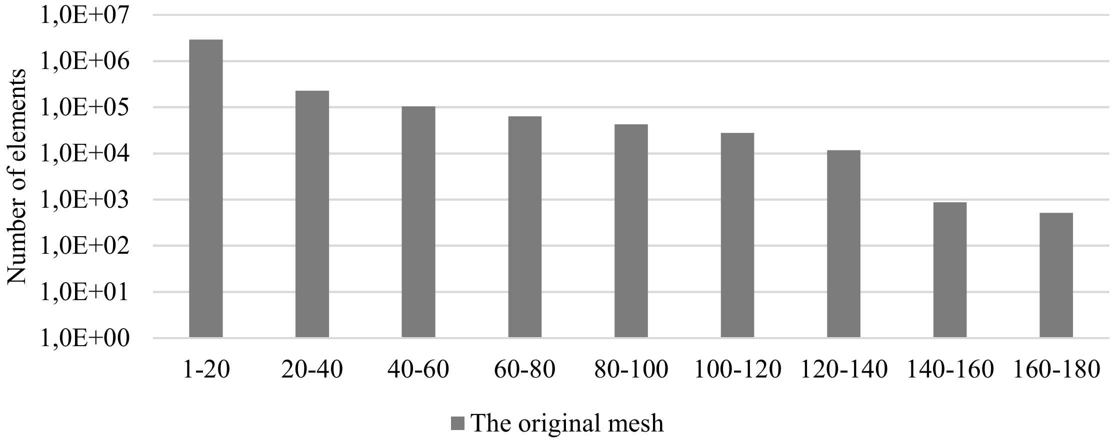

Figure 55 – *The achieved aspect ratio values of the mesh of the IRT-4M FA active part channels*

The mesh for the model of IRT-4M fuel assembly with outer flow is documented below in Figure 56. This mesh was made on the same principle as the meshes for the CERCA FA with the outer flow.

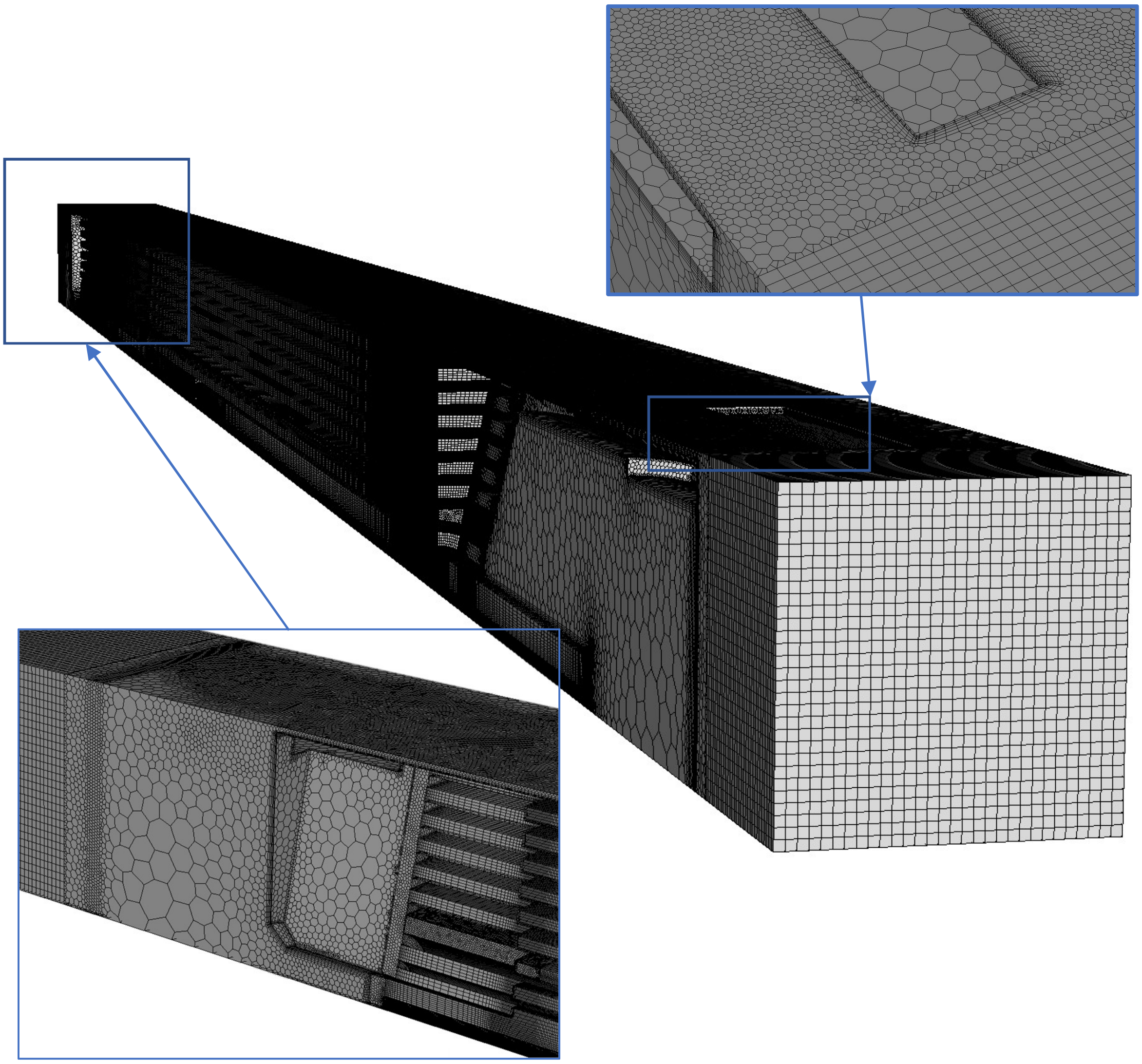

Figure 56 – *The 3D mesh of the whole IRT-4M fuel assembly with outer flow*

Hexahedral elements are used for the active part of the fuel assembly in structured order with the same parameters as in the previous case. Polyhedral and prismatic elements are used for the volumes of the top and bottom nozzle parts. The connection between hexahedral and polyhedral elements is made as a non-conformal interface; this interface was tested, and it has no negative impact. The test was performed as the simulations of the original tetrahedral model and the model formed using polyhedral elements with the same physical parameters and boundary condition. The monitored parameters were the pressure drop, mass flow and velocities at defined points. The results of the mesh quality analysis are shown in Figure 57 for the orthogonal quality and Figure 58 for the aspect ratio. The original mesh is composed of 5 691 371 elements; the transformed one has 4 311 224 elements.

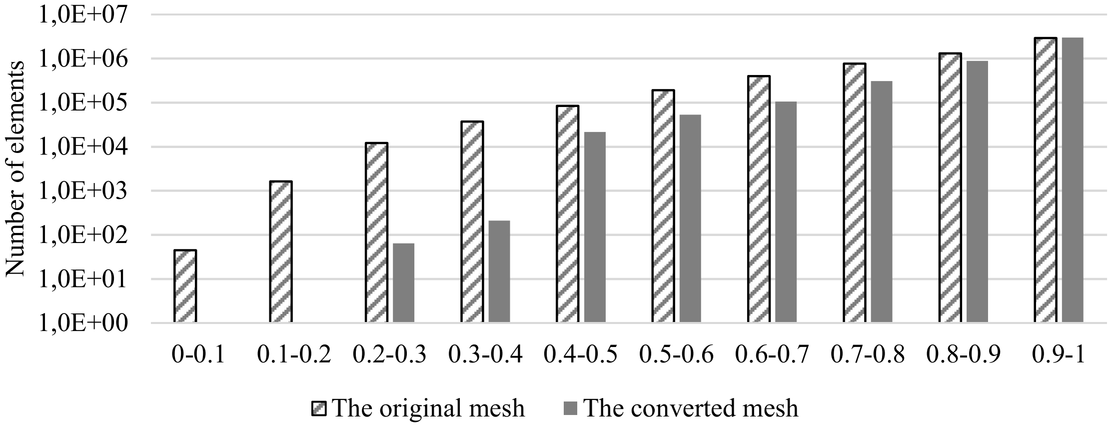

Figure 57 – *The achieved orthogonal quality of the mesh of the whole IRT-4M FA with outer flow*

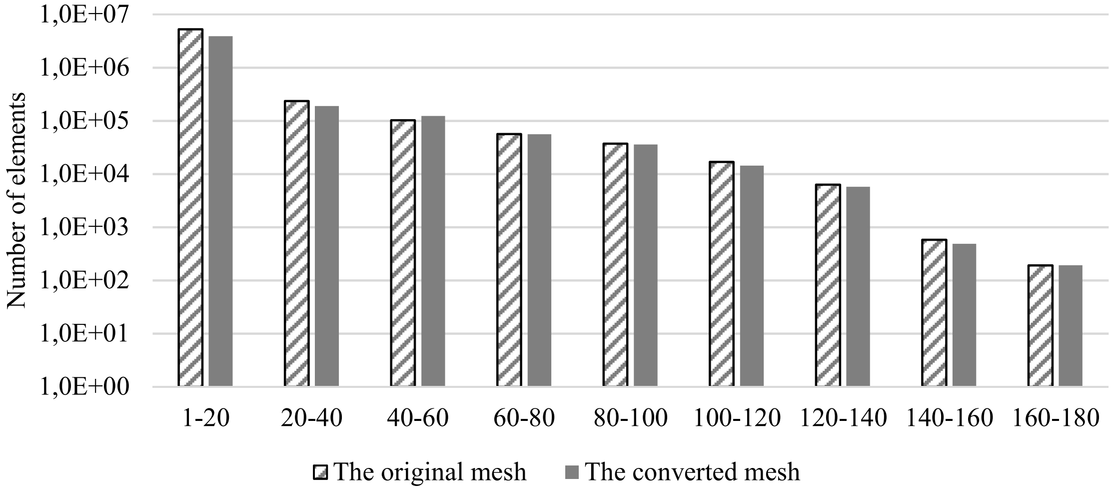

Figure 58– *The achieved aspect ratio of the mesh of the whole IRT-4M FA with outer flow*

The high aspect ratio values for both models are due to the creation of a structured mesh. The elements with these values are situated in the area of central tube and they have no negative impact on model accuracy.

5.3 The IRT-4M solver setting

As this is a physically and geometrically similar case to the one in the previous chapter, the same solver and its setting as for the New European fuel assembly were used for all the simulated models of the IRT-4M fuel assembly. A detailed description of this setting can be found in chapter 4.3 *The solver setting* or in the Table 3 – *Summary of the ANSYS Fluent solver settings*. The only difference is that these calculations were performed only for physical parameters of water corresponding to the temperature of 40 °C and the pressure of 1.32 bar, specific values can be found in Table 2 – *The thermodynamic parameters of water at given pressure of 1.32 bar*. At the same time, the number of iterations for each case and the same convergence criteria were used here.

5.4 The IRT-4M analysis results

Unlike for the CERCA FA, there are no available data for the validation of calculations for this fuel assembly. However, the mesh sensitivity analysis was made, and the same procedure with the same solver setting as for the CERCA FA was used in this case; based on this, the following results are considered sufficient. The results represented in this chapter are focused on the comparison of the hydraulic characteristic of the IRT-4M FA and the CERCA FA. Specifically, it is a comparison between the hydraulic characteristic of the active part of both fuel assemblies, a comparison of the hydraulic characteristic between the active part of the IRT-4M FA and the whole geometry of IRT-4M FA, and a comparison between the hydraulic characteristic of the IRT-4M FA and the CERCA FA. These results are valid for the operating pressure of 1.32 bar and temperature of 40 °C.

5.4.1 The comparison of the active parts of IRT-4M FA and CERCA FA

From the geometric point of view, it is possible to say, that the active part of the CERCA FA has lower hydraulic diameter than the active part of the IRT-4M FA. Both active parts have the same length 660 mm. Based on this, higher values of pressure drop for the active part of CERCA FA can be expected in comparison to the active part of the IRT-4M FA. The results of the CFD analysis for the active parts of both fuel assemblies are represented on the following Figure 59.

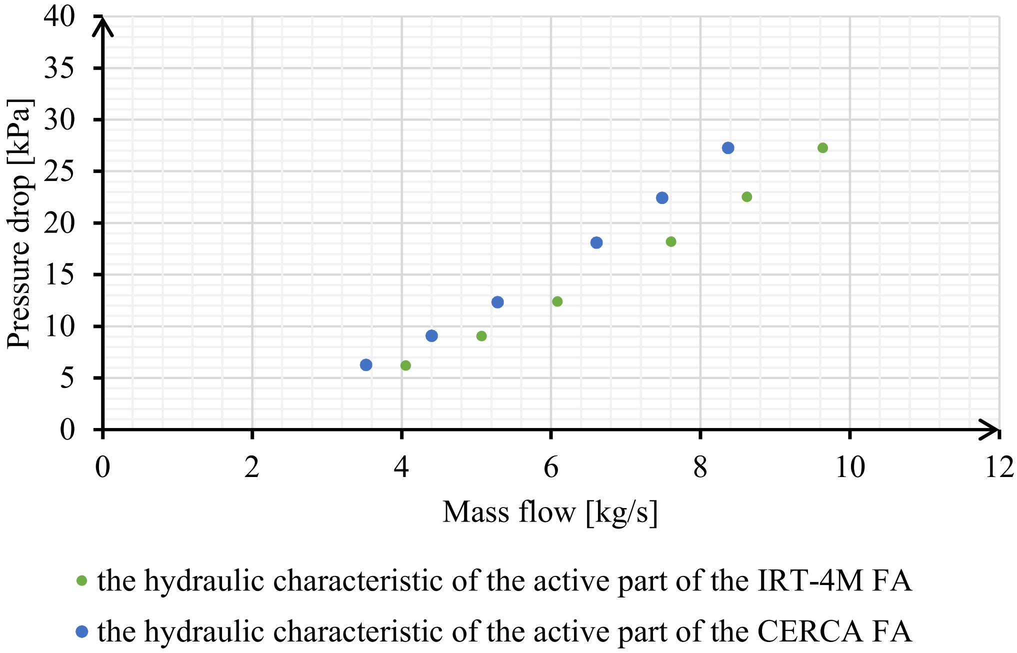

Figure 59 – *The pressure drop dependence on mass flow of the both active parts*

As it can be seen in Figure 59, the trend of the hydraulic characteristics and their mutual position corresponds to the expectation given by the respective hydraulic diameters. The hydraulic characteristic of the active part of the CERCA FA shows a higher pressure drop values, average 15 % in comparison to the active part of the IRT-4M FA. This trend also indicates that the CFD analysis of the active part the IRT-4 M FA is giving reasonable values of the pressure drop, considering that the validation of the CERCA fuel assembly in the previous chapter is sufficient. The values are listed in the following table 10; the data are ordered according to the inlet boundary condition.

Table 10 – *The hydraulic characteristic of the active parts the fuel IRT-4M and CERCA FA at the water temperature of 40 °C and operating pressure of 1.32 bar*

BC: Inlet velocity [$\text{m}\cdot\text{s}^{-1}$]	**the CERCA FA**		**the IRT-4M FA**	
	Pressure drop [kPa]	Mass flow [$\text{kg}\cdot\text{s}^{-1}$]	Pressure drop [kPa]	Mass flow [$\text{kg}\cdot\text{s}^{-1}$]
1.9	27.23	8.37	27.24	9.64
1.7	22.40	7.49	22.52	8.62
1.5	18.08	6.61	18.16	7.61
1.2	12.33	5.29	12.37	6.09
1.0	9.05	4.41	9.04	5.07
0.8	6.23	3.52	6.17	4.06

The difference between the resulting mass flows at the same input boundary condition velocity are caused by individual geometry of the active parts. For better understanding, the following Figure 60 shows the differences in the cross-section through the active parts and the input area.

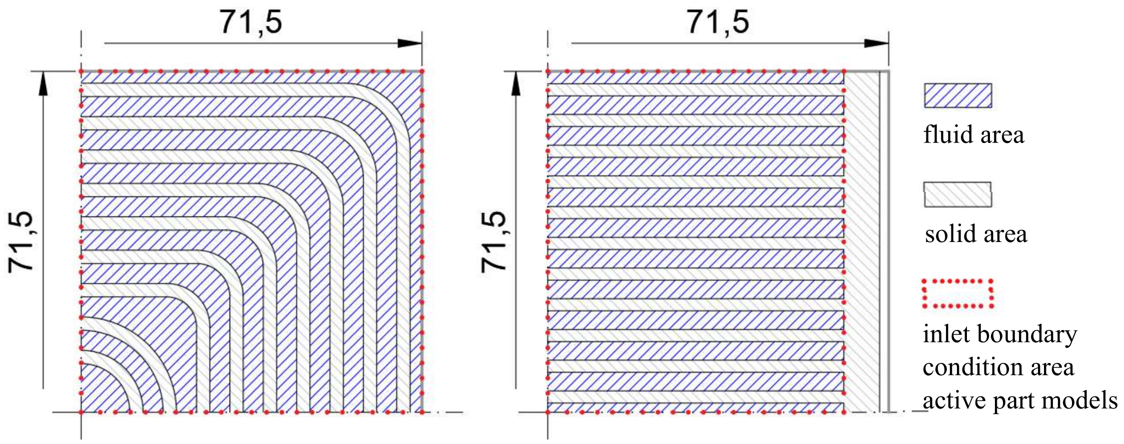

Figure 60 – *The cross-section of both FA used for the active part models*

5.4.2 The comparison between the active part and whole IRT-4M FA

The geometry of the top and bottom nozzle parts is in the case of the IRT-4M FA more complicated than for the CERCA FA. Due to the fuel plates holders, both nozzles have a lower hydraulic diameter than the CERCA FA ones. Based on this fact, a more significant influence on the pressure drop can be expected. The following represented data correspond to the hydraulic characteristic of the active part of the IRT-4M from the previous subchapter and the whole IRT-4M FA. Figure 61 shows the dependence of pressure drop on mass flow.

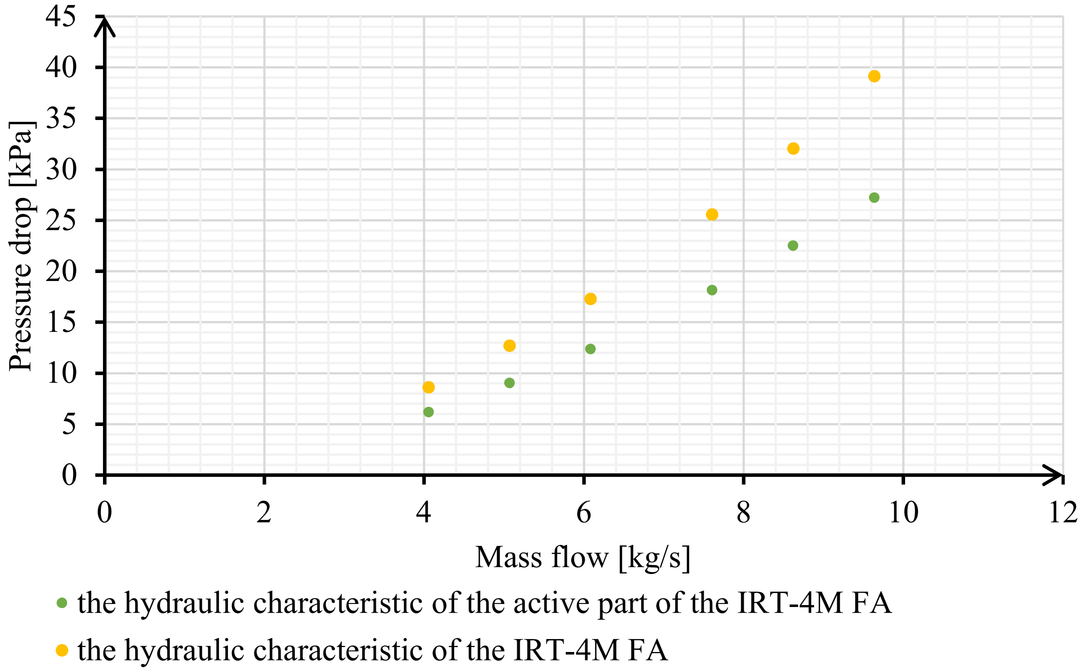

Figure 61 – *The pressure drop dependence on mass flow of the IRT-4M active part and the whole IRT-4M FA*

The impact of the top and bottom nozzle parts on the total pressure drop is around 30 % at higher mass flow values. This increase in the pressure drop due to the top and bottom nozzle parts is significantly higher than for the CERCA FA. This difference is legitimate from the character of the individual nozzle geometries. Specific values of this analysis are documented in the following table 11 in the order of inlet boundary condition.

Table 11 – *The hydraulic characteristic of the active parts the fuel IRT-4M and the whole fuel assembly IRT-4M at the water temperature of 40 °C and operating pressure of 1.32 bar*

BC: Inlet velocity [m·s^{-1}]	**the active part**		**the fuel assembly**	
	Pressure drop [kPa]	Mass flow [kg·s^{-1}]	Pressure drop [kPa]	Mass flow [kg·s^{-1}]
1.9	27.24	9.64	39.13	9.64
1.7	22.52	8.62	32.04	8.62
1.5	18.16	7.61	25.57	7.61
1.2	12.37	6.09	17.28	6.09
1.0	9.04	5.07	12.69	5.07
0.8	6.17	4.06	8.59	4.06

5.4.3 The comparison of the IRT-4M FA and the CERCA FA

For the thermohydraulic of the active zone, the results in this subchapter are crucial. As in the previous subchapter, the dependence of pressure drop on mass flow is represented. From this dependency, it is possible to find out which is the total mass flow through the fuel assembly obtained for a generated pressure drop in the reactor active zone. The resultant mass flow has a further essential impact on the cooling capability of individual fuel assemblies. The higher mass flow means the more significant heat transfer due to the character of turbulent flow and the temperature differences between cooling water and the fuel elements. From this point of view, it is appropriate that the resulting hydraulic characteristic of the CERCA FA reaches the same or lower values of the pressure drop in comparison with the IRT-4M FA. The results of this comparison between the CERCA FA and IRT-4M FA is represented in the following Figure 62. For clarity, the data are also recorded in table 11, in the order according to the inlet boundary condition.

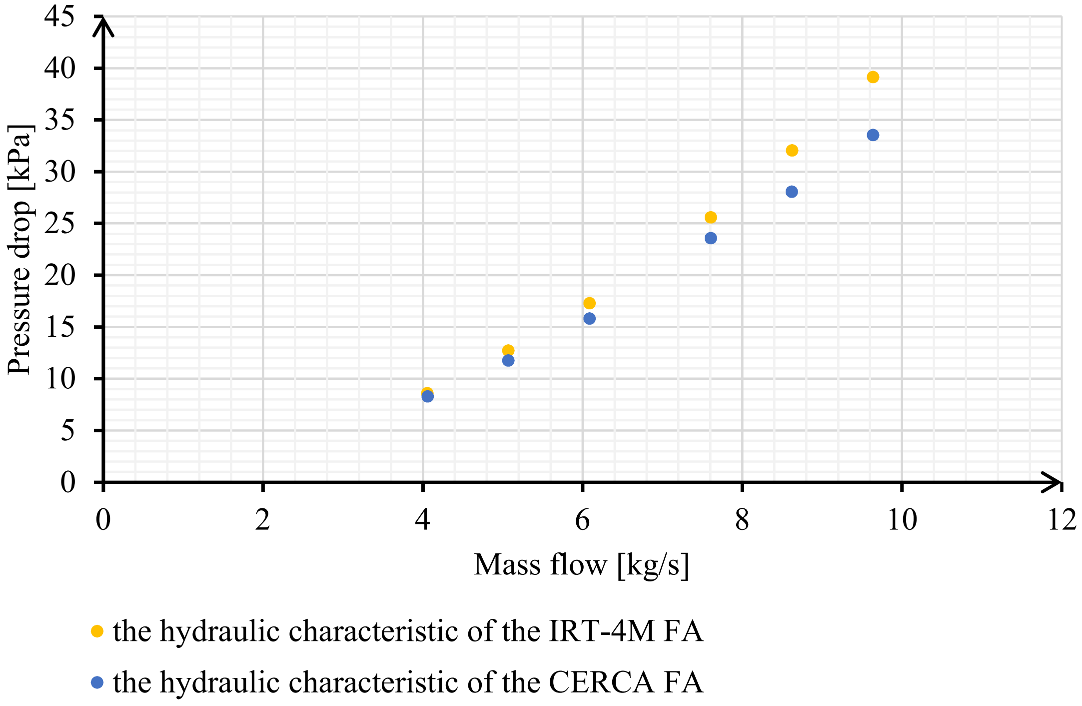

Figure 62 – *The pressure drop dependence on mass flow of the IRT-4M FA and the CERCA FA*

Table 12 – *The hydraulic characteristic of the fuel IRT-4M and the CERCA FA at the water temperature of 40 °C and operating pressure of 1.32 bar*

BC: Inlet velocity $[\mathrm{m \cdot s^{-1}}]$	**the IRT-4M FA**		**the CERCA FA**	
	Pressure drop [kPa]	Mass flow $[\mathrm{kg \cdot s^{-1}}]$	Pressure drop [kPa]	Mass flow $[\mathrm{kg \cdot s^{-1}}]$
1.9	39.13	9.64	33.52	9.64
1.7	32.04	8.62	28.04	8.62
1.5	25.57	7.61	23.55	7.61
1.2	17.28	6.09	15.81	6.09
1.0	12.69	5.07	11.73	5.07
0.8	8.59	4.06	8.28	4.06

From Figure 62, it is possible to see that the CERCA FA has a lower pressure drops for the same values of mass flow compared to the IRT-4M: the difference goes from 0 to 16 %. Due to this result, the CERCA FA seems to be a suitable compensation for IRT-4M in terms of mass flow dependency. However, this does not show anything about its actual cooling capability, because it also depends on the flow character through the fuel assembly. It may happen that most of the coolant flow will go around the fuel assembly instead of the central channels. That case may be potentially dangerous due to overheating of the fuel element plates. The previous chapter *4.4.4 The analysis of the flow inside the CERCA FA* is focuses on this problem.

5.4.4 The analysis of the flow inside the IRT-4M FA

As for the CERCA FA, the analysis of the flow is composed of the velocity contours, the velocity magnitude and the static pressure along the specific line graphs, and particle tracking. The analysis is presented of the whole IRT-4M FA model with the outer flow and the inlet velocity 1.2 $m \cdot s^{-1}$.

The velocity contours on the symmetry surfaces of the model are documented together with the velocity contours of the horizontal cross-section in the following Figure 63, including the color legend for the velocity contours. The graphs of the velocity magnitude and the static pressure are shown as Figures 64 – 75. The graphs are focused on the cross-section of top nozzle area at z-coordinate 0.82 m, the cross-sections of the active part area at z-coordinate 0.37 m with the centre throttle element and at z-coordinate 0.32 m without the central throttle element; the cross-section of bottom nozzle area is situated at z-coordinate 0.04 m. The sections of the following Figures of the particle tracking are marked with blue rectangles. The results of the particle tracking analysis are documented in Figures 76, 77 and 78.

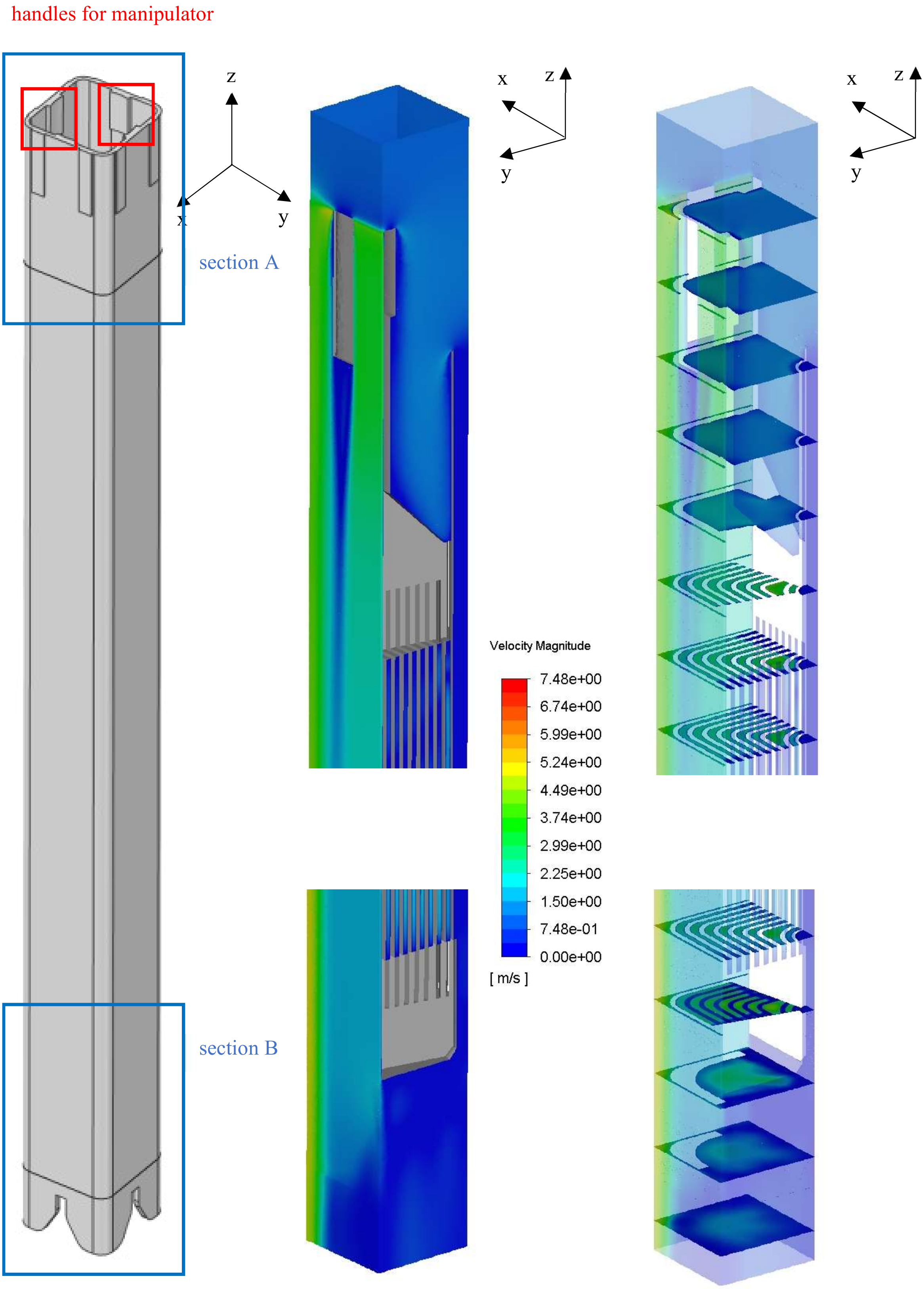

Figure 63 – *The velocity contours of the ¼ IRT-4M FA*

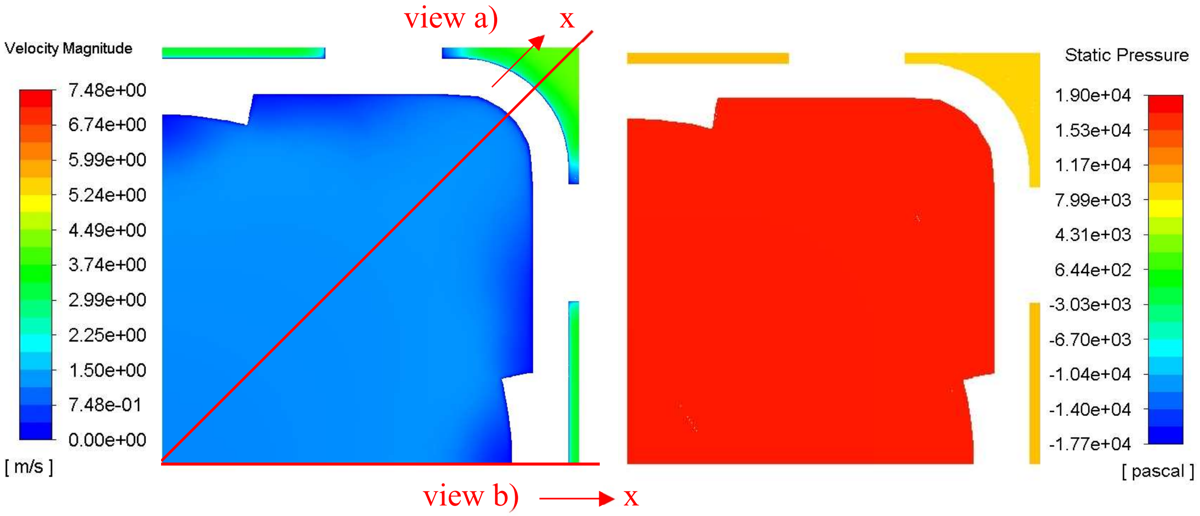

Figure 64 – *The detailed cross-section at z = 0.82 m of the ¼ IRT-4M FA, top nozzle*

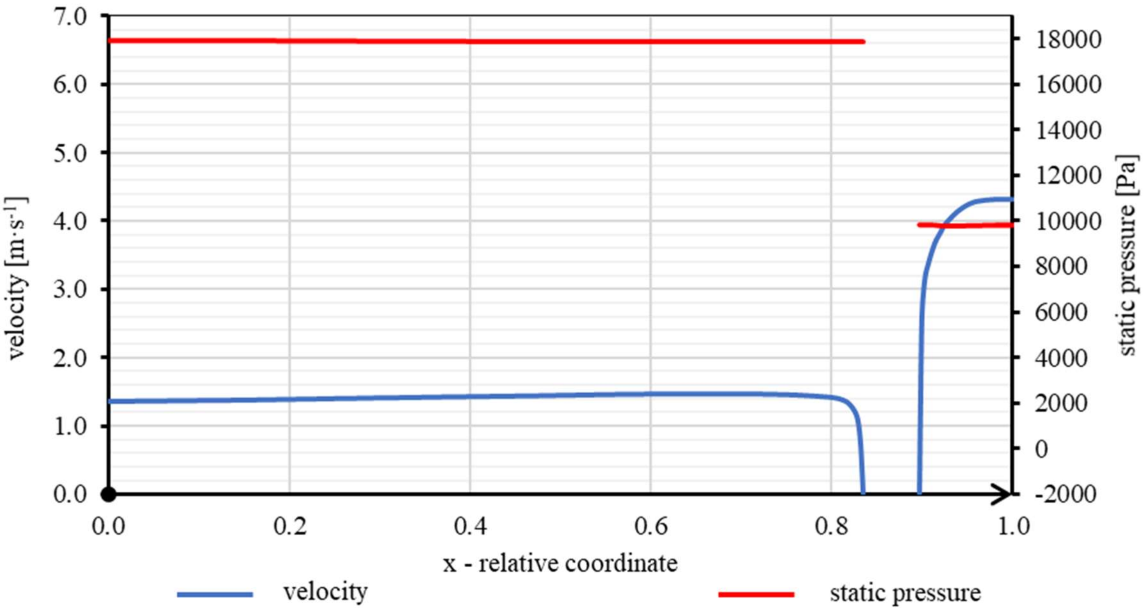

Figure 65 – *The velocity magnitude and the static pressure at z = 0.82 m, view a)*

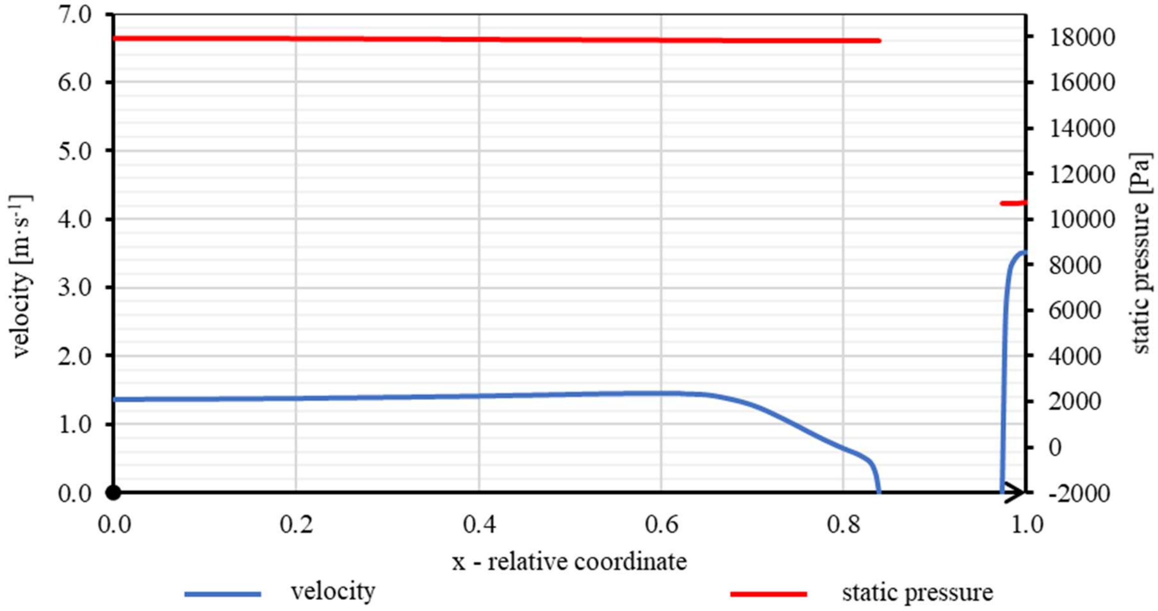

Figure 66 – *The velocity magnitude and the static pressure at z = 0.82 m, view b)*

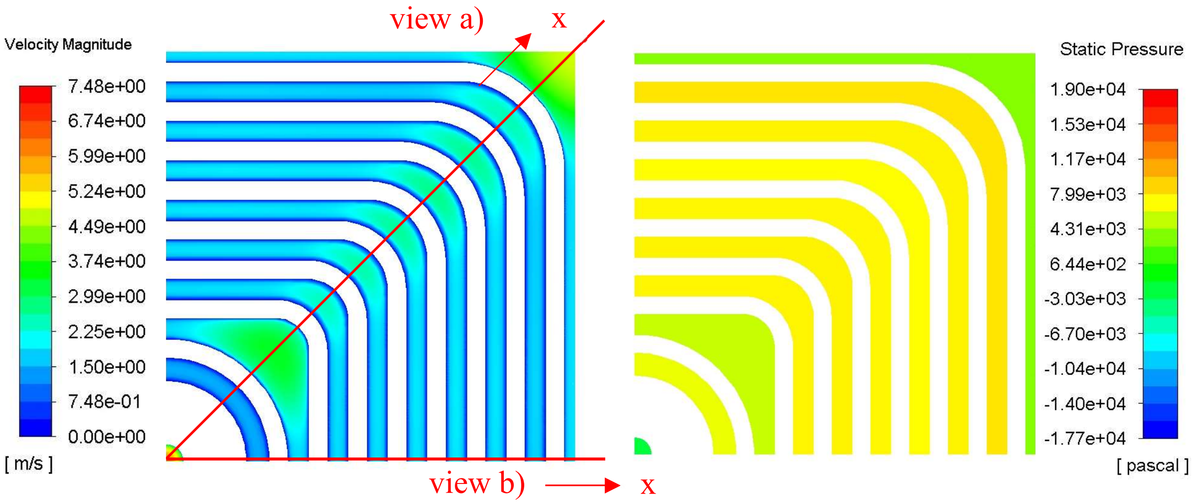

Figure 67 – *The detailed cross-section at z = 0.37 m of the ¼ IRT-4M FA, throttle element*

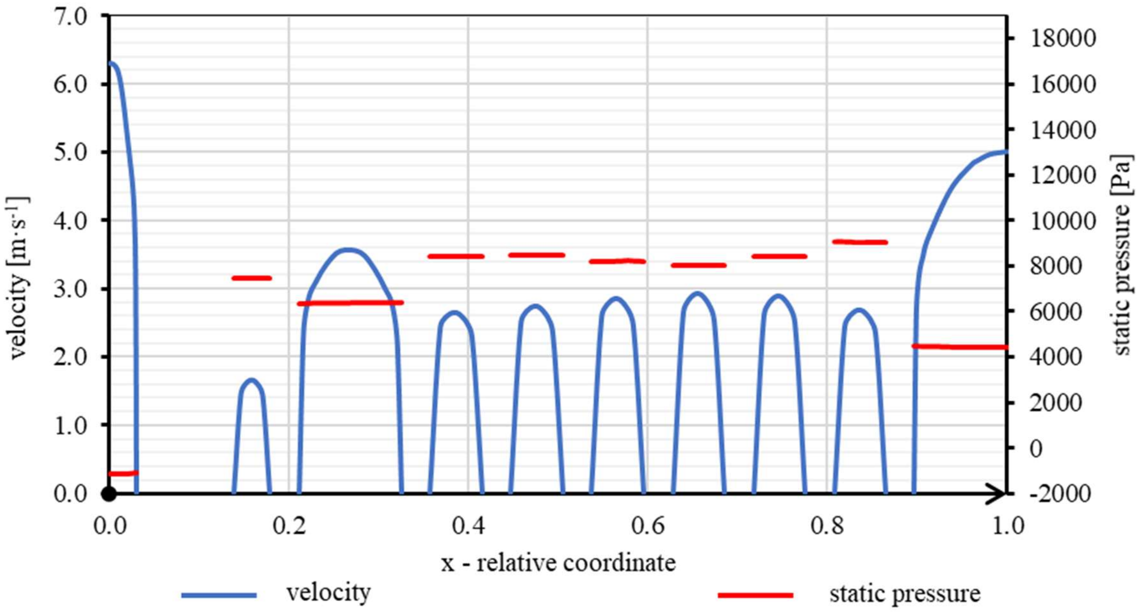

Figure 68 – *The velocity magnitude and the static pressure at z = 0.37 m, view a)*

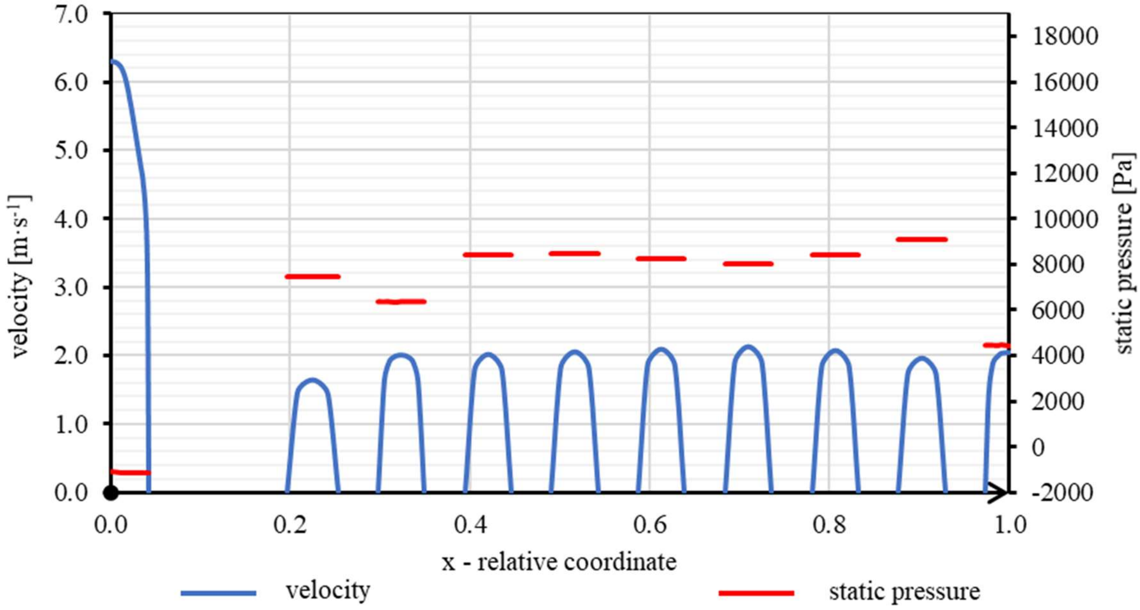

Figure 69 – *The velocity magnitude and the static pressure at z = 0.37 m, view b)*

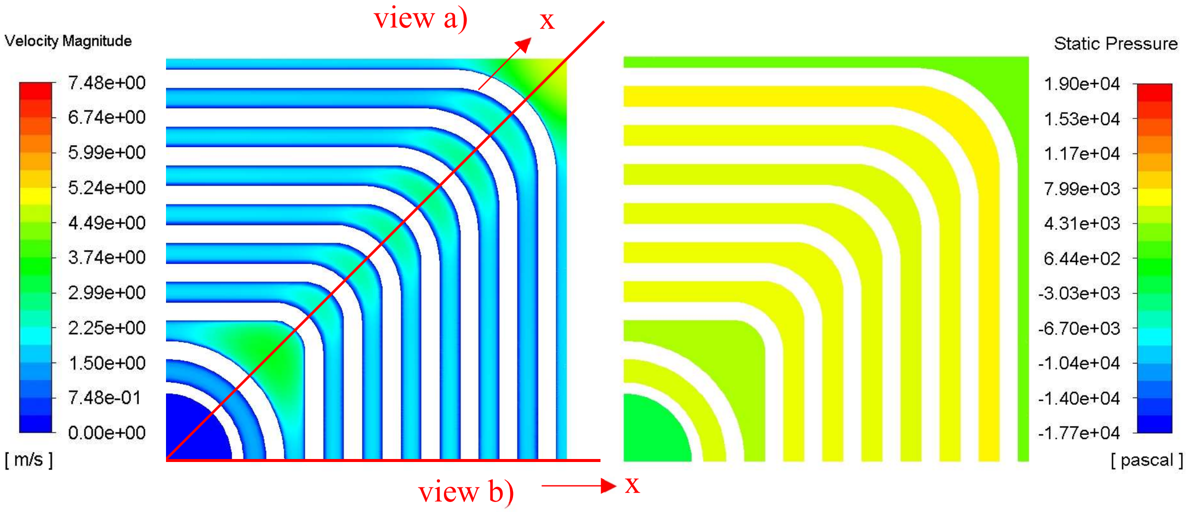

Figure 70 – *The detailed cross-section at z = 0.32 m of the ¼ IRT-4M FA, under throttle element*

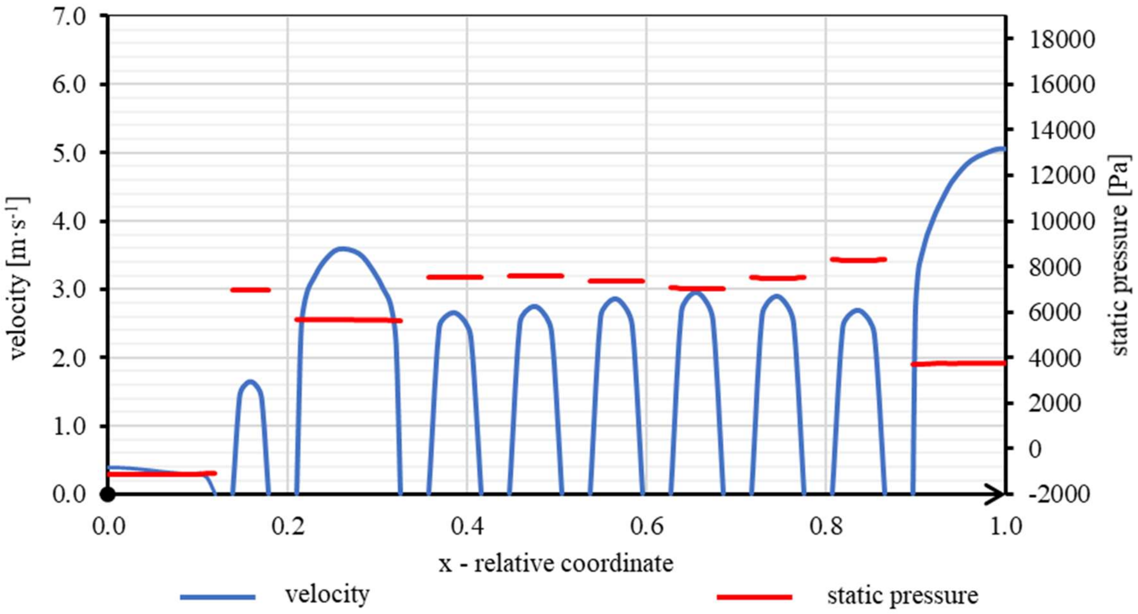

Figure 71 – *The velocity magnitude and the static pressure at z = 0.32 m, view a)*

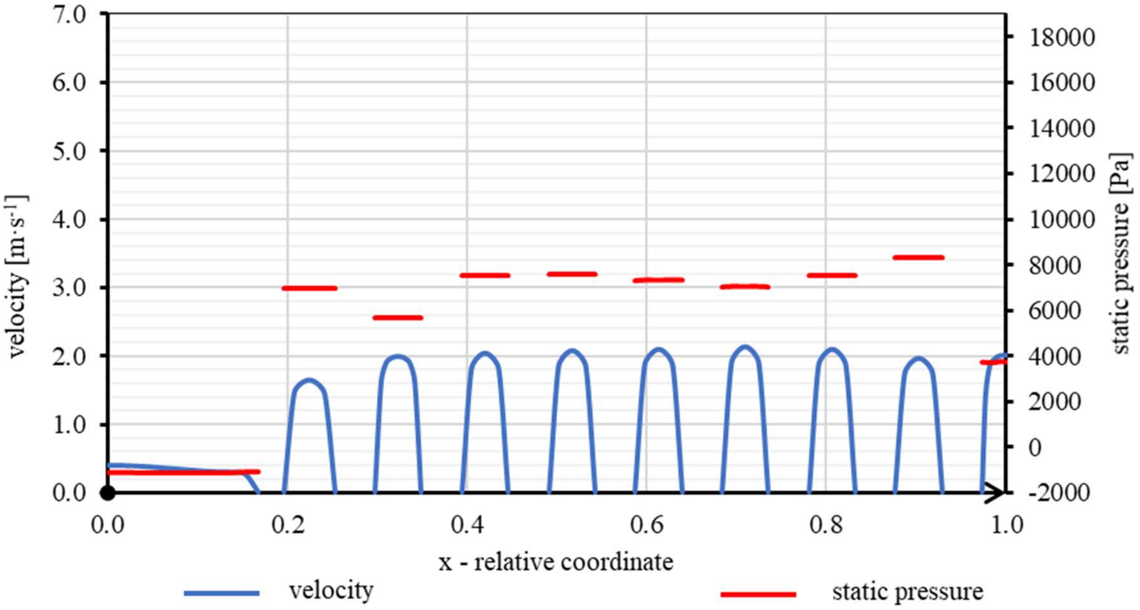

Figure 72 – *The velocity magnitude and the static pressure at z = 0.32 m, view b)*

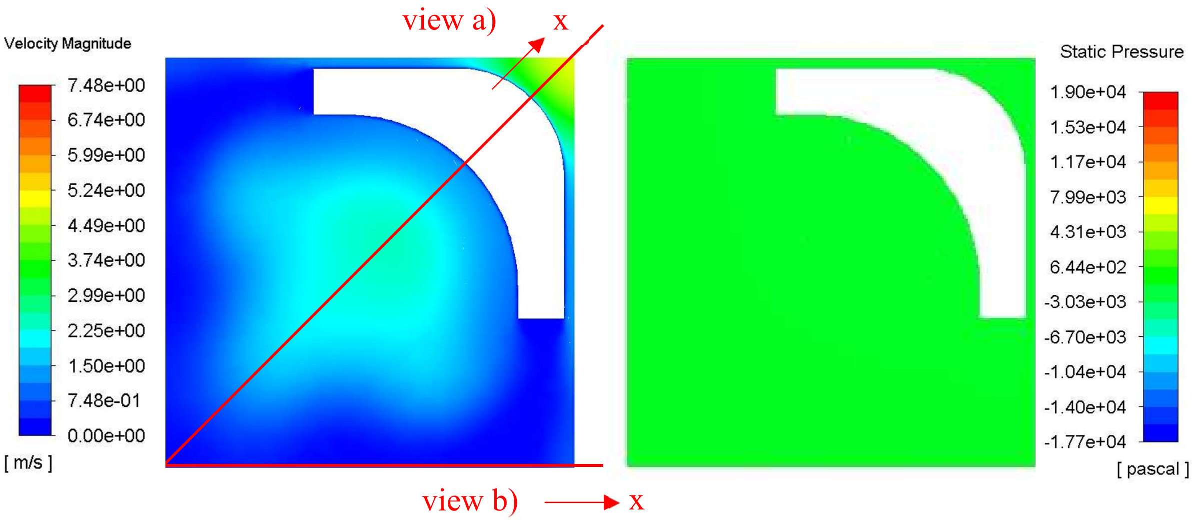

Figure 73 – *The detailed cross-section at z = 0.04 m of the ¼ IRT-4M FA, bottom nozzle*

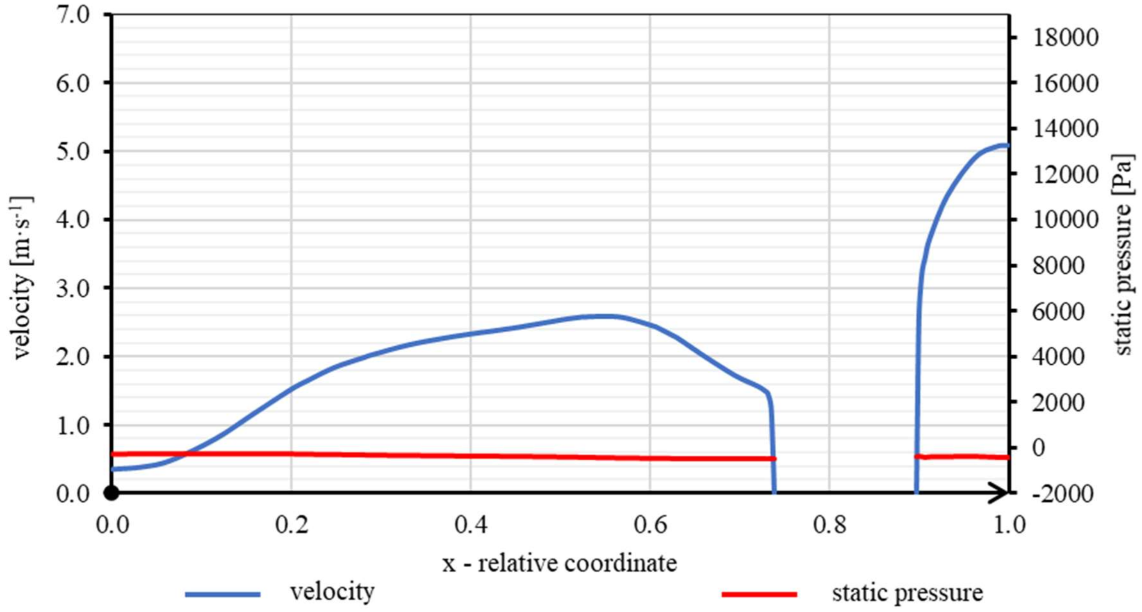

Figure 74 – *The velocity magnitude and the static pressure at z = 0.04 m, view a)*

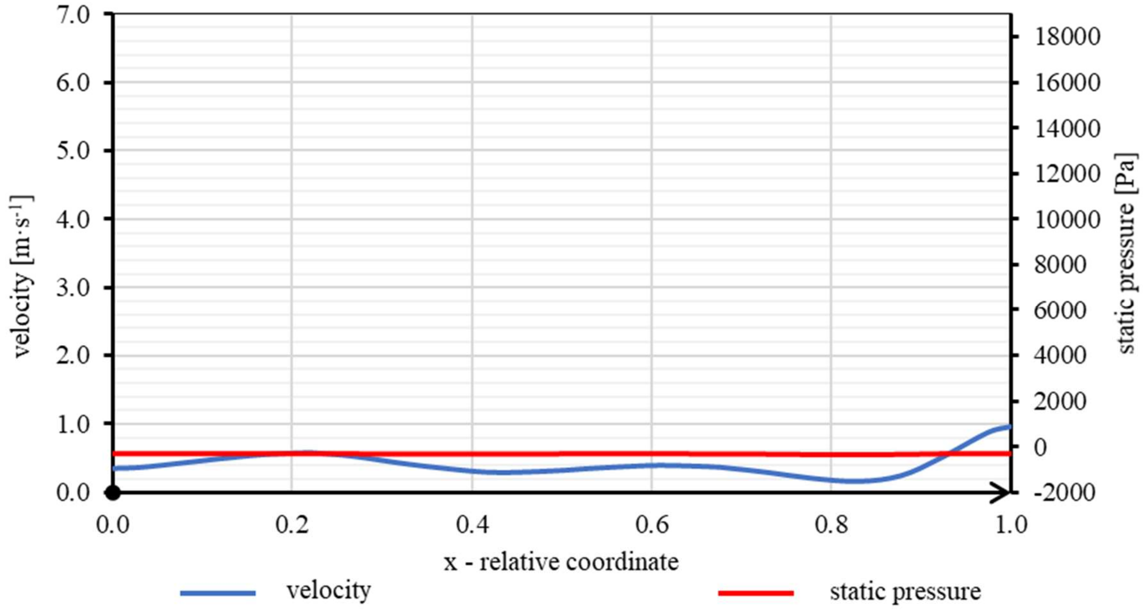

Figure 75 – *The velocity magnitude and the static pressure at z = 0.04 m, view b)*

The IRT-4M FA does not have bypass windows in the area of the top and bottom nozzle parts. However, the high turbulent flow occurs in the area under the fasteners. The fuel elements holder geometry causes the turbulent flow in the inlet and outlet parts. Since a certain channel length is necessary for the flow to fill the whole channel, in the area under these holders high turbulent flow occurs. The maximal velocity 7.48 m·s^{-1} represents in the color legend for the velocity contours occurs in the area of the throttle element which is located in the central tube. This throttle element ensures the lower flow through this central tube, which does not include the fuel; due to this fact, the central tube does not require the same mass flow as other fuel elements.

As in the CERCA FA case, the flow in the top nozzle area is affected by the handles for the manipulator; this phenomenon is documented in Figures 65 and 66. The active part of FA, which is documented in Figures 68 and 67, includes the throttle element; the maximal velocity 7.48 m·s-^{1} is visible there too. Figures 71 and 72 show the cross-section of the active part at lower z-coordinate. The lower velocity in the non-heated central channels, which is caused by this throttle element, is documented. In Figures 74 and 75 it is possible to see the influence of the element holders on the bottom nozzle flow.

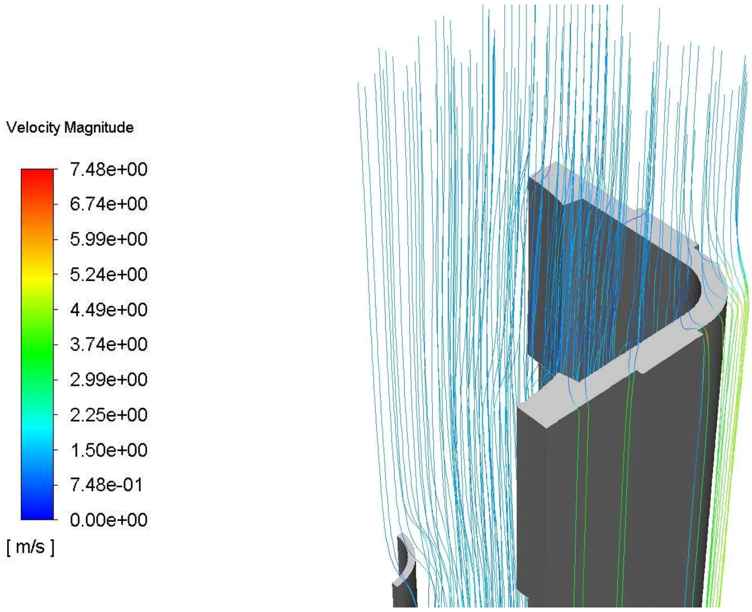

Figure 76 – *The particle tracking in the area of section A – inlet area – IRT-4M FA*

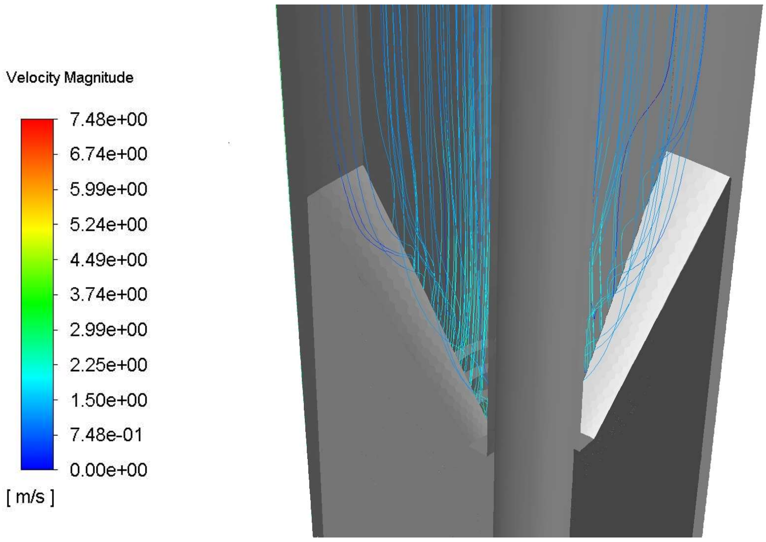

Figure 77 – *The particle tracking in the area of section A – area of the fuel elements holders – IRT-4M FA*

The particle tracking analysis of the top nozzle parts documented in Figure 76 shows the distribution of the flow, which is separated from the inner flow, and is going around the FA. Figure 77 shows the situation in the area of fuel elements holders. The turbulent flow occurs here due to the impact of water flow into the upper wall of the holders.

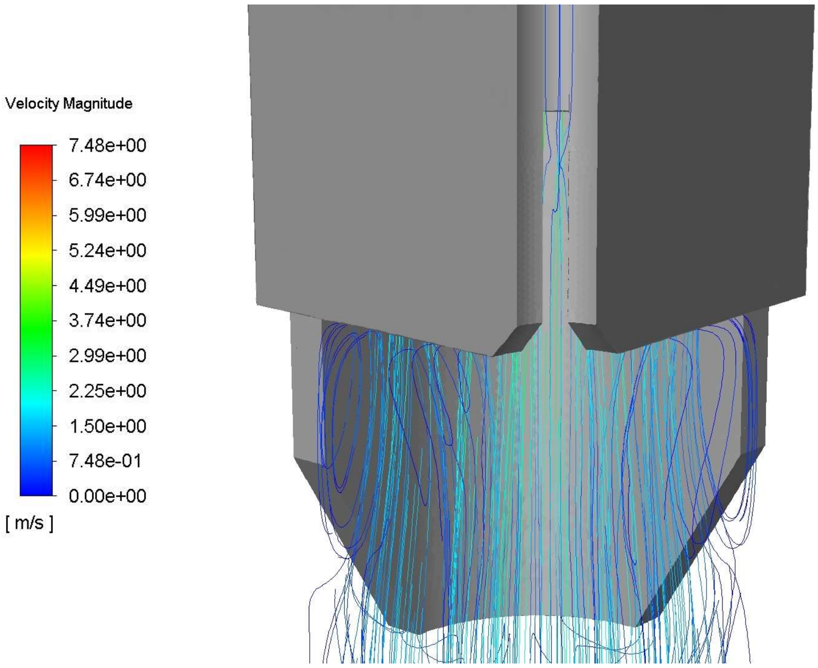

Figure 78 – *The particle tracking in the area of section B – the fuel elements area – IRT-4M FA*

The particle tracking of the bottom nozzle part shows the high turbulences due to the outlet from the channels. The flow in the outlet area of each channel exhibits behavior of the nozzle flow, which may be the source of these high turbulences.

Conclusion

The results of this diploma thesis are structured in a few sections. The first of them is the hydraulic characteristics of both fuel assemblies, specifically the CERCA FA and the IRT-4M FA. This section is described in the previous chapters *4.4.2 the hydraulic characteristics* for the CERCA FA and *5.4.2 The comparison between the active part and whole IRT-4M FA* for the IRT-4M FA. It is possible to see that the CERCA FA has a lower pressure drops for the same values of mass flow compared to the IRT-4M. Due to this, the CERCA FA seems to be a suitable compensation for the currently used IRT-4M fuel assemblies. From this point of view, it would be further appropriate to extend the model with an analysis of the heat transfer generated by the fission reaction and its influence on the hydraulic characteristics.

The other section is focused on the hydraulic axial profiles of the CERCA fuel assemblies. In particular, the axial profile of the pressure drops and of the average velocities in the fuel assembly were assessed. These data are further used in the RELAP system code for the thermohydraulic analysis. As in the previous section, the addition of heat transfer would be appropriate to increase the accuracy of the model.

In the third section, there are the analyses of the flow inside both fuel assemblies. The analyses are composed of the velocities contours on the symmetry surfaces and of the horizontal cross-section for both fuel assemblies. Additional to this, the particle tracking analysis in the specific areas of both analyses is documented. In the case of CERCA FA, it is possible to see a higher velocity in the outer channel in comparison to the inner channels. Figure 47 documents the intended function of the windows in nozzle parts of the CERCA FA. In the window area of the top nozzle, a flow separation from the inner area to the outer nozzle area is occurring. A similar situation occurs in the bottom nozzle area, where a part of the outer flow is separating from the rest, and it passes to the inner bottom nozzle area. For the IRT-4M, the high turbulences in the area under the fuel elements holders in the top nozzle and above fuel elements holders in the bottom nozzle occur. At the outlet of the IRT-4M fuel assembly, the turbulence reaches a higher intensity than in the case of CERCA FA; this phenomenon can be visible by comparison of Figures 47 and 78. However, for a more accurate analysis, it would be appropriate to include the heat transfer as well. Another useful analysis could be the model corresponding to the configuration of the active zone consisting of one CERCA FA and nine IRT-4M FA. This model would feature the symmetric geometry with ¼ of the sample area. In this way, it would be appropriate to analyze the distribution of the coolant flow by individual fuel assemblies in the situation where these two fuel assemblies would occur in the reactor active zone at the same time.

References

[1] ANTES, M., P. NETREBSKY, J. RYCHECKY, J. NEUZIL, V. JURICEK, M. SUNKA and M. MORAVEC. Provozní bezpečnostní zpráva reaktoru LVR-15. Praha, 2018.

[2] VOJACEK, A. Cross section of the LVR -15 reactor with designated core composition for the SCWR-FQT. In: *Research Gate* [online 2019-08-02]. Link: *https://www.researchgate.net/publication/275020464_Design_and_1D_Analysis_of_the_Safety_Systems_for_SCWR_Fuel_Qualification_Test/figures?lo=1*

[3] Example of configuration of active core of LVR-15 reactor. In: Ústav jaderné fyziky AV ČR [online 2019-08-02]. Link: *http://www.ujf.cas.cz/opencms/export/sites/ujf/.content/galerie-content/naa/naa-xfr-active-core-of-lvr-15.jpg*

[4] Experimental hall. In: Ústav jaderné fyziky AV ČR [online 2019-08-02]. Link: *http://www.ujf.cas.cz/opencms/export/sites/ujf/.content/galerie-content/onf/lvr15_hala.png*

[5] Proposal Submission Forms*:* FOREvER. Final. Brussel: European Commission, 2016.

[6] HEGYI, G., A. KERESZTURI and A. TOTA. Qualification of the APOLLO2 lattice physics code of the nurisp platform for VVER hexagonal lattice [online 2019-08-02]. Link: *https://inis.iaea.org/collection/NCLCollectionStore/_Public/42/105/42105718.pdf?r=1&fbclid=IwAR3JOlb_upm0r18fC7sb4HxFSifeSRoe73u5uNhlLACmzQ_rDy8CaNOtkzI*

[7] MARTINOLLI, E., T.C. CARTER, F. CLEMENT, et al. *APOLLO2-A* - AREVA's new generation lattice physics code: Methodology and validation. 2010 [online 2019-08-04]. Link: *https://www.researchgate.net/publication/275969363_APOLLO2-A_-_AREVA's_new_generation_lattice_physics_code_Methodology_and_validation*

[8] NEA-1716 TRIPOLI-4 VERS. 8.1. *NEA:* Nuclear energy agency. 2013 [online 2019-08-02]. Link: *https://www.oecd-nea.org/tools/abstract/detail/nea-1716?fbclid=IwAR0WFyPnU12a0TOkrn2mmaqS_9DnWNwjKzaxuLbE3bMr74O7ieVX__yPIPQ*

[9] MALOUCH, F., E. BRUN, CH. DIOP, et al. Recent developments in the TRIPOLI-4® Monte-Carlo code for shielding and radiation protection applications. EPJ Web of Conferences. 2017, [online 2019-08-02]. ISSN 2100-014X. Link: *http://www.epj-conferences.org/10.1051/epjconf/201715306007*

[10] BESTION, D. System Code Models and Capabilities [online 2019-08-02]. Link: *https://inis.iaea.org/collection/NCLCollectionStore/_Public/42/101/42101978.pdf?fbclid=IwAR1bQBSdi06oeUVjkkuMUG2Agq34VuOTGcuq0yRc3JxgE_vTk2k9zPohT6s*

[11] TRACE V5.0 THEORY MANUAL: Field Equations, Solution Methods, and Physical Models [online 2019-08-06]. Link: *https://www.nrc.gov/docs/ML0710/ML071000097.pdf*

[12] BOYACK, B. E. and L. W. WARD. Validation test matrix for the consolidated TRAC (TRAC-M) code. 2010 [online 2019-08-06]. Link: *https://www.osti.gov/servlets/purl/763345*

[13] Computer codes: The CATHARE2 code. IRSN: Institut de radioprotectin et de surete nucleaire [online 2019-08-02]. Link: *https://www.irsn.fr/EN/Research/Scientific-tools/Computer-codes/Pages/The-CATHARE2-code-4661.aspx?fbclid=IwAR39a4cbh18Dwdpipx6wJ1fb5Flj_XwxFarn3BGJLnxAQP6Y_HX_eJ6epHI*

[14] Gesellschaft für Anlagenund Reaktorsicherheit (GRS) gGmbH. ATHLET 3.2: Program Overview [online 2019-08-15]. Link: *https://www.grs.de/sites/default/files/pdf/athlet_3.2_overview.pdf*

[15] L. VYSKOCIL and J. MACEK, Coupling CFD code with system code and neutron kinetic code, Nuclear Engineering and Design, Vol 279, 210-218, 2014.

[16] KOUBBI, J., M. BOYARD, F. HUET, V. ROMANELLO, A. DAMBROSIO and M. HREHOR. LEU-FOREVER project: Preliminary neutronic calculations status [online 2019-08-02]. Link: *https://www.researchgate.net/publication/332414934_LEU-FOREVER_PROJECT_PRELIMINARY_NEUTRONIC_CALCULATIONS_STATUS*

[17] Serpent [online 2019-08-04]. Link: http://montecarlo.vtt.fi

[18] TUOMINEN, R., V. VALTAVIRTA, J. PELTOLA and J. LEPPANEN. Coupling SERPENT and OpenFOAM for neutronics – CFD multi-physics calculations [online 2019-08-04]. Link: *www.vtt.fi/inf/julkaisut/muut/2016/OA-Coupling-serpent-and.pdf*

[19] SCALE Overview [online 2019-08-15]. Link: *https://www.ornl.gov/scale/overview*

[20] ŠESTÁK, J. and F. RIEGER. Přenos hybnosti, tepla a hmoty. Prague: Czech technical university 1996. ISBN 80-010-0957-2.

[21] BHASKARAN, R. and L. COLLINS. Introduction to CFD Basics [online 2019-08-21]. Link: *https://dragonfly.tam.cornell.edu/teaching/mae5230-cfd-intro-notes.pdf*

[22] ZUO, W. Introduction of Computational Fluid Dynamics [online 2019-08-21]. Link: *http://wwwmayr.informatik.tu-muenchen.de/konferenzen/Jass05/courses/2/Zuo/Zuo_paper.pdf*

[23] PATANKAR, S. V. Numerical heat transfer and fluid flow. Bristol, PA, c1980. Series in computational and physical processes mechanics and thermal sciences. ISBN 08-911-6522-3.

[24] ANSYS Fluent Theory Guide: Release 18.0. 2017.

[25] Fluctuation velocity [online 2019-08-27]. Link: *https://nptel.ac.in/courses/101103004/module5/lec1/images/14.png*

[26] CFD Online: Turbulence modeling [online 2019-08-22]. Link: *https://www.cfd-online.com/Wiki/Turbulence_modeling*

[27] SUGA, K. Recent Developments in Eddy Viscosity Modelling of Turbulence [online 2019-08-24]. Link: *https://www.tytlabs.com/english/review/rev331epdf/e331_039suga.pdf*

[28] KALITZIN, G. Application of the v 2-f model to aerospace configurations [online 2019-08-24]. Link: *https://web.stanford.edu/group/ctr/ResBriefs99/kalitzin.pdf*

[29] Symscape [online 2020-06-09]. Link: *https://www.symscape.com/polyhedral-tetrahedral-hexahedral-mesh-comparison*

[30] ANSYS: Mesh Topologies [online 2020-06-09]. Link: *https://www.afs.enea.it/project/neptunius/docs/fluent/html/ug/node161.htm*

[31] Design Engineering [online 2020-06-09]. Link: *https://www.design-engineering.com/cfd-automeshing-1004028397-1004028397/*

[32] CFD Online [online 2020-06-09]. Link: *https://www.cfd-online.com/Forums/cfx/19480-difference-between-structured-unstructured-mesh.html*

[33] Grid generation. Széchenyi University [online 2020-06-09]. Link: *https://www.feszty.com/uploads/3/6/7/8/3678219/alkalmazottÁramlástan_week9_eng.pdf*

[34] CFD Online [online 2020-06-09]. Link: *https://www.cfd-online.com/Forums/main/219657-how-do-cfd-softwares-calculate-derivatives-unstructured-grids.html*

[35] Applied Computational Fluid Dynamics: Meshing [online 2020-06-09]. Link: *http://www.bakker.org/dartmouth06/engs150/07-mesh.pdf*

[36] All about CFD: Mesh quality [online 2020-06-09]. Link: *https://allaboutcfd-tomersblog.com/2019/02/01/know-thy-mesh-mesh-quality-part-i/*

[37] ANSYS: Students community [online 2020-06-09]. Link: *https://studentcommunity.ansys.com/thread/what-is-the-source-of-mesh-quality-spectrum/*

[38] ANSYS: Mesh quality [online 2020-06-09]. Link: *https://www.afs.enea.it/project/neptunius/docs/fluent/html/ug/node167.htm*

[39] ANSYS: Turbulence Modeling [online 2020-06-09]. Link: *https://slideplayer.com/slide/3872321/*

[40] CFD Online: Enhanced Wall Treatment [online 2020-06-09]. Link: *https://www.cfd-online.com/Forums/fluent/109837-enhanced-wall-treatment.html*

[41] All about CFD: Turbulence Modeling [online 2020-06-09]. Link: *https://allaboutcfd-tomersblog.com/2019/06/21/turbulence-modeling-near-wall-treatment-in-ansys-fluent/*

[42] ANSYS: Converting the Domain to a Polyhedra [online 2020-06-09]. Link: *https://www.afs.enea.it/project/neptunius/docs/fluent/html/ug/node200.htm*

[43] Sborki těplovydělajuščije IRT-4M, Kataložnoje opisanije, P 0019.20.00.000 DKO, Sobstvennosť OAO „NECHK“

[44] Peace Software [online 2020-06-09]. Link: *https://www.peacesoftware.de/einigewerte/wasser_dampf_e.html*

[45] DUPERRAY, R., L. ROUX, and F. HUET, LEU-FOREvER LVR15 fuel assembly preliminary design: thermal-hydraulic studies, 04.03.2019

List of appendices

Since the thesis is connected to the European project focused on the design of the CERCA FA, the DVD with .cas and .dat files of the CERCA FA is attached. These files are corresponding to the model of the CERCA FA active part and the model of the CERCA FA with the outer flow, both with the inlet boundary velocity 1.2 $m \cdot s^{-1}$. The DVD also includes the digital .doc and .pdf version of this diploma thesis text.